UNIVERSITÀ
DEGLI STUDI
FIRENZE

Scuola di
Scienze Matematiche
Fisiche e Naturali
Corso di Laurea Magistrale
in Fisica della Materia

Study and optimization of individual atom manipulation in quantum computational arrays

Studio e ottimizzazione della manipolazione di singolo atomo in registri computazionali quantistici.

Candidato:
Andrea Fantini

Relatore:
Filippo Caruso

Correlatore:
Leonardo Fallani

Anno Accademico: 2021/2022

A nonno Mario,
per sempre al mio fianco

Contents

Chapter 1

Introduction to Quantum Computing

Quantum Computing is now reaching highest levels of expectation, it offers incredible theoretical advantages, but it is still far from being practical.

Quantum simulators are a promising technology on the spectrum of quantum devices from specialized quantum experiments to universal quantum computers. These quantum devices utilize entanglement and many-particle behavior to explore and solve hard scientific, engineering, and computational problems.
Rapid development over the last two decades has produced more than 300 quantum simulators in operation worldwide using a wide variety of experimental platforms. Recent advances in several physical architectures promise a golden age of quantum simulators ranging from highly optimized special purpose simulators to flexible programmable devices. These developments have enabled a convergence of ideas taken from fundamental physics, computer science, and device engineering [**1**].

Quantum simulators are special experimental platforms that are capable of reproducing an Hamiltonian - or a class of Hamiltonians - that describes a particular physical system, in a controllable apparatus. Such devices offer the possibility to simulate in synthetic systems many-body physics problems that can be often very difficult to solve exactly and for which only approximate solutions, if any, exist [**2**]. These platforms can address questions across many domains of physics and scales of nature, from the behavior of solid-state materials and devices, to chemical and biochemical reaction dynamics, to the extreme conditions of particle physics and cosmology that cannot otherwise be readly probed in terrestrial laboratories [**3**].

Recent technical advances have brought us closer to realizing practical quantum simulators. These state-of-the-art experiments involve the control of up to millions of quantum elements and are implemented on a wide variety of atomic, molecular, optical, and solid-state platforms. Each architecture is characterized by strengths and weaknesses for solving particular classes of quantum problems. Simulators handle many problems, from special purpose to highly programmable devices. These systems have the potential to fill a critical gap between conventional supercomputers, which cannot efficiently simulate many-particle quantum systems, and fault-tolerant scalable digital quantum computers, which may be decades away. At the same time, there are significant opportunities for codevelopment of the science and technology underlying both quantum simulators and fault-tolerant quantum computers.

Quantum architecture advantages have been reached in many different branches, like quantum speed up and optimization with short-time Hamiltonian dynamics [**4**] and [**5**]; lately in Quantum Machine Learning we have already got theoretical promising performances that need their own platform to be run [**6**].

The past decade has seen tremendous progress over the control of individual quantum objects. Many experimental platforms, including trapped ions [**7**] and superconducting qubits [**8**], are being actively explored. The current challenge is to extend these results to large assemblies of such objects while keeping the same degree of control, with a view toward applications in quantum information processing [**9**], quantum metrology [**10**], or quantum simulation [**11**]. Neutral atoms offer some advantages over other systems for these tasks. Besides being well isolated from the environment and having tunable interactions, systems of cold atoms keep the promise of being scalable to hundreds of individually controlled qubits. Control of atomic positions at the single-particle level can be achieved with optical potentials. In a "top-down" approach using optical lattices and quantum gas microscopes, hundreds of traps can now be created and addressed individually [**12**]. By making use of the superfluid–Mott insulator transition, single-atom filling fractions exceeding 90% are achieved [**13**], though at the expense of relatively long experimental duty cycles and constraints in the lattice geometries.

Over the past few years, arrays of single laser-cooled atoms trapped in **optical tweezers** have become a prominent platform for quantum science, in particular for quantum simulation. They allow **single-atom imaging** and manipulation, fast repetition rates, and high tunability of the geometry of the arrays. When combined with excitation to **Rydberg states**, these systems naturally implement quantum spin models, with either Ising [**14**] or XY [**15**] interactions. They can also be used to realize quantum gates with fidelities approaching those of the best quantum computing platforms.
A crucial ingredient of the atom array platform is the atom-by-atom assembly of fully loaded arrays, starting from the partially loaded arrays (with a typical filling fraction of 50%–60%) obtained when loading optical tweezers with single atoms [**16**]. This technique, first demonstrated in [**17**], can follow different approaches. A fast and effective approach for realizing one-dimensional chains uses an acousto-optic deflector (**AOD**) driven with multiple radio-frequency tones to generate all the traps [**18**]; after loading, empty traps are then switched off and the remaining ones are brought to their target position, thus achieving a fully loaded chain in a single step. However, directly extending this approach to more than one dimension is challenging [**19**]. A different approach consists of using a spatial light modulator (**SLM**) to generate arbitrary patterns of traps in one, two, or three dimensions, load them with atoms, and then dynamically change the SLM pattern to rearrange the atoms in space [**20**]. However, SLMs are slow, making the rearrangement time prohibitive, which limits this approach to small atom numbers. Another approach is using a static trap array and combining it with a moving tweezer.

Our experiment follows this strategy and uses an SLM that produces a user-defined fixed pattern of optical tweezers which includes the final (target) array, combined with a moving tweezer. This extra microtrap, controlled by a two dimensional (2D) AOD, is used to move the atoms one by one to reach a fully loaded target array. The heuristic "shortest-moves" and its improvements used and developed in

[**21**] in order to find the set of needed moves are versatile, as any target array included in an initial regular array can be assembled. The heuristic "shortest-moves" works well up to a few tens of atoms, but it has some limitations. First, the algorithm was written for regular arrays, such as square and triangular lattices. On completely arbitrary arrays, lattice edges along which atoms can be moved are not naturally given, and using straight paths between source and target traps would lead to unwanted losses, as another target trap already containing an atom may be in the way. A further limitation is that the number of moves needed for ordering is not optimal, and minimizing this number becomes more crucial when the number N of assembled atoms increases beyond a few tens. In figure below we can visualize differences between quantum simulators and quantum platforms.

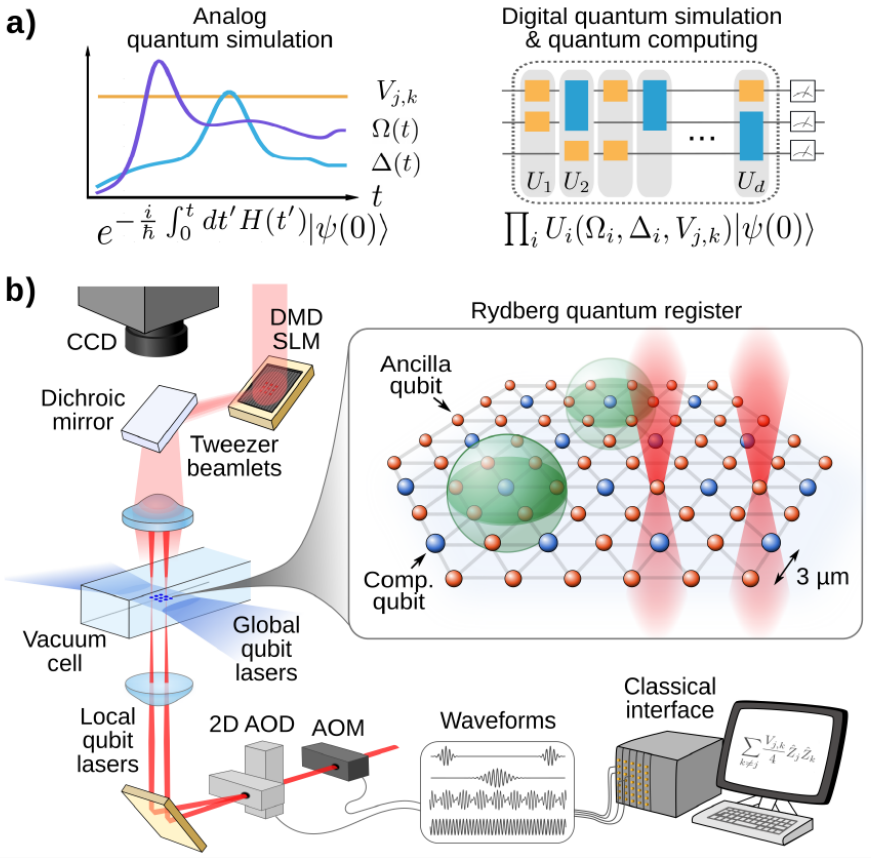

Figure 1.1: Examples of different meaning of quantum computing. In (b) an overlook on the ideal physical quantum computing register and its apparatus with Rydberg atoms. Image taken form [**22**].

Here is a little **legend** to guide everybody in this thesis:

$[a, b]$ is the *commutator of* a *and* b
$v^* =$ *hermitian conjugate of* v
$|a\rangle$ is the a state in *Dirac notation* (*ket* of a), therefore
$\langle a|$ is its *hermitian transpose* (*bra* of a)
$\hat{a}$ is *operator* a, $\mathbf{a}$ (or $\vec{a}$) is *vector* a,
these two notation will get lost as soon as misleading would fade out.

At the end of this thesis I attach a few basic notions, that may help in comprehension and in insight, and the main *MatLab* codes I developed in order to give the reader the oportunity to replicate results and get practice with the problems we are trying to solve. For this study just a bidimensional problem has been treated, but the algorithms in Appendix *D* are totally feasible on three-dimensional arrays too.

1.1 Programmable arrays of ultracold atoms

Atom-by-atom assemblers based on optical tweezers are here used to trap individual neutral atoms of a laser-cooled sample. This particular assebling technique generates a family of platforms where it is possibile to manipulate and move the tweezers and the atoms trapped within them to create ordered, defect-free, arrays of individual atoms with arbitrary geometry. Single neutral atoms trapped in arrays of optical tweezers represent a middle ground between well established quantum simulation platforms like degenerate quantum gases and trapped ions platforms, combining desirable features of these platforms while minimizing some of their weaknesses.

Degenerate quantum gases can employ hundreds of thousands of quantum neutral objects, thus allowing for a high accuracy of the measurements: the standard quantum limit on measurement accuracy, valid for non-entangled systems, scales as $1/\sqrt{N}$, where N is the number of atoms in this case. Moreover, many well known techniques can be carried out to manipulate ensembles of neutral atoms. In ion-based platforms, instead, the strong Coulomb repulsion between charged ions limits the number of particles that can be trapped simulataneously to a few tens. On the other hand, in this platforms the distance between individual ions is large enough to allow for single atom detection, which is instead typically not possible in quantum simulators based on degenerate gases, with the exception of extremely complex quantum gas microscopes. These two platforms also differ for another fundamental feature, that is the typical duty cycle: while degenerate quantum gases need a long process of cooling in order to trap the atoms, resulting in duty cycles of tens of seconds, experiments with trapped ions are typically realized in **less than one second**.

A useful quantum simulator needs to fulfill 3 main technological requests:

1) *Quantum Simulator needs to be scalable to large number of particle in order to play out its advantages.*

2) *Its coherence time needs to be sufficiently larger than the important timescales of the involved physics, in order to obtain the quantum nature of simulation.*

3) *Quantum Simulator needs to be benchmarked, for instance against an analytically known solution or a numerical calculation in a regime where this is possible.*

One possibility to generate interactions among neutral atoms that extend beyond nearest neighbours is to excite them to Rydberg states, which are states where one of electrons of the atom possesses a high principal quantum number.

1.2 First Italian Quantum Machine with Strontium Atoms

Quantum simulators enable probing the static and dynamic properties of correlat-ed quantum many-body systems that would otherwise be numerically inaccessible using classical simulators. First in Italy, a quantum simulator based on programmable arrays of neutral atoms excited to Rydberg states is under development within a scientific collaboration between the Department of Physics of the University of Florence and the National Institute of Optics of the National Reasearch Council. In Fig. 1.2 we show how the experimental setup is going to be like.

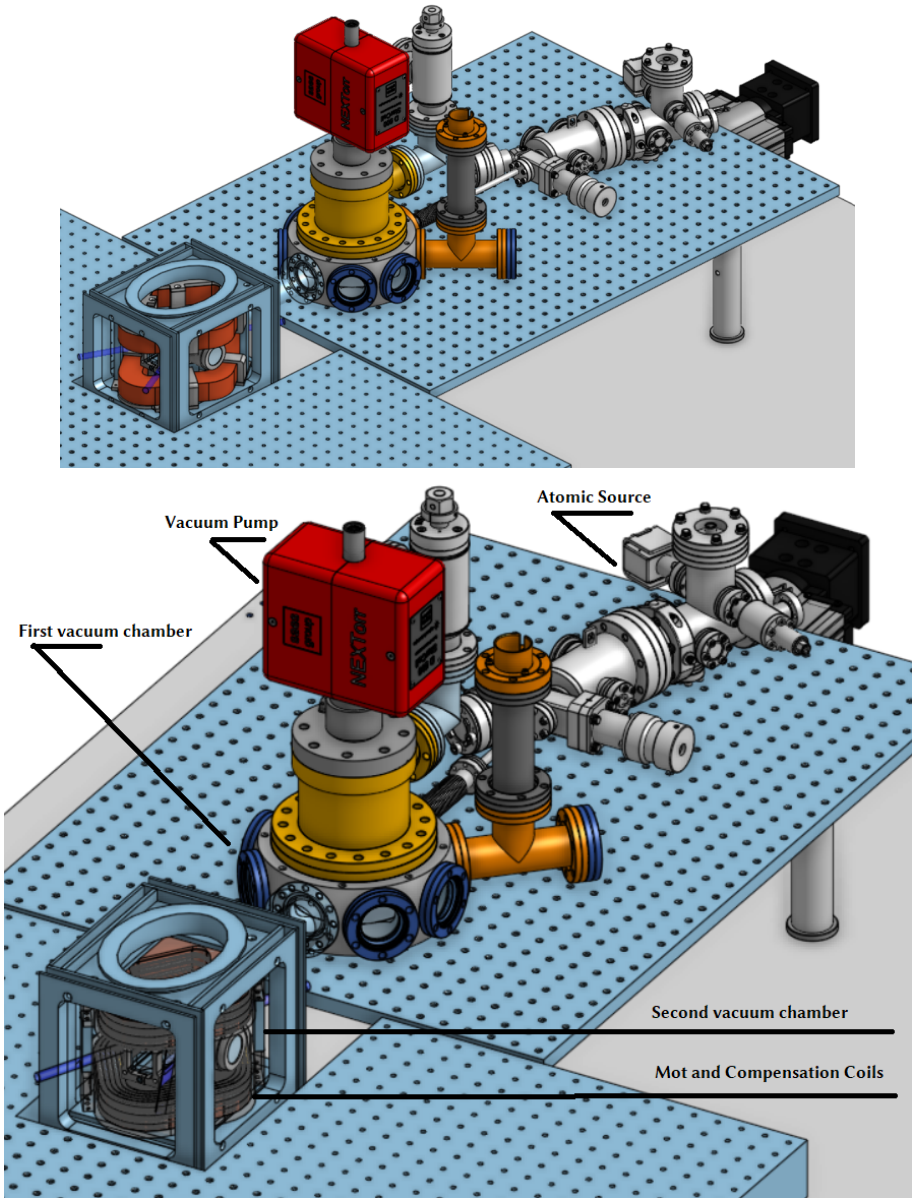

Figure 1.2: Overall Experimental Setup. Two different points of view. Form the right to the left, we can recognise the Sr atomic oven and pump, then the first vaccum chamber, the octogonal one, with its vacuum pump (NEXTorr device), a second vacuum chamer where to perform MOT and surrounded by compensation coils. Image courtesy of the Florence Strontium Tweezers Group.

Such Rydberg atom arrays are advantageous for simulating the dynamics of interacting spin systems (Ising spin models) in higher dimensions and arbitrary geometries. Our simulator uses alkali-earth atoms trapped in two-dimensional arrays of optical tweezers. It will be used for studying many-body quantum dynamics, non-equilibrium physics, and quantum chaos. We will explore these areas after optimizing our control gates and engineering interactions using coherent excitation to Rydberg states. We will also explore novel ideas presented by the early adopter community, such as approaches to gain better insight into advanced materials. Finally, as this project involves the development of novel quantum hardware, including an optimal control toolbox and advanced laser systems, it may lead to further application to quantum enhanced sensing and precision metrology.

The alkaline earth metals are six chemical elements in group 2 of the periodic table. They are beryllium (Be), magnesium (Mg), calcium (Ca), strontium (Sr), barium (Ba), and radium (Ra). Structurally, they have in common an outer s-orbital which is full; that is, this orbital contains its full capacity of the two electrons, which the alkaline-earth metals readily lose to form cations with charge +2, and an oxidation state of +2.

Strontium (Sr) is an alkaline-earth atom of atomic number $Z = 38$ with four stable and naturally occurring isotopes. In this section, we review relevant properties of strontium, its isotopes, its two electrons level structure, and certain key transitions. We will work with Strontium bosonic isotope ^{88}Sr. It has been chosen primarly for its large abundance ($\sim$80%) as well as for the simplicity of its electronic structure. The most relevant property of Sr to us will be the level structure of its outer electronic shell, which importantly has two electrons in an s^2 configuration. This is a property shared by all of the alkaline earth atoms, but is not exclusive to them. Helium, for example, is the quintessential and most basic two electrons atom. Ytterbium is another example, notable for having recently developed experimental techniques [**23**] that are similar to those we show in this work for Sr.

Let me remind here some of **nomenclature** symbols.

Let $\vec{s_i}, \vec{l_i}$ be the spin and orbital angular momentum operators, respectively, for the $i-th$ outer-shell electron. We define $\vec{S} = \sum_i \vec{s_i}$ and $\vec{L} = \sum_i \vec{l_i}$ with associated quantum numbers of $|\vec{S}|^2$ denoted by the same symbol without an arrow S. For two outer-shell electrons, we have $s_1 = s_2 = 1/2$, so the possible values of S are 0 and 1. The $S = 0$ sector contains one S^z state, so we call it a singlet, while the $S = 1$ sector contains three, so we call it a triplet.
We index states of Sr with the following notation:

$$n_1 l_1 n_2 l_2 \qquad {}^{2S+1}L_J \tag{1.1}$$

or, in the case of both electrons occupying the same orbital, by $nl^2\ {}^{2S+1}L_J$, where we use the spectroscopic alphabet (s, p, d, f,...) to index l and the same but with capital letters for L. So, for example, the ground state (which is a singlet) will be referred to as $5s^2\ {}^1S_0$, while a triplet state might be $5s5p\ {}^3P_2$.

This notation suggests that l_i, L, S and J are "good" quantum numbers, meaning that the energy eigenstates labelled by them are either exact or approximate eigenstates of the operators associated with those quantum numbers. This arises when the dominant angular momentum coupling is given by $\vec{L}\cdot\vec{S}$, a situation that is called LS coupling. This is indeed the case for (relevant) states of Sr. Of these quantum numbers, however, only the total angular momentum quantum number J is exact for all states, and this is due to the overall rotational symmetry of the atom. We invite the reader to have a look on Fig. 1.3.

The fact that S is a "good but not exact" quantum number is a key feature of two-electron atoms. Particularly, this becomes important when we look at electric dipole (E1) transitions between states, such as the ones induced by laser light. Strictly speaking, E1 transitions do not couple to electronic spin degrees of freedom, so we have the selection rule $\Delta S = 0$. One might then conclude that E1 transitions between singlet and triplet states are forbidden. However, mixing of atomic eigenstates of equal J but different S (due to strong $\vec{L}\cdot\vec{S}$ spin-orbit terms) makes some nominally triplet states have weak singlet character and vice versa, making transitions between the two sectors weakly allowed. Practically what this means is that two-electron atoms have narrow E1 transitions between singlet and triplet sectors called *inter-combination lines*. These lines are of great experimental utility as they allow for e.g. optical cooling to very low temperatures, precise spectroscopy, and optical clock transitions [**24**].

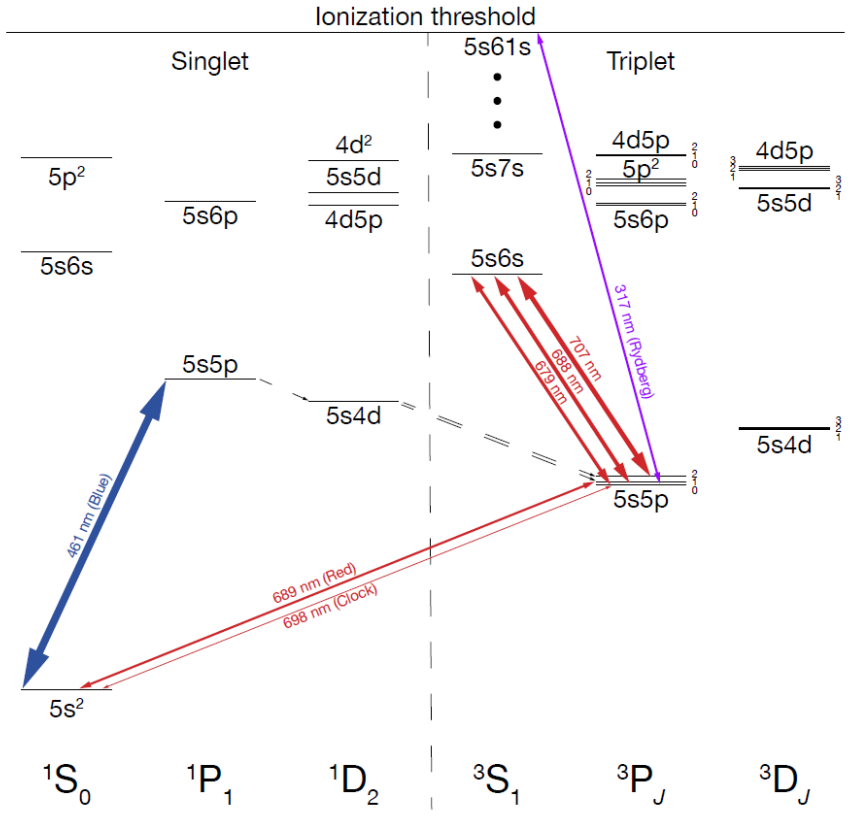

Figure 1.3: Electronic Levels and transitions of interest. We show all states with $L \in [S, P, D]$ up to $5s7s\,^3S_1$ as well as our Rydberg state $5s61s\ ^3S_1$ and the ionization threshold. If a state has fine structure, the J values are listed to the side of the relevant states. Image taken from [**24**].

We are interested in the following **key transitions** of Sr:

BLUE: $5s^2\ {}^1S_0 \leftrightarrow 5s5p\ {}^1P_1$ |460.9 nm| $\gamma = 2\pi \times 30$ MHz ($\tau = 5.3$ ns) This is the primary "strong" singlet ground-to-excited transition of Sr. It is commonly used for slowing, first-stage Magneto-Optical Traps (MOTs), and imaging. In this sense, it is similar to the D_1 and D_2 lines of alkali atoms; however, it is significantly broader by about a factor of 5. This means its Doppler temperature ($T \sim 730$ μK) is higher by the same factor, and furthermore there is no obvious way of achieving sub-Doppler cooling on this transition as the $5s^2\ {}^1S_0$ ground state has no fine or hyperfine structure. This would have made cooling Sr to sufficiently low temperatures im-possible were it not for the red transition. The $5s5p\ {}^1P_1$ excited state has a weak decay channel into the $5s4d\ {}^1D_2$ state, which subsequently decays into the $5s5p\ {}^3P_{1,2}$ states.

RED: $5s^2\ {}^1S_0 \leftrightarrow 5s5p\ {}^3P_1$ |689.4 nm | $\gamma = 2\pi \times 7.5kHz$ ($\tau = 21$ μ s) This is an intercombination line (sometimes called the intercombination line) with a linewidth small enough for a Doppler temperature of $T_d \sim 180$ nK (although, unusually, its recoil temperature is higher at $T_r \sim 230$ nK), but still large enough for cooling to be practical. It does not scatter rapidly enough to make direct cooling of a thermal beam into a MOT very practical, so usually this transition is used for a second-stage red MOT after a blue MOT. Later, we will show that this transition is very useful for cooling and diagnostic spectroscopy in tweezers (Sec. 3.3). To actually take advantage of the narrow linewidth, one must use a narrow laser locked to a high-finesse cavity.

These transitions allow for rapid incoherent population transfer between the $5s5p\ {}^3P$ states. For example, if it is desired to transfer population from ${}^3P_2$ to ${}^3P_1$, one can simultaneously turn on the transitions at 679 nm and 707 nm. Then, ${}^3P_1$ becomes the only dark state in the manifold and, after several scattering events through $5s6s\ {}^3S_1$, it will be populated. This exact scheme is used to return atoms into the singlet blue transition cycle if they have decayed to $5s5p\ {}^3P_2$ through the weak $5s4d\ {}^1D_2$ channel after a decay from the ${}^3P_1$ to the ${}^1S_0$.

Repumps

$5s5p\ {}^3P_0 \leftrightarrow 5s6s^3S_1$ |679.3 nm | $\gamma = 2\pi \times 13$ MHz ($\tau = 120$ ns)

$5s5p\ {}^3P_1 \leftrightarrow 5s6s\ {}^3S_1$ |688.0 nm | $\gamma = 2\pi \times 39$ MHz ($\tau = 41$ ns)

$5s5p\ {}^3P_2 \leftrightarrow 5s6s\ {}^3S_1$ |707.2 nm | $\gamma = 2\pi \times 67$ MHz ($\tau = 24$ ns)[**24**]

In this work we have optimized the process of atoms array configuration in order to create costumized patterns of quantum computing registers. The study was divided in two big optimization problems. **The first one**: how to optimize the process of atoms *imaging* in terms of readiness and in the less disturbing way. **The second one**: how to create the best atom reordering algorithm in terms of computational running time and experimental costs. The central idea around this work is to simulate a physical system under well controlled conditions.

1.3 Entanglement via Rydberg excitation

A Rydberg atom is an atom in which one electron is excited to a high principal quantum number (n) energetic level. One possible scheme for obtaining a Rydberg atom relies on the excitation of the electron via a laser coupling. If the atom considered is a neutral atom, it has no net charge and does not interact via Coulomb interaction. Nevertheless, in the Rydberg excitation the atom acquires a very large induced electric dipole moment. Many important properties of a Rydberg atom differ from those of a ground state atom, because they depend on the principal quantum number n.

Property	scaling	Value for $^{80}Sr_{1/2}$ Rb
Binding Energy E_n	n^{-2}	-500 GHz
Level Spacing $E_{n+1} - E_n$	n^{-3}	13 GHz
Size of wavefunction $< r >$	n^{+2}	500 nm
Lifetime τ	n^{+3}	200 μs
Van der Waals C_6	n^{+11}	4 THz·μm^6

(1.2)

In this table we see an example that the size of the wavefunction scales up as the square of n and can reach dimensions of a few μm. Fig. 1.4 shows the simulation of the spatial wavefunction of a Rubidium Rydberg atom in the $80S_{1/2}$ state, which has an extension of the order of 1 μm. This aspect is fundamental for generating interaction between the atoms in the array of optical tweezers. Neutral ground state atoms do not interact via Coulomb interaction, since they have no net charge, but they can interact via Van der Waals or dipole-dipole couplings. Anyway, the spatial extension of a ground state wavefunction, on the lengthscale of the Bohr radius a_0, is so small that a couple of ground state atoms interact via contact interaction only.

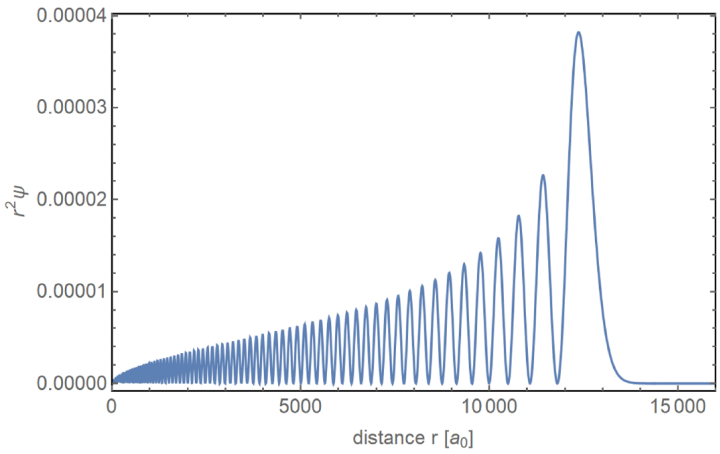

Figure 1.4: Simulated wavefunction for the $^{80}S_{1/2}$ level. Image taken from [**2**].

Since in optical tweezers each site is loaded with one atom, ground state atoms are not interacting at all in the array. In the Rydberg regime the spread of the wavefunction is instead 10^4 times higher and there is a non-zero overlap between neighbouring atoms in the array, that are typically separated by $5 - 10$ μm. The atoms interact via strong induced dipole-dipole interaction. The interaction between

a couple of atoms both excited to the same Rydberg level can be huge, as a consequence of the scaling of the Van der Waals coefficient with the eleventh power of n, as pointed out in Table (1.2). Actually, the Van der Waals interaction is not the only regime in which atoms can interconnect, since they can also show dipolar interaction. These two interaction regimes differ on whether both the atoms are excited to the same Rydberg level or not. As shown in the next lines, dipolar and Van der Waals interaction regimes have different scaling on the principal quantum number n and on the spatial separation R. Anyway, both the interaction regimes produce strongly interacting couples or ensembles of atoms.

In order to generate an entangled state between qubits, some kind of interactions between the qubits are necessary. Effectively zero-range interactions have been used to entangle atoms that are allowed to occupy the same trap and to simulate manybody Hubbard models. However, ground state atoms are typically non-interacting at long ($\gg 50$ nm) range. Since our atoms will be in optical tweezers spaced at several μm apart, we must induce long-range interactions. One approach is to place the atoms in a cavity, which allows for photon-mediated interactions. Our approach to long-range interactions will instead be precisely to drive atoms to Rydberg states. **Rydberg interactions** were proposed as a potential entangling resource for neutral atoms in the early 2000s as [**25**]. **Rydberg blockade**, a mechanism for generating entanglement between atoms, was observed in 2009 in [**26**], and was soon after used to generate entanglement in hyperfine ground states. Rydberg interactions were later used in optical lattices and for entangling operations and quantum simulation in large arrays.

Rydberg interactions have been most recently combined with the technique of array rearrangement, allowing for the study of re-configurable, defect-free many-body entangled atomic arrays. And this is the way we are following.

Chapter 2

Cooling and Trapping setup

The cooling phase can be performed through two steps of Magneto Optical Trap (MOT): the first one exploits the principal blue excitation line for Sr atoms, the ${}^1S_0 \rightarrow {}^1P_1$ transition at 461 nm, then the second step has the ${}^1S_0 \rightarrow {}^1P_1$ red intercombination line (at 689 nm). The linewidth of the intercombination line is 2π 7.6 kHz and it is small enough to cool the atoms down to a few hundreds of nK [**27**], a temperature much lower than that achievable for alkali atoms with the Doppler cooling only. The efficient Doppler cooling performed thanks to the red line is sufficient to trap the atoms in the optical tweezers, whose trap depth is on the order of 1 mK. Hence, an evaporative cooling procedure is not necessary for this application. That is important because it drops significantly down the preparation time during a typical duty cycle. Although the temperature reached by the MOT is low enough to trap the atoms in the tweezers, there is still a substantial probability of finding the atoms in excited vibrational states in the trap. It is then possible to implement cooling schemes directly in the tweezer that allow us to cool atoms down to the ground state of the trap.

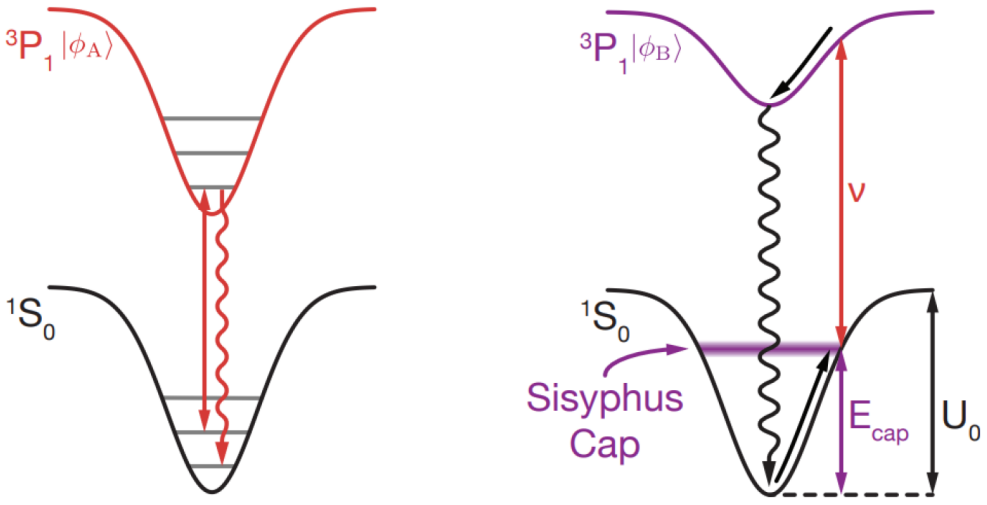

Figure 2.1: The two cooling techniques. Left: Sideband cooling scheme for a two-electron atom trapped in an optical tweezer. Right: Sisyphus cooling scheme for a two-electron atom trapped in an optical tweezer. Images taken from [**28**].

In the case of Sr atoms, **two** possible approaches can be exploited, depending on the wavelength of the tweezer traps, as shown in Fig. 2.1. The **first** cooling technique is a sideband cooling, that exploits red sideband trasitions to decrease the vibrational state of the atom in the trap. In the case of alkali atoms the natural linewidth of the atomic transitions is larger than the vibrational levels spacing, hence the technique used for cooling the atom in the trap is the Raman sideband cooling, that makes use of a two-photon transition whose energy separation covers the energy gap between vibrational states. The sideband cooling used for two-electron atoms, such as Strontium, is instead a direct scheme, based on a single-photon transition and spontaneous decay. Let us consider the atom as a two-level system, $|g\rangle$ and $|e\rangle$, trapped in an optical tweezer at magic wavelength, such that the two levels feel the same trapping potential due to identical light shifts. A schematic representation of the sideband cooling is shown in Fig. (2.1a): the frequency of the red transition is tuned in such a way to excite the atom from $|g\rangle$ state to the $|e\rangle$ state, but in a lower vibrational level. It was verified, e.g. in 26, that under certain experimental conditions the spontaneous emission decay maintains the the vibrational state of the atom, hence the net result is a decrease in vibrational level. Such a cooling scheme is not possible for alkalis, because the bandwidth of the excitation laser is much larger than the separation between vibrational levels and a proper target level cannot be chosen. The sideband cooling scheme can be implemented for Sr atoms exploiting the intercombination ${}^1S_0 \rightarrow {}^3P_1$ that has a natural linewidth of 2π 27.6 kHz, smaller than the typical separation between vibrational levels that is of the order of tens of kHz. This technique is going to be treated widely later in Subsect. (3.3.2).

A **second** cooling technique, called Sisyphus cooling, can be exploited to keep the atoms below a desired value of motional energy within the trap [**28**]. In this case a non magic wavelength trap is considered: for example the excited state $|e\rangle$ is less trapped than the ground $|g\rangle$. This mechanism is important especially during the imaging stage, where atoms continuously scatter the broad band blue light. The energy kicks of the imaging light heat up the atoms in the $|g\rangle$ state, increasing their vibrational state. Since the trapping potential is non magic, the photon of the Sysiphus cooling laser beam is resonant only for a restricted fraction of atoms that have the correct energy. Consider for example Fig.(2.12b), where a photon with frequency is resonant with the $|g\rangle \rightarrow |e\rangle$ transition at the side of the trap. If an atom acquires enough energy to reach the value for which the cooling photon is resonant, it will be excited to the $|e\rangle$ state. After spending some time in the excited trap, the atom decays preferably in the ground vibrational level of the electronic state $|g\rangle$. This mechanism keeps the atoms below the energy value for which the cooling photon is resonant. The cooling works because of the mismatch of the energy of the photons exchanged. In particular, the cooling photon is less energetic than the spontaneously emitted one. Hence, we will perform both cooling techniques in order to keep atoms cold the most and in the most continuous way.

2.1 AOD and SLM

In this section we are going to present the use of two kinds of devices for the creation of arrays of optical tweezers, namely *Spatial Light Modulators* (SLMs) and *Acousto Optic Deflectors* (AODs). As mentioned above, an *Optical Tweezer* (OT) is an optical dipole trap that is tightly focused, on a lengthscale of around 1 μm, by a high numerical aperture (NA) objective. Thanks to light-assisted collisions that rapidly expel pairs of atoms, it's possible to trap at most one single atom in each optical tweezer, thus making the tweezer a perfect tool to control and address single atoms. Pair losses are the consequence of the interaction of a pair of atoms trapped in the optical dipole potential with a properly detuned laser beam. This collisional blockade mechanism results in either zero or one atom loaded in an optical tweezer, with probability $p \sim 0.5$. The light-matter interaction describing the trapping technique is presented in this Chapter, in Section 2.2 [**30**].

The idea of trapping individual atoms can be extended to several optical tweezers, that can be assembled together to form an array of OTs. The assembly of several optical tweezers can be accomplished making use of mainly two devices to arrange the tweezers to form complex patterns, the above mentioned AODs and SLMs. Although these devices exploit completely different technologies, they can both produce multiple beams, that will then be focused to create multiple OTs, starting from one single laser beam. Arrays of hundreds of tweezers - and so hundreds of atoms - were recently realized by means of these two techniques [**28**, **29**], as shown in Fig. 2.2.

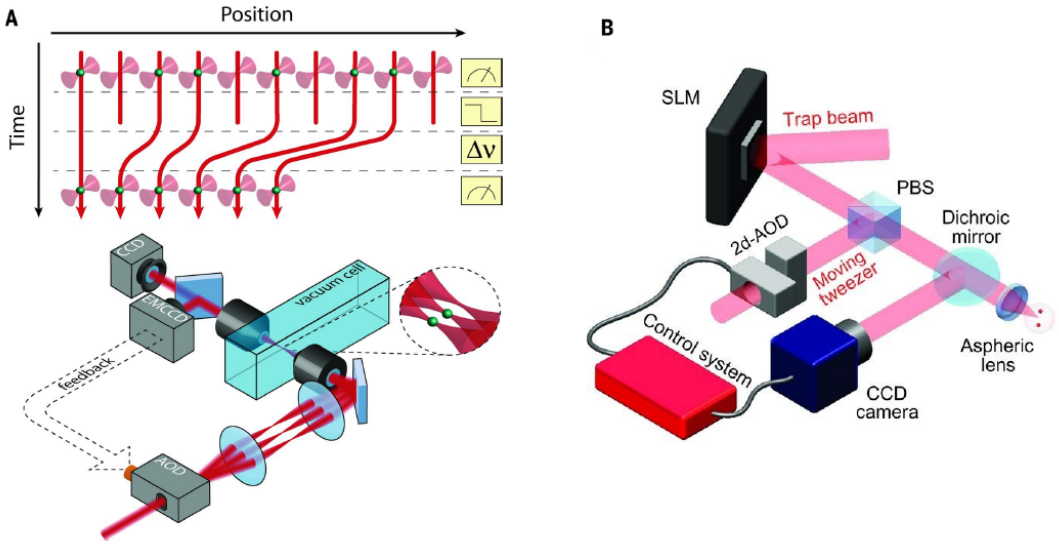

Figure 2.2: Realization of OT arrays by means of AODs and SLMs. Left: 1D array created using only one AOD. Image taken from [**28**]. Right: 2D array created with a SLM. Image taken from [**17**].

Acousto Optic Deflectors are devices that use the acousto-optic effect to deflect a laser beam. Like Acousto Optic Modulators (AOMs), AODs are composed of a piezoelectric transducer, that is guided by a RF signal, and a crystal that vibrates under the effect of the transducer. The difference between AODs and AOMs is that

the first are more suitable for the deflection of multiple beams at different angles. An AOD working with multiple frequency components produces a 1D array of deflected beams that, once projected by a high numerical aperture objective, form an array of optical traps in which atoms are trapped individually (Fig. 2.3).

Figure 2.3: Rearrangement of arrays of optical tweezers in arbitrary patterns. Defect free 1D array rearranged usind one AOD. Image taken from [**28**].

Two dimensional arrays can be achieved by considering a pair of AODs perpendicularly oriented, as shown in Fig 2.4. This simple scheme for the realization of a 2D array involve anyway some limitations, because it can only provide square or rectangular arrays. In fact, the presence of a perpendicular AOD can only copy the linear 1D pattern in multiple lines/columns but is constrained by the pattern of the first 1D array. Nevertheless, more complex experimental schemes can be implemented to produce arbitrary geometry patterns both in a static and in a dynamic way.

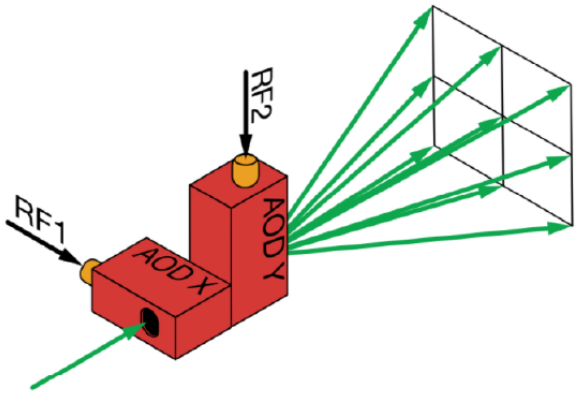

Figure 2.4: Creation of a 2D pattern using crossed AODs. Image taken from [**26**].

The static scheme makes use of SLMs, while the dynamic creation of arrays showing arbitrary geometry relies on a time-averaged potential technique that can be carried out by means of the AODs alone. SLMs are based on liquid crystals, a completely different technology with respect to AODs. These devices work with holographic techniques and imprint a phase pattern on the input beam that hits the SLM's screen in order to obtain a certain spatial pattern in the conjugate plane. Liquid crystals are oriented with electric fields and behave as a diffraction grating for the light beam. According to the phase pattern imprinted on the screen of the device, the beam is deflected and the desired spatial pattern is reproduced onto the Fourier plane conjugated with the plane of the screen. SLMs allow for the realization

of any kind of static pattern geometry (Fig. 2.5). Moreover, these devices produce, in general, a higher number of spots, and so OTs, with respect to the AODs scheme. A second way of producing an array of optical tweezers arranged in a pattern of arbitrary geometry relies on a time-averaged potential technique. This technique is currently used in many fields and applications but its implementation for the creation of array of optical tweezers is still under investigation.

The basic idea of this technique consists of using one single deflected beam at once and making it jump periodically over all the positions that we want to include in our array. During one cycle the beam spends a fraction of the period over each position. If one atom is initially trapped in one of these sites, it will feel a trapping potential as long as the deflected beam stays onto that site, while it falls down under the effect of gravity during the rest of the period. To trap the atoms with high fidelity, each atom has to be recaptured before it falls out of the action range of the optical tweezer trap, so the rate - the potential is switched at - must be very high. Ref.[**2**] has characterized the optimal frequency for the switching.

The methods described above satisfy only one of the two conditions that a good array of optical tweezers should have: the possibility of creating an arbitrary pattern both in one and two dimensions. Because of the light assisted collisions mentioned above, that produce the loss of pairs of atoms when they occupy the same site, an optical tweezer can be loaded with either 0 or 1 atom. Typically, the probability of loading one atom per tweezer is $p = 0.5$ and in Chapter 4 we will see the reason why. This p value means that in every experimental cycle the stochastical loading of the atoms in the array will populate approximately the 50% of the sites. Hence, generating an arbitrary geometry array is not sufficient, and a feedback system that allows the rearrangement of the atoms is necessary to prepare the ensemble of atoms in the array in the desired configuration: such a system needs to know where the atoms are loaded and where to move them.

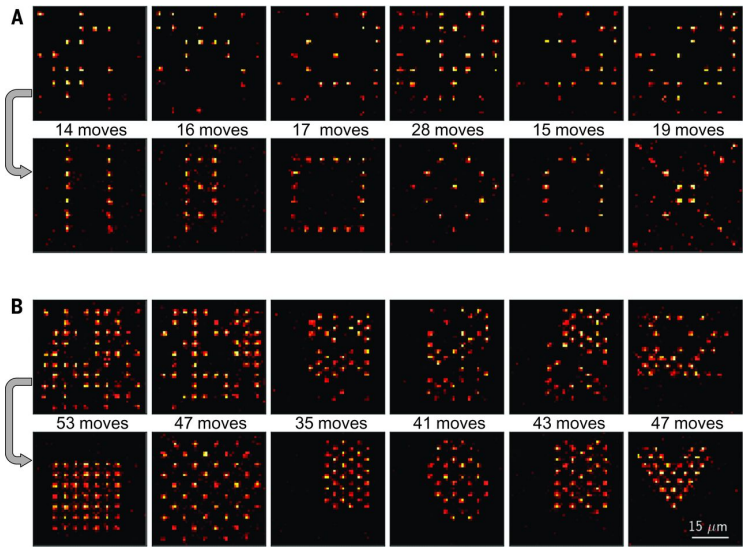

Figure 2.5: Rearrangement of arrays of optical tweezers in arbitrary patterns. Gallery of fully loaded arrays. Arbitrary, user-defined 2D arrays (bottom images) are obtained from the initial, random configurations (top images). All images are single shots. The number of elementary moves needed to achieve the sorting are indicated. Image taken from [**17**].

2.2 Optical Tweezers

In order to consider the global effect of light on atoms in the trapping phase, we can now include external motion energy of the atom. The total Hamiltonian Operator of the open quantum system composed by the laser field (F), by the atomic system (A) and by the environment (E), is the following:

$$\hat{H} = \frac{\hat{\mathbf{P}}^2}{2M} + \hat{H}_A + \hat{V}_{FA}(\hat{\mathbf{R}}) + \hat{V}_{AE}(\hat{\mathbf{R}}), \tag{2.1}$$

where $\hat{V}_{FA}$ and $\hat{V}_{AE}$ represent a generical potential interaction between laser field and atomic system and between atomic system and environment. M is the mass of the atom, while $\hat{\mathbf{P}} = -i\hbar\nabla_{\hat{\mathbf{R}}}$ and $\hat{\mathbf{R}}$ are the momentum and position operators of the particle.
Now we need to identify the force applied by the laser field on the atom, therefore we can write:

$$\begin{aligned} \hat{\mathbf{F}} = \tfrac{d\hat{\mathbf{P}}}{dt} = \tfrac{i}{\hbar}\left[\hat{H}, \hat{\mathbf{P}}\right] = -\nabla_{\hat{\mathbf{R}}}\hat{H} \\ = -\nabla_{\mathbf{R}}\hat{V}_{FA}(\hat{\mathbf{R}}) - \nabla_{\hat{\mathbf{R}}}\hat{V}_{AE}(\hat{\mathbf{R}}) \end{aligned}, \tag{2.2}$$

where the laser-atom interaction could be represented, as shown in Eq (2.1), by $\hat{V}_{FA}(\mathbf{R}) = -\mathbf{d}\cdot\mathbf{E}(\hat{\mathbf{R}})$ and $\mathbf{E} = \mathbf{e}E_0(\hat{\mathbf{R}})\cos(\omega t + \phi)$ is the electric field associated with the laser beam having amplitude $E_0(\hat{\mathbf{R}})$, polarization $\mathbf{e}$, frequency ω ($2\pi\nu$) and phase $\phi(\hat{\mathbf{R}})$.
We can now consider the expectation value of the force operator over the state of the system:

$$\mathbf{F} = <\hat{\mathbf{F}}> = <\nabla\mathbf{d}\cdot\mathbf{E}(\hat{\mathbf{R}})> - <\hat{V}_{AE}(\hat{\mathbf{R}})>, \tag{2.3}$$

but the second term is neglectable under the circumstances that guarantee isotropy: in macroscopic events we must consider infinite fluorescence modes that gives zero expectation value in terms of forces in the atom-environment interaction. Therefore, we get the followig result:

$$\mathbf{F} = <\nabla\mathbf{d}_i\mathbf{E}_i(\hat{\mathbf{R}})> \qquad i \in \{x, y, z\} \tag{2.4}$$

Let us now proceed with an *adiabatic approximation*: we will consider a system internally evolving for a time scale much smaller than the external one ($T_{int} \ll T_{est}$). This gives the following results:
-We can now consider $\mathbf{R}, \mathbf{P}$ as classical variables, i.e. not operators anymore.
-A stationary internal state can be identified by the the stationary Optical Bloch Equations (OBE) solutions (Sec.3.3). We therefore obtain:

$$\mathbf{F} = <\hat{d}_i\nabla E_i(\mathbf{R})> + <\nabla\hat{d}_i> E_i(\mathbf{R}), \tag{2.5}$$

where the second term is neglectable since *adiabatic approximation* makes the $<\nabla\hat{d}_i>$ contribution fade out quickly. Proceeding with our considerations:

$$\mathbf{F} = <\hat{d}_i>\nabla E_i(\mathbf{R}) = d_i^{st}\nabla E_i(\mathbf{R}). \tag{2.6}$$

We should now estimate "steady state" electric dipole moment d_i^{st}. Calculating it with the stationary solution of the OBE, we can obtain that the electric field induces

an electric dipole oscillating at the frequency of the laser radiation (Appendix A). Here the stationary - under *adiabatic aproximation* - solutions:

$$\begin{cases} u^{st} = \frac{\Omega\delta}{\delta^2+\gamma^2/4+\Omega^2/2} \\ \\ v^{st} = \frac{\Omega\gamma/2}{\delta^2+\gamma^2/4+\Omega^2/2} \end{cases}, \tag{2.7}$$

with Ω, δ and γ the already defined parameters: Rabi Frequency, detuning between atomic level and electric field frequency and the linewidth of the atomic transition. The induced dipole is composed of two terms, one in phase with the electric field and one out of phase by 90°. Substituting the expression for d_i^{st} in the equation before and averaging for long times the force becomes:

$$\mathbf{F} = -\frac{\hbar\nabla\Omega}{2}u^{st} - \frac{\hbar\Omega\nabla\phi}{2}v^{st}, \tag{2.8}$$

which splits the total force in two different contributions, Dipole Force and Radiation Pression Force, respectively. Let us focus now on the first term: the dipole force is a conservative contribution that corresponds to the in-phase oscillation of the induced electric dipole moment, while the radiation pressure is the dissipative term that is used to slow down and cool the atoms. The dipole force, that guarantees the trapping of the atom, is dominant for large detunings, namely for $\delta >> \gamma, \Omega$; we therefore can think of F_{dip} as $-\nabla U_{dip}$, having defined the dipole potential:

$$U_{dip} = \frac{\hbar\delta}{2}\log\left(1 + \frac{\Omega^2/2}{\delta^2+\gamma^2/4}\right) \sim E^2/\delta, \tag{2.9}$$

valid in sub-saturation regime ($d \sim \Omega \sim E$), since the logarithm can be expanded at the first order in Taylor series because we are considering the $\delta >> \gamma, \omega$ regime. Moreover, we notice that the Dipole Potential is proportional to the square of the electric field over the detuning; if we now observe that the intensity I is proportional to the square of the electric field we obtain the last proportionality relation: $U_{dip} \sim I/\delta$.

When the detuning becomes comparable to the energy difference between electronic levels, the two-level approximation breaks down and one has to resort to a more complete expression, taking into account the coupling of the ground state to different excited levels j:

$$U_{dip}(\mathbf{R}) = -\frac{3\pi c^2}{2\omega_\gamma^3}\sum_j \left(\frac{\Gamma_j}{\omega_L - \omega_j} + \frac{\Gamma_j}{\omega_L + \omega_j}\right) \cdot I(\mathbf{R}), \tag{2.10}$$

where ω_L is the frequency of the laser beam, Γ_j and ω_j are the linewidths and the frequencies of all the j-th transitions. The dipole potential can also be interpreted as a light-shift of the atomic levels induced by the non-resonant interaction [**31**].

The next step to obtain an analytic expression for the Dipole Potential is to determine the intensity profile of the laser beam. It well known, as in [**32**], that a Gaussian beam is a good representation of a propagating laser beam, ruled by the following profile:

$$I(r,z) = \frac{2Po}{\pi W^2(z)}e^{-2r^2/W^2(z)}, \tag{2.11}$$

where $r = \sqrt{x^2 + y^2}$ is the radial coordinate, z the axial coordinate (propagation direction), Po is the power of the laser beam and $W(z)$ is the beam size of the laser beam at propagation distance z. $W(z)$ is characterized by beam waist W_0 and Rayleigh length $z_R = \pi W_0^2/\lambda$ - for a λ wavelength laser - according to the following relation:

$$W(z) = W_0\sqrt{1 + (z/z_r)^2}. \tag{2.12}$$

The laser beam that we will use for generating the optical tweezers is a "Matisse Syrah" manufactured by *Spectra-Physics* that is tuned to work around 813 nm, *Titanium-Sapphire laser*. This wavelength is one of the so-called magic wavelengths for the ultranarrow optical clock transition connecting the ground state $^1S_0$ and the metastable state $^3P_0$. For this specific wavelength the light shift is the same for both the levels, therefore the transition frequency is not shifted by the trapping light, which is highly beneficial for metrologic applications exploiting the $^1S_0 \leftrightarrow ^3P_0$ transition.
The laser beam coming out of its cavity is slightly elliptic, having the waists measured along the x and y axes:

$$\begin{cases} W_{0,x} = (1.024 \pm 0.009)\ \text{mm} \\ W_{0,y} = (0.974 \pm 0.011)\ \text{mm} \end{cases} . \tag{2.13}$$

The Rayleigh length is approximately $z_R = (4.15 \pm 0.07)$ m . The beam is deflected by the couple of acousto-optic deflectors in order to create multiple beams, and then is focused by a microscope objective to reduce the beam sizes to a micrometer lengthscale.

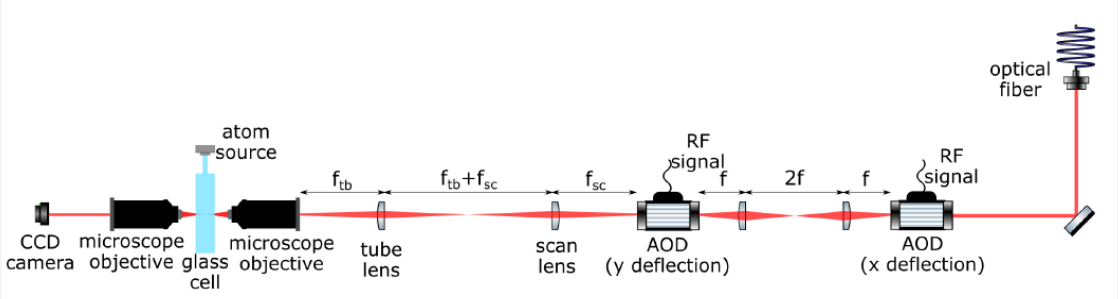

Figure 2.6: Schematic representation of the basic components of the apparatus for the creation of arrays of optical tweezers. A couple of crossed AODs can create several deflected beams covering the whole solid angle. The beams are focused via a microscope objective into a glass cell where the atoms are prepared in a MOT. A second microscope objective recollects the tweezers light. Image taken from [**2**].

The main components of the apparatus that will be used to create the Optical Tweezers are presented in Fig. 2.6. The core of this apparatus is the glass cell, where atoms are trapped and cooled in a Magneto Optical Trap (MOT). The glass cell is engineered in such a way to provide the maximum optical access possible. The array of optical tweezers is superimposed to the MOT region in order to trap individual atoms. Given this optical setup, we can calculate the expected beam size of the tweezers and their separation after the microscope objective, in the glass cell. We can calculate these quantities as a function of the focal lengths of scan and tube lenses f_{sc} and f_{tb} (the pair of lenses before the objective in figure 3.1) and the

effective focal length of the objective f_o, also called working distance (WD). First off, the divergence of a Gaussian beam with waist W_i has to be recalled:

$$\theta_0 = \frac{\lambda}{\pi W_i}. \tag{2.14}$$

Therefore, the beam size of the tweezer after being focused by the objective is then:

$$W_{tweez} = f_o \cdot \theta_1 = f_o \cdot \theta_0 \cdot \frac{f_{sc}}{f_{tb}} = \frac{\lambda f_o}{\pi W_i} \frac{f_{sc}}{f_{tb}}, \tag{2.15}$$

where θ_1 is the divergence of the Gaussian beam at the input of the objective that is expressed as a function of the divergence θ_0 before the scan-tube lenses system. Scan lens and tube lens focal lengths are used to calculate, in geometrical optics, the magnification/reduction of the divergence angle. The distance between a pair of tweezers generated at RF frequencies f_1 and f_2, such that the difference is Δf, is instead [**30**]:

$$d_{tweez} = 2 f_o \tan\left(\frac{\Delta\theta}{2}\right) = 2 f_o \tan\left(\frac{\Delta f}{2 v_s} \lambda \frac{f_{sc}}{f_{tb}}\right); \tag{2.16}$$

for typical values - such $\lambda = 813$nm, $W_i = 1$ mm, $f_o = 5$ mm, $f_{sc} = f_{tb} = 200$ mm, $\Delta f = 1$ MHz and $v_s = 650$ m/s - we get $W_{tweez} = 1.3$ μm and $d_{tweez} = 6.3$ μm. Feeding the W_{tweez} estimated value into equation (2.11), the intensity at the center of the trap, where the exponential factor is equal to 1, is $I_0 = 3.8 \cdot 10^8$ W/m^2 for a power $Po = 1$ mW. This huge intensity of the optical tweezers trap is the result of the tight focusing of the laser beams, and allows us to trap, with a little amount of laser power (for example 1 mW), atoms that have relative high temperature of few μK. If $Po = 1$ mW is enough for an optical tweezer that holds one atom, we might produce a few hundreds of traps within the same array, since the power is above 7 W right out of the laser cavity.

The parameters used to obtain this potential are $Po = 1$ mW, $W_{tweez} = 1$ μm and $\lambda = 813$ nm. Only the two main transitions of Sr atoms were considered, that is the ${}^1S_0 \rightarrow {}^1P_1$ and the ${}^1S_0 \rightarrow {}^3P_1$, because they have the largest linewidths, and the trap depth is converted in a temperature scale (μK). Approximating the dipole potential to a harmonic trap, it is possible to calculate the harmonic **trap frequencies**. This would be fundamental for sideband considerations in imaging processes. In figures below, we report a few values for the power depth of the trap P in mW, , and the corresponding trapping frequency for the x (radial) and z (axial) directions in kHz, following the relations:

$$\begin{cases} \omega_z = \sqrt{\frac{2U_0}{M z_R^2}} \\ \omega_x = \sqrt{\frac{4U_0}{M W_0^2}} \end{cases} \tag{2.17}$$

All the parameters are obtained for fixed $\lambda = 813$ nm and $W_{tweez} = 1$ μm.

In order to avoid undesired Stark effects (different energy shifts) we determine two different *magical* λ: 515.2 nm and 813.4 nm. 515 nm is an interesting wavelength for trapping Sr because it is available at high power ($\sim$ 10 W) and is also power efficient due to fact that it is a relatively short wavelength (leading to a tight tweezer waist) and having large ground state polarizability. Furthermore, it offers

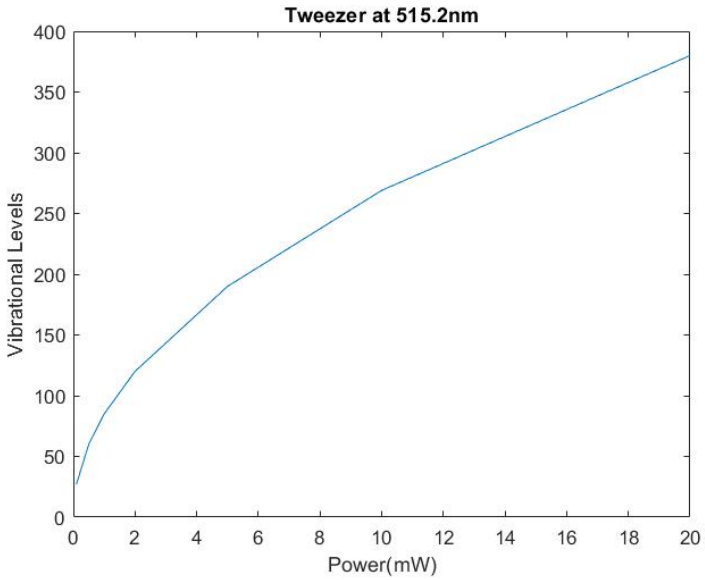

Figure 2.7: Vibrational Levels Number for different values of beam power.

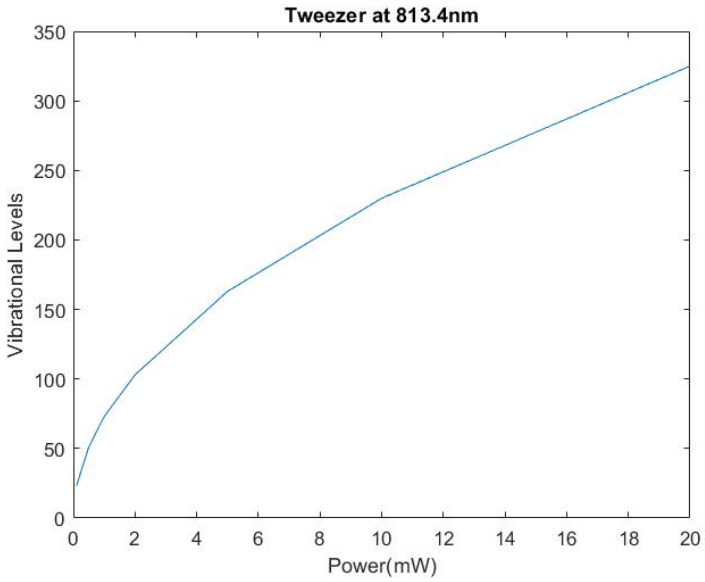

Figure 2.8: Vibrational Levels Number for different values of beam power.

transitions to both more weakly and more strongly trapped sub-levels of $5s5p\,^3P_1$. If desired, 515 nm traps can also be tuned to a magic condition for the red transition with polarization or fields. However, [**24**] has shown that 515 nm tweezers have unavoidable issues that lead to atom loss at a certain level during imaging. Finally, 515 nm is not magic for the clock transition (and cannot be made so), so highly coherent clock operation with 515 nm traps is ruled out.
On the other hand, 813.4 nm is the magic wavelength for clock tranistion $^1S_0 \rightarrow ^3P_0$. In Fig. 2.7 and 2.8 we can see the profile of vibrational trapped levels in optical tweezers made by 515 nm and 813 nm laser beams respectively.

2.3 Time-dependent trapping models

In this section we will recall two problems regarding the trapping and the transport of atoms. These two topics are relevant in the context of the rearrangement of the array that is performed to create a defect-free pattern. An array of static OTs can be created using the pair of crossed AODs by driving them with multiple frequency components RF signals. As the loading of this array with cold atoms will be non deterministic, we need to implement rearrangement techniques to obtain the desired pattern of trapped atoms, as developed in Chapter 4. For 1D patterns the rearrangement consists in compacting only those tweezers that are filled to form a defect-free array of arbitrarily spaced OTs [**33**, **34**]. To move one tweezer along the line, a frequency sweep is applied to the corresponding frequency component of the RF signal that drives the AOD. The sweep can be linear, resulting in a uniform rectilinear motion (URM) for the atom, but also more complicated equations for the tweezer's motion can be explored.

The problem of finding the best equation for the transport of the atom has been resolved by Ref.[**2**]. For arbitrary 2D patterns this approach cannot be used, because only separable 2D patterns can be created with two orthogonal AODs, which forbid arbitrary movements of individual OTs. To overcome this limitation, the soltion coomly adopted is that of combining arbitrary 2D patterns created by SLMs with an additional OT that moves the atoms one at time.

Alternatively, exploiting time-averaged potentials has been considered as an alternative method. In Ref.[**2**] the effects of the periodic on/off switching of a single static tweezer were studied to understand the feasibility of such an approach. The constraints for the trapping of the atoms were studied as function of the laser power generating the tweezer and the frequency at which the periodic switching of the potential is driven. A further approch is the study of quantum-mechanical evolution in a very simplified case, that of a *release and recapture* process, which is, however, highly relevant to the experimental implementation of Rydberg experiments. Results of [**2**] in Fig. 2.9.

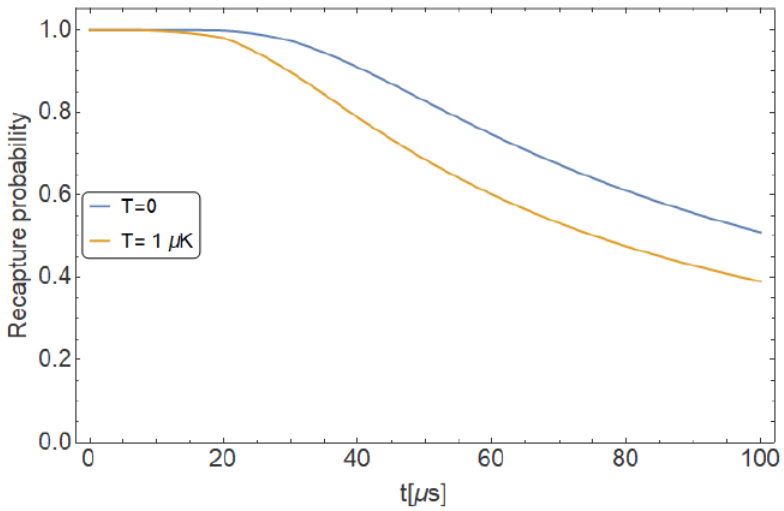

Figure 2.9: Recapture probability as a function of time in the case at zero temperature and finite temperature as found by [**2**].

This whole optimization has guaranteed an average moving time of 10 μs per $1\mu m$, without losing atoms.

The atoms initially loaded randomly in the array (100 ms) are imaged one first time ($\sim$ 10 ms) to determine the sequence of moves for the reordering (50 ms). After the reordering a second imaging stage ($\sim$ 10 ms) is needed to check whether the reordering worked properly or not. Then the Rydberg excitation takes place and finally a third imaging stage (30 ms) allows for the detection of the atomic state [**24**]. The overall timescale should then be around 200 ms. Indeed, we will try to minimize it.

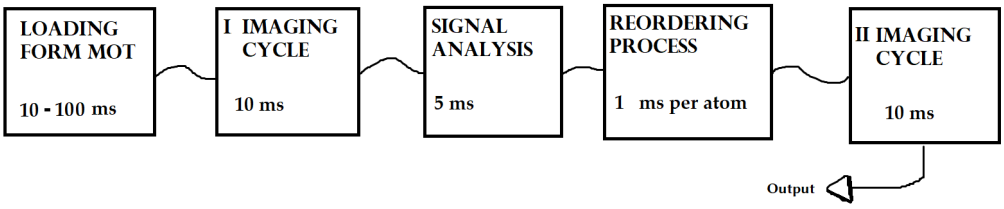

Figure 2.10: Total experiment processes time scheme.

Chapter 3

Imaging Process

Imaging a single atom is a delicate process where every photons counts, and this requires us to think about certain concepts more deeply than one would when imaging e.g. a bulk gas.
For a trapped atom to be detected with high fidelity, it needs to scatter a sufficient amount of photons into an imaging system so as to be well-distinguished from a background signal. If the atom scatteres a high number of photons, without cooling processes, it gets hotter - by a Photon Recoil energy E_R any time it spontaneously emits a photon - and it seriously risks to get lost in few ms. We will discuss about these heating and cooling processes in Section 3.3.2.

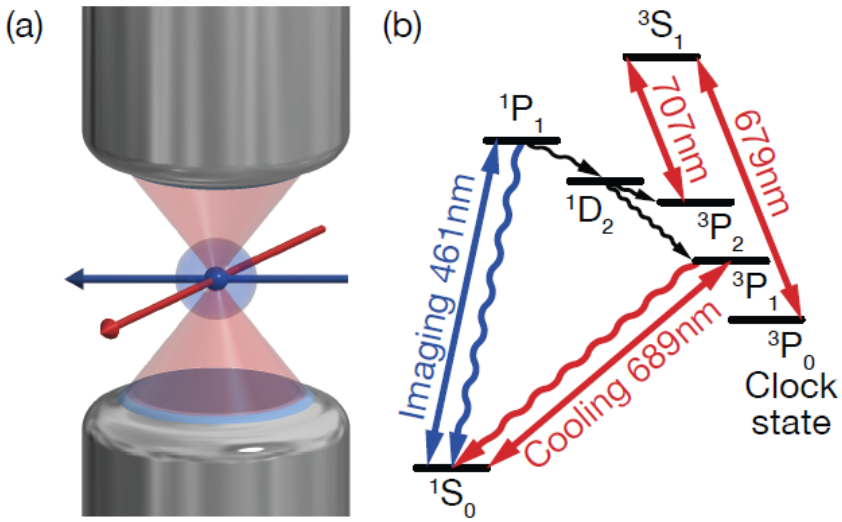

Figure 3.1: Imaging setup. (a) An atom in a tweezer is illuminated by a blue (461 nm) imaging beam while being cooled by a red (689 nm) cooling beam. The imaging beam may be retro-reflected or not. One objective creates the tweezer, and fluorescence can be imaged through either or both objectives. Not shown: repump beams. (b) A level structure indicating the relevant transitions during imaging. In addition to the imaging and cooling beams, two beams at 679 nm and 707 nm are used to repump atom out of the $5s5p\ ^3P_2$ and $5s5p\ ^3P_0$ metastable states. Images taken from [**24**].

The figure above shows a typical imaging setup. Fluorescence is induced by a 461 nm beam, near-resonant with the blue transition, while simultaneous cooling is done by a beam at 689 nm. A single non-reflected cooling beam is sufficient to cool all direction during imaging phase. Any way, multiple (and possibly retro-reflected)

beams can be used [**26**], but care must be taken that interference does not occur (by e.g. piezo-modulating a mirror).

A repump beam at 707 nm is used to repump atoms out of the $5s5p\ ^3P_2$ metastable state into the $5s5p\ ^3P_1$ state, which decays back into the imaging cycle. $5s5p\ ^3P_2$ is populated via decay from $5s4d\ ^1D_2$, which is in turn populated by a weak decay channel from the excited state of the blue transition $5s5p\ ^1P_1$. We will see soon that the polarizability of $5s4d\ ^1D_2$ at the trapping wavelength is important. If this state is not sufficiently trapped, the atom can leave the trap before it decays out of this state. Since $5s5p\ ^3P_2$ is repumped via $5s6s\ ^3S_1$, part of the population ends up in $5s5p\ ^3P_0$, so a $679nm$ repump is needed to excite these atoms back to $5s6s\ ^3S_1$. The combination of the 707 nm and 679 nm beams eventually repumps all population in the metastable $5s5p\ ^3P_{0,2}$ states back to the imaging/cooling cycle, typically on the timescale of a few μs. We further note that both of these repump wavelengths are also necessary when exciting the red (689 nm) transition in a trap, as the trap light can cause Raman scattering between the various states of the $5s6s\ ^3P_J$ manifold. Finally, we can note that it is entirely possible to use red cooling beam as both a cooling and imaging beam, i.e. such that red fluorescence is collected instead of blue cooling, but this differs on imaging time taking way more than our setup. Once again, let me remind that all we want to do is to minimize the whole process time.

3.1 Imaging beam

Here we provide a few considerations for the blue imaging beam. First, we consider whether it needs to be retro-reflected. One may suspect that a sideband-unresolved beam pointed along only one direction can create an "unbalanced" radiation pressure force $F = \hbar k \Gamma_s$ on the atom (with with Γ_s the scattering rate) such that the atom is pushed away from the tweezer in that direction. However, we have found that for the scattering rates we typically use that retro-reflection is not important. Classically, such a force applied to a harmonically trapped (ω_T) particle simply shifts its equilibrium position by $\Delta x = F/m\omega_T^2$. If Δx is small enough, this effect is unimportant. Nonetheless, this fact makes it prudent to point the imaging beam along the radial tweezer direction so as to not apply a force along the weakly trapped axial direction.
Furthermore, the sign of this detuning is chosen to be such that when the atom heats and attains a higher energy in the trap, its scattering rate goes down. This is heuristically done to reduce heating for higher-temperature atoms. The actual sign of detuning that fulfills this condition depends on the differential polarizability of the blue transition. At a trap wavelength of 813.4 nm, the blue excited state $5s5p\ ^1P_1$ is more strongly trapped than the ground state, so a red detuning is used. At 515.2 nm, the situation is reversed, and in fact here the excited state is anti-trapped.

As to the size of the beam, it is recommended to choose a beam large enough such that it illuminates the entire tweezer array uniformly. However, larger beams also produce greater background scatter. If possible, the beam should be made to avoid scattering off of surfaces near the imaging objective.

3.2 Dipole Radiation Pattern

The scattering of fluorescence photons is not isotropic. The dipole radiation pattern is a function defined on a sphere giving the probability that an atom will scatter a photon in a particular direction. We note that the results presented here are essentially identical to those of classical electrodynamics, particularly in the context of electromagnetic radiation from oscillating dipoles. We will follow a treatment given in [**35**]. For an excited state with total angular momentum quantum number decaying into a ground state, we define a dipole radiation pattern operator on the subspace of the excited manifold as

$$\mathcal{D}(\theta,\phi) = (\frac{2J_e+1}{2J_g+1}) \sum_{q,q'\in\{0,1\}} f_{qq'}(\theta,\phi) \times \Sigma, \tag{3.1}$$

where

$$\begin{aligned} \Sigma = \sum_{m_e} |J_e, m_e\rangle \langle J_e, m_e + q - q'| \times ... \\ ... \times \langle J_e, m_e + q | J_e, m_e + q - q'; 1q' \rangle \langle J_e, m_e + q | J_e, m_e + q - q'; 1q \rangle \end{aligned} \tag{3.2}$$

and

$$f_{qq'}(\theta,\phi) = \frac{1}{4\pi}(\delta_{qq} - (-1)^q \sqrt{6\pi} \begin{pmatrix} 1 & 1 & 2 \\ -q & q' & q-q' \end{pmatrix} Y_2^{q-q'}(\theta,\phi)), \tag{3.3}$$

with $Y_l^m(\theta,\phi)$ spherical harmonic and the two-rows matrix is a Wigner 3-j symbol. It should be clear that integrating over the entire sphere, we get $\int d\Omega f_{qq'}(\theta,\phi) = \delta_{qq'}$. This formulation allows us to compute the dipole radiation pattern for an arbitrary state in the excited manifold by taking the expectation value, given by

$$D(\theta,\phi) = \langle \psi_e | \mathcal{D}(\theta,\phi) | \psi_e \rangle . \tag{3.4}$$

This result sums over all polarizations of the emitted photon, therefore applications where only one particular polarization is to be imaged will require a more sophistcated anlysis. This is the way we will procede.
We can simplify our analysis by assuming that the atom is in a certain energy eigenstate and that eigenstate is also an eigenstate of angular momentum along some quantization axis $\hat{z}$. Since our excited states of interest have $J_e = 1$ and $J_g = 0$, we will also focus only on this situaton. Then only the $q = q' = -m_e$ terms are nonzero and the dipole radiation pattern simplifies to

$$\begin{aligned} D(\theta,\phi) &= \tfrac{3}{8\pi}\sin^2(\theta) && \text{if } m_e = 0 \\ D(\theta,\phi) &= \tfrac{3}{16\pi}(1+\cos^2(\theta)) && \text{if } m_e = \pm 1 \end{aligned} \tag{3.5}$$

where θ is the angle with respect to the quantization axis $\hat{z}$.
This result has important implications for imaging, as it is prudent to orient the dipole radiation pattern such that scattering into the imaging objective is maximized. For an $m_e = 0$ state, this happens when the quantization axis is oriented in such that the objective is at $\theta = 90^o$. On the other hand, for an $m_e = \pm 1$ state $\theta = 0^o$ is the optimal choice.
We will now calculate the collection efficiency C for several cases and an objective

with numerical aperture $NA = \sin\alpha$, where α is the maximal collection angle as measured from optical axis. We define the collection efficiency as the fraction of all scattered photons that end up being collected by the imaging objective. We note that the realization of these scenarios requires excitation to an appropriate ψ_e, i.e. an appropriate choice of imaging beam polarization as well as consideration of any degeneracy-breaking fields such a magnetic field or optical trap.

Case (1): $m_e = 0$, objective at $\theta = 90^o$.
It is most convenient here to rotate the coordinate frame by 90^o by rotating the $\hat{z}$ into the $\hat{y}$, where we now have new spherical coordinates θ', ϕ' such that the objective is $\theta' = 0$. We can see $\sin^2(\theta) = \cos^2(\theta') + \sin^2(\theta')\cos^2(\phi')$. Then we get

$$C_{(1)}(\alpha) = \frac{3}{8\pi}\int_0^{\alpha}\int_0^{2\pi} \sin(\theta')(\cos^2(\theta') + \sin^2(\theta')\cos^2(\phi'))d\phi' d\theta' \tag{3.6}$$

$$= \frac{1}{8}(4 - \cos(\alpha)(3 + \cos^2(\alpha))) \tag{3.7}$$

$$= \frac{1}{8}(4 - (NA^2 - 4)\sqrt{1 - NA^2}). \tag{3.8}$$

For $NA = 0.5$, we have $C_{(1)} = 0.094$.

Case (2): $m_e = \pm 1$, objective at $\theta = 0^o$.
We can straightforwardly evaluate it in the original frame as

$$C_{(2)}(\alpha) = \frac{3}{16\pi}\int_0^{\alpha}\int_0^{2\pi} \sin(\theta)(1 + cos^2(\theta)d\phi d\theta \tag{3.9}$$

$$= \frac{1}{8}(4 + (NA^2 - 4)\sqrt{1 - NA^2}), \tag{3.10}$$

that is exactly the same result as in (1).

Case (3):$m_e = 0$, objective at $\theta = 0$.
This choice is defenitely the worst and therefore to be avoided.

$$C_{(3)}(\alpha) = \frac{3}{8\pi}\int_0^{\alpha}\int_0^{2\pi} \sin(\theta)\sin^2(\theta)d\phi d\theta \tag{3.11}$$

$$= (2 + \cos(\alpha))\sin^4(\frac{\alpha}{2}), \tag{3.12}$$

that means for $NA = 0.5$ a $C_{(3)} = 0.013$, about 14% of $C_{(1)}$.

Case (4): Isotropic emission.
This case is not achievable for a polarized laser beam, i.e. an atom gets excited to a not-balanced angular momentum states ensemble, neertheless we will use it as reference value:

$$C_{(4)}(\alpha) = \frac{1}{4\pi}\int_0^{\alpha}\int_0^{2\pi} \sin(\theta)d\phi d\theta \tag{3.13}$$

$$= \frac{1}{2}(1 - \sqrt{1 - NA^2}). \tag{3.14}$$

For $NA = 0.5$, $C_{(4)} = 0.067$.

3.3 Fluorescence and Cooling Simulation

In this section, we will remind some central aspects of single-atom physics starting from a semi-classical point of view, passing to a more computational one. We will start treating all the fondumental tranistion events in specific two-level systems to sum everythings up (fluorescence and cooling) in a three-level system.
A good starting point would be the separation between atomic classical and quantum natures: more specifically we use $\mathbf{P}$ and $\mathbf{R}$ as atom center of mass variables and $\mathbf{p}$ and $\mathbf{r}$ for electron relative motion, subject to optical transitions with respect to the nucleus. We can always describe the global atomic system as ruled by this atomic Hamiltonian Operator:

$$H_A = \frac{\mathbf{P}^2}{2M} + \frac{\mathbf{p}^2}{2\mu} + V(\mathbf{R}), \tag{3.15}$$

where $\mathbf{P}$ and $\mathbf{p}$ are the total and relative momentum operators, $\mathbf{R}$ is the free position operator, M and μ are atomic total and reduced mass with respect to the center of mass. V is a generical potential energy operator. The first term represents the most classical nature of the atom: the evolution of its center of mass. The second terms has to be studied as quantum contribution.

Let me get started with a simple two-level system describing in first approximation our Strontium atoms imaging cycle. Let $\hbar\omega_0$ be the energy difference between the ground state $|g\rangle$ and the excited state $|e\rangle$, and $\vec{E} = \vec{E_0}\cos(\omega t)$ be the classical form of an electric monochromatic field inciding on the atom. In our two-level approximation, it is practical to write our equation in matrix representation, where $|g\rangle = \begin{pmatrix} 0 \\ 1 \end{pmatrix}$ and $|e\rangle = \begin{pmatrix} 1 \\ 0 \end{pmatrix}$. Without any external interaction, the unperturbed atomic Hamiltonian would be

$$H_A = \hbar\omega_g |g\rangle \langle g| + \hbar\omega_e |e\rangle \langle e| \tag{3.16}$$

meanwhile the electron-nucleus interaction Hamiltonian would be

$$H_I = -\vec{d} \cdot \vec{E} = e\vec{r} \cdot \vec{E} \tag{3.17}$$

where $\vec{d} = -e\vec{r}$ is the atom polarization vector and $\vec{r}$ the electron postion operator. Now, since H is not diagonal on (e,g) basis any longer, we have to study the interaction term:

$$\langle e| H_I |g\rangle = e \int \psi_e^*(\vec{r} \cdot \vec{E})\psi_g d\vec{r} = e\vec{E_0}\cos(\omega t)\vec{\mu_{eg}} \tag{3.18}$$

where we have introduced the transition matrix element:

$$\vec{\mu_{eg}} = \int \psi_e^* \vec{r} \psi_g d\vec{r}. \tag{3.19}$$

This means that the Reduced Dipole Matrix Element RDME= $e\vec{\mu}_{e,g}$. Finally, we can define the "Rabi frequency":

$$\Omega = e\vec{\mu_{eg}} \cdot \vec{E_0}/\hbar : \tag{3.20}$$

by this, since $\vec{r}$ parity does not allow diagonal terms, it is possible to write:

$$H_I = \hbar\Omega\cos(\omega t)[|e\rangle \langle g| + |g\rangle \langle e|]. \tag{3.21}$$

Summing everything up, we eventually get

$$H = H_A + H_I = \hbar \begin{pmatrix} \omega_e & \Omega\cos(\omega t) \\ \Omega^* \cos(\omega t) & \omega_g \end{pmatrix}. \tag{3.22}$$

Taking Schroedinger's Equation $i\hbar\partial_t |\psi\rangle = H |\psi\rangle$, and initializing the state $|\psi\rangle = a_g |g\rangle + a_e |e\rangle$, we can write:

$$\begin{cases} i\dot{a_g} = \Omega^* \cos(\omega t) a_e \\ i\dot{a_e} = \Omega \cos(\omega t) a_g + \omega_0 a_e \end{cases} \tag{3.23}$$

We will work typicaly with $\omega_0 \sim 10^{14} - 10^{15}$ Hz and $\Omega \sim 10^6$ Hz. Starting now from this Hamiltonian:

$$H = \hbar \begin{pmatrix} \omega_0 & \Omega\cos(\omega t) \\ \Omega^* \cos(\omega t) & 0 \end{pmatrix} \tag{3.24}$$

if detuning $\delta = \omega - \omega_0 \ll \omega + \omega_0$ and $\Omega \ll \omega$ we can now call the *Rotation Wave Approximation*, which allows to neglect the terms $e^{\pm i2\omega t}$ in this variables transformation:

$$\begin{cases} \tilde{a_g} = a_g \\ \tilde{a_e} = a_e e^{i\omega t} \end{cases} . \tag{3.25}$$

We can reshape Eq.(3.25) in the following way

$$\begin{cases} \dot{\tilde{a}}_g = \frac{\Omega}{2}\, \tilde{a}_e \\ \dot{\tilde{a}}_e = \frac{\Omega^*}{2} \tilde{a}_g - \delta \tilde{a}_e \end{cases} \tag{3.26}$$

that represents the trasformed Hamiltonian:

$$\tilde{H} = \hbar \begin{pmatrix} \delta & \Omega^*/2 \\ \Omega/2 & 0 \end{pmatrix}. \tag{3.27}$$

In this transfomation eigenstates population amplitudes are conserved: $|\tilde{a_{g,e}}|^2 = |a_{g,e}|^2$. With legitimate initial conditions $\dot{\tilde{a}}_g(0) = 1$ and $\dot{\tilde{a}}_e(0) = 0$, we get these time-dependent solutions:

$$\begin{cases} \tilde{a}_g(t) = e^{i\delta t/2}(\cos\Omega' t/2 - i\frac{\delta}{\Omega'} sin\Omega' t/2) \\ \tilde{a}_e(t) = e^{i\delta t/2}(-i\frac{\Omega}{\Omega'} sin\Omega' t/2) \end{cases} \tag{3.28}$$

with $\Omega' = \sqrt{|\Omega|^2 + \delta^2}$ *Generalized Rabi Frequency.* Those are *Rabi Oscillations* and describe the periodic process of absorption and stimulated emission in our two-level systems, with frequency and amplitude depending on δ.

It is going to be useful to introduce operator matrix representation starting with Pauli matrices for the atomic system:

$$\sigma_z = \begin{pmatrix} 1 & 0 \\ 0 & -1 \end{pmatrix} \qquad \sigma_x = \begin{pmatrix} 0 & 1 \\ 1 & 0 \end{pmatrix} \tag{3.29}$$

on the same atomic basis $|g\rangle = \begin{pmatrix} 0 \\ 1 \end{pmatrix}$ and $|e\rangle = \begin{pmatrix} 1 \\ 0 \end{pmatrix}$. We can also write $\sigma_x = \sigma_+ + \sigma_-$, i.e. the sum of "creation" and "destruction" operators of atomic state:

$$\sigma_+ = \begin{pmatrix} 0 & 1 \\ 0 & 0 \end{pmatrix} \qquad \sigma_- = \begin{pmatrix} 0 & 0 \\ 1 & 0 \end{pmatrix} \tag{3.30}$$

They act on atomic state in the following way:

$$\begin{array}{ll} \sigma_+ |g\rangle = |e\rangle & \sigma_+ |e\rangle = 0 \\ \sigma_- |g\rangle = 0 & \sigma_- |e\rangle = |g\rangle \end{array} \tag{3.31}$$

Identity operator is simply $\mathbb{1}_A = \mathbb{1}_2$. For Harmonic Oscillators, we can introduce "creation" and "destruction" operators of bosonic states, in this case of electromagnetic field:

$$\begin{array}{ll} |n\rangle_F = \frac{(a^\dagger)^n}{\sqrt{n!}} |0\rangle_F & n \geq 0 \\ a^\dagger |n\rangle_F = \sqrt{n+1}\, |n+1\rangle_F & a |n\rangle_F = \sqrt{n}\, |n-1\rangle_F . \end{array} \tag{3.32}$$

In this way it is possible to define the Number Operator $N_F = a^\dagger a$. We can now write the Atomic and Electro-Magnetic Hamiltonian as combination of those operators:

$$H/\hbar = \frac{\omega_0}{2}\sigma_z \otimes \mathbb{1}_F + \omega \mathbb{1}_A \otimes N_F + \frac{\Omega}{2}(\sigma_+ + \sigma_-) \otimes (a^\dagger + a). \tag{3.33}$$

Reduced dipole matrix elements are listed in various ways in the wider literature and it is often confusing to convert from one convention to the other. We will not give a comprehensive review of all of them here, but we will at least relate the RDME as defined through the Wigner-Eckart theorem:

$$\langle \beta m_J | \, \mathbf{d}_q \, | \beta' m'_J \rangle = \frac{1}{\sqrt{2J+1}} \langle \beta | \, |d_q| \, | \beta' \rangle \, \langle J m_J | \, J' m'_J; 1q \tag{3.34}$$

to an unambiguous experimental quantity: the decay rate.

For an allowed transition $|\beta\rangle \rightarrow |\beta'\rangle$ where $|\beta'\rangle$ is higher in energy, there is generally some decay rate $\Gamma_{\beta' - \beta}$ from $|\beta'\rangle$ to $|\beta\rangle$. Note that this decay rate does not depend on magnetic sub-level. Also, note that this may not be the total decay rate of $|\beta'\rangle$ if it decays to states other than $|\beta\rangle$. Then the squared RDME between the two states is given by:

$$| \langle \beta | \, \mathbf{d} \, | \beta' \rangle \, |^2 = \frac{3\pi\epsilon_0 \hbar c^3}{\omega^3_{\beta'\beta}} (2J'+1) \Gamma_{\beta' - \beta} \tag{3.35}$$

Like for Eq. (3.1), note that our convention has a factor of $(2J'+1)$ which is not found in some other conventions, e.g. in that of [**36**].

3.3.1 Spontaneous Emission in a Two-Level System

Once the atomhas been excited to the $|e\rangle$ state by a single mode - let us say $(\vec{k}, \omega)$ - of electromagnetic field, it can decay by stimulated emission to the ground state - that frustrates the previous absorption - or by spontaneous emission: in this case it will interact with an infinite amount of e.m.f. modes, not yet occupied by photons, with energy $E_{\vec{k_i},\omega_i} = \hbar\omega_i(n_{\vec{k_i},\omega_i} + 1/2)$ for $n_{\vec{k_i},\omega_i}$ occupation number of i-mode.
This process is characterized by a *free space* rate given by Fermi's golden rule depending on ω_f emission frequency:

$$\gamma(\omega_f) = \frac{e^2 \omega_f^3 |\mu_{eg}|}{3\pi\epsilon_0 \hbar c^3} \tag{3.36}$$

If we now consider an atom excited at a certain time, it will interact with all the modes of e.m.f, and the excited population will incour in an exponential decay, with finite average life time $\tau = 1/\gamma$. If it interacts just with one mode, e.g. imaging laser mode, we will see the same results as in Rabi's model.
It would be useful to continue with State Density Matrix

$$\rho = \begin{pmatrix} \rho_{gg} & \rho_{ge} \\ \rho_{eg} & \rho_{ee} \end{pmatrix} = \begin{pmatrix} |a_g|^2 & a_e^* a_g \\ a_g^* a_e & |a_e|^2 \end{pmatrix} \tag{3.37}$$

and to reshape *Schrödinger Equation* in *Liouville-Von Neumann* form:

$$\dot{\rho} = \frac{1}{i\hbar}[H, \rho]. \tag{3.38}$$

Whitout further ado, let me introduce directly *Bloch Optical Equations* in *RWA*:

$$\begin{cases} \Delta\dot{\tilde{\rho}} = -i(\Omega\tilde{\rho}_{ge} - \Omega^*\tilde{\rho}_{eg}) - \gamma(\Delta\tilde{\rho} + 1) \\ \dot{\tilde{\rho}}_{ge} = i\delta\tilde{\rho}_{eg} + \frac{i}{2}\Omega\Delta\tilde{\rho} - \frac{\gamma}{2}\tilde{\rho}_{eg} \\ \dot{\tilde{\rho}}_{ge} = i\delta\tilde{\rho}_{ge} + \frac{i}{2}\Omega^*\Delta\tilde{\rho} - \frac{\gamma}{2}\tilde{\rho}_{eg} \end{cases} \tag{3.39}$$

with $\Delta\tilde{\rho} = (\tilde{\rho}_{ee} - \tilde{\rho}_{gg})$.
Under initial conditions $\rho = \begin{pmatrix} 0 & 0 \\ 0 & 1 \end{pmatrix}$ we can simulate different evolution of excited state population for different Ω as shown in Fig 3.2 below:

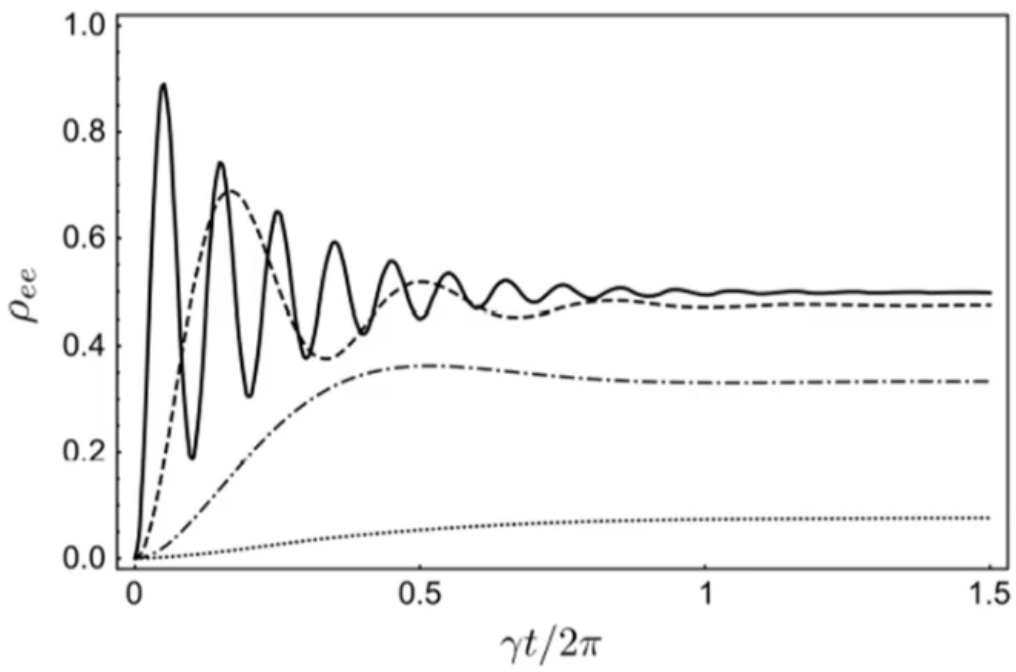

Figure 3.2: Excited state population obtained from integration of equations (2.23). The curves are calculated in resonance $\delta = 0$, fixed γ and different Rabi frequencies: 10γ (solid), 3γ (dashed), 1γ (dash-dotted), 0.3γ(dotted).

In each case, given by different Ωs, we can see the same asymptotic behaviours: *OBE*"steady-state" solutions, i.e. homogeneous solution of equations system (3.37). We can suddenly reach the expression of "steady-state" excited population:

$$\rho_{ee}^{st} = \frac{1 + \Delta\tilde{\rho}^{st}}{2} = \frac{1}{2} \cdot \frac{s}{1+s} \cdot \frac{1}{1 + (2\delta/\gamma_s)^2}, \tag{3.40}$$

where we have introduced the saturation parameter $s = 2|\Omega|^2/\gamma^2$ and the *saturated* linewidth $\gamma_s = \gamma\sqrt{1+s}$ of spontaneous emission.
The saturation parameter s will lead us in the optimization of the imaging process. An other important parameter we can introduce is the scattering rate associated to sucha a transition:

$$\Gamma_s = \gamma_s \rho_{ee}^{st} = \frac{\gamma_s}{2} \cdot \frac{s}{1+s} \cdot \frac{1}{1 + (2\delta/\gamma_s)^2}, \tag{3.41}$$

that represents the rate photons are emitted with in steady conditions for a two-level atomic system.

3.3.2 Cooling Processes

Let me now consider again a two-level atom, in a trap of potential $U(\mathbf{R})$ and driven by a spatialy uniform wave with wavevector $\mathbf{k}$, Rabi frequency Ω and detuning δ. Under these assumptions, the motional plus internal Hamiltonian (still not including fluorescence) in RWA is given by

$$H = \frac{\mathbf{P}^2}{2M} + U(\mathbf{R}) - \hbar\delta \left|e\right\rangle \left\langle e\right| + \frac{\hbar}{2}\Omega(e^{i\mathbf{k}\cdot\mathbf{R}} \left|e\right\rangle \left\langle g\right| + h.c.) \tag{3.42}$$

We now assume that $U(\mathbf{R})$ is approximately harmonic near $\mathbf{R} = 0$ (which is true for tweezers) and that the atom is close to this region. It is here important to highlight that $U(\mathbf{R})$ must be a magic trap, i.e it does not depend on the internal state of the atom.
In this case, the 3D trap will have three geometric principal axes along which we can define trap frequencies $\omega_i = \sqrt{\partial_i^2 U|_{\mathbf{R}=0}/M}$. Let us further assume one of these axes is parallel to $\mathbf{k}$ and say it is $\mathbf{x}$ since its frequency is the highest: let us call it $\omega_T = \omega_x$. The Hamiltonian in this harmonic region will now separate into a sum of components along each direction, with only the component along $\mathbf{x}$ having non-trivial coupling between motion and internal state. We define the harmonic ladder operators $\hat{a} = A_T(\hat{R}_i + \frac{i}{m\omega_T}\hat{P}_i)$, where $A_T = \sqrt{\hbar/M\omega_T}$, and the *Lamb-Dicke parameters*

$$\eta = kA_T, \tag{3.43}$$

Focusing only on the $\mathbf{x}$ component of the Hamiltonian and dropping subscripts, we get

$$H_x = \hbar\omega_x(\hat{a}^\dagger\hat{a} + \frac{1}{2}) - \hbar\delta \left|e\right\rangle \left\langle e\right| + \frac{\hbar}{2}\Omega(e^{i\eta(\hat{a}+\hat{a}^\dagger)} \left|e\right\rangle \left\langle g\right| + h.c.) \tag{3.44}$$

We may recognize $e^{i\eta(\hat{a}+\hat{a}^\dagger)}$ as the momentum displacement operator by $\mathbf{k}$, due to the Photon Recoil $E_R = \frac{\hbar^2k^2}{2M}$. In order to understand how this term affect the dynamics in a trap, we can evaluate its matrix element on a basis of eigenstates of $\hat{N} = \hat{a}^\dagger\hat{a}$.

We can assign two harmonic oscillation eigenstates to ground and excited state: $\phi_g = |m\rangle$ and $\phi_e = |n\rangle$. If ω_T is the trap characteristic frequency then $E_N = \hbar\omega_T(N + 1/2)$ is the energy assigned to each oscillator level. The global ground state wave function will be $|\psi_g\rangle = |g\rangle\,|m\rangle$, and for excited state in analog way.
We can now consider, with $n' = min(n, m)$

$$\langle m|\, e^{i\eta(\hat{a}+\hat{a}^\dagger)}\,|n\rangle = \sqrt{\frac{n'!}{n' + |m-n|}}(i\eta)e^{\eta/2}\mathcal{L}_n'^{|m-n|}(\eta^2), \tag{3.45}$$

where $\mathcal{L}_\beta^\alpha(y)$ is a generalized Laguerre polynomial function. We desire to keep $\eta \ll 1$ in order to proceed in the following calculations.
In this Lamb-Dicke regime, we can now write the Hamiltonian matrix element between $|g\rangle$ and $|e\rangle$ in the following way

$$\langle n|\, e^{i\eta(\hat{a}+\hat{a}^\dagger)}\,|m\rangle\,\frac{\Omega}{2} = \frac{\Omega}{2}\,\langle n|\, 1 + i\eta(\hat{a} + \hat{a})\,|m\rangle = \tag{3.46}$$

$$= \frac{\Omega}{2}(\delta_{n,m} + i\eta\frac{\sqrt{m+1}}{\sqrt{2}}\delta_{n,m+1} + i\eta\frac{\sqrt{m}}{\sqrt{2}}\delta_{n,m-1}) + O(\eta^2), \tag{3.47}$$

where we can recognize three non-vanishing contribution coming from three distinct processes:
carrier (n=m) characterized by $\omega = \omega_0$,
blue sideband (n=m+1) $\omega = \omega_0 + \omega_T$, or
red sideband (n=m-1) $\omega = \omega_0 - \omega_T$,
if $\eta \ll 1$ sideband contributions are widely suppresed and this is good. As long as the excitation of the atom does not change its localization it means we can look at it without losing it: the centre of mass does not change. For this purpose it would be necessary to have ω_T as big as possible in order to minimize A_T, i.e. the narrowest possible trap. This also means we are not having any undesired Doppler or Recoil effects. We can see the overall Lamb-Dicke regime sidebands evolution in Fig. 3.3 for different values of n. Not always it is possible to perform experiments in this *Lamd-Dicke regime*: only by using very deep optical lettices (as in optical lattice clock or quantum gas microscopes experiments) on can satisfy this condition. But, unfortunatley, this is not our case: we get $\eta \sim 0.5$. This is the reason why we must consider thermal states too.

The term $\hbar\delta\,|e\rangle\,\langle e|$ in the Hamiltonian of Eq. (3.42) also plays an important role by allowing one to energetically target certain motional transitions by detuning the driving laser. In particular, one can create a resonance condition for $|g, m\rangle \rightarrow |e, m + n\rangle$ transitions by choosing $\delta = n\omega_T$.

A crucial element of **Sideband** cooling we have not yet considered is spontaneous decay. Let us now assume that $|e\rangle$ decays to $|g\rangle$ with a rate γ. This can be modeled by the master equation (3.39), reshaped as:

$$\dot{\rho} = \frac{1}{i\hbar}[H_\gamma, \rho] + i\hbar\gamma\int d\Omega D(\theta, \phi)L_{\theta,\phi}\rho L_{\theta,\phi}^\dagger, \tag{3.48}$$

where $H_\gamma = H_A - i\frac{\hbar}{2}\gamma\,|e\rangle\,\langle e|$ is the effective no-hermitian Hamiltonian, the *jump operator* is given by $L_{\theta,\phi} = e^{i|k|\hat{u}_{\theta,\phi}\cdot\vec{r}}\,|g\rangle\,\langle e|$ and $\hat{u}_{\theta,\phi}$ is unit vector along the given direction.

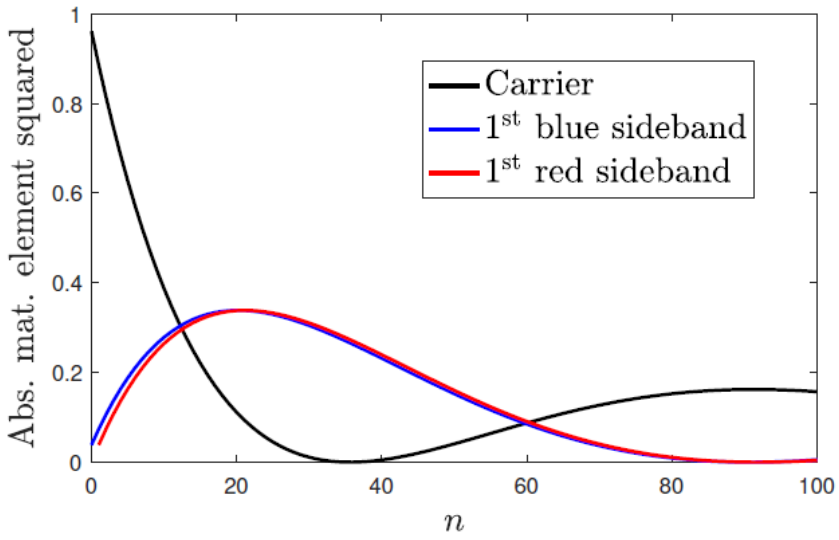

Figure 3.3: Absolute matrix elements squared $\left|\langle m|\, e^{i\eta(\hat{a}^\dagger+\hat{a})}\, |n\rangle\right|^2$ for the carrier ($n \to n$), first blue sideband ($n \to n+1$), and first red sideband ($n \to n-1$), with $\eta = 0.2$. The carrier contribution is dominant until $\eta\sqrt{n} < 1$. Image taken from [**24**].

The jump operators not only de-excite the atom, they also apply a momentum kick in a random (dipole pattern distributed) direction. These random momentum kicks are an intrinsic source of heating and play a role in the temperature limit of sideband cooling.

The final requirements for sideband cooling are certain conditions between ω_T, Ω, γ and η. Firstly, we would like to be able to target a specific $m \to m+n$ transition and to have all others be off-resonant. This requires us to be in the sideband-resolved regime, which means that the separation between motional levels is significantly larger than the power-broadened linewidth of the transition, or $\omega_T \gg \sqrt{2\Omega^2+\gamma^2}$. Secondly, we would like the momentum kick of the spontaneously emitted photon to be small. In particular, we would like the kick to be small enough such that its $m \to m$ matrix element is much larger than all other matrix elements that change the motional state (at least for small m). We can see from Eq.(3.51) and its various approximations in Eqs.(3.52-3.53) that this is achieved when $\eta \ll 1$, i.e. in the Lamb-Dicke regime. Note that the sideband-resolved and Lamb-Dicke regimes can both be satisfied by having a sufficiently large ω_T, but they are not equivalent, and one may be satisfied without the other being satisfied.
We note finally that these two requirements are essentially the major distinctions between sideband cooling and Doppler cooling — in fact, Eq. (3.54) could just as well be used to model light - induced forces in free-space by setting $U = 0$ in the Hamiltonian.

We can now present the full cycle of sideband cooling: an atom in $|g, m\rangle$ is resonantly excited by light detuned at $\delta = -n\omega_T$ to the state $|e, m-n\rangle$, with $n > 0$. We can do this without resonantly exciting other motional transitions as we are in the sideband resolved regime. Eventually, the atom spontaneously emits a photon while in $|e, m-n\rangle$, and since it is in the Lamb-Dicke regime, it decays to $|g, m-n\rangle$ within high probability (again, this is true mainly for small m). The cycle then repeats to $|g, m-2n\rangle$ and so on until a state $|g, m' < n\rangle$ is reached. This is now a

dark states, as there is no longer a state with quantum number $m' - n$, and cooling stops. If we wish to reach the motional ground state, we must ultimately choose $n = 1$ such that the dark state that we reach is $|g, 0\rangle$. Such a cycle is illustrated in Fig. 3.4 below.

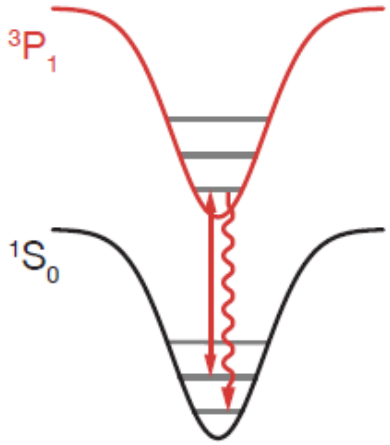

Figure 3.4: Illustration of sideband cooling on the Sr red transition. A coherent transition on the first red sideband drives the atom to a reduced motional state in the electronic excited state. Upon spontaneous decay in the Lamb-Dicke regime ($\eta \ll 1$), this atom returns to the same reduced motional state in the electronic ground state. Image taken from [**24**].

For a 3D trap, performing this process will cool the atom in the direction along which the beam is pointed. However, the spontaneous decay will produce momentum kicks in all three directions, producing an overall heating effect in non-cooled directions [**37**]. In practice, this is mitigated by alternating cooling in all three directions, where pulses are alternated to avoid interference between beams. We have prefered to cool just along one direction by exploiting Sisyphus cooling as weel. An importan observation is that Sisyphus mechanisms are **indipendent of the direction** of the driving beam and affect motional dynamics in all directions - even if the driving beam points along only one of the principal axes of the traps.

The sideband cooling cycle just described is based on the approximation that the motional and electronic ground state $|g, 0\rangle$ is completely dark to excitation as no red sideband exists for this state. However, slow off-resonant excitation of the carrier and of blue sidebands can still occur. Excitation of such transitions can lead to decay that does not preserve the initial ground motional state. This creates a fundamental lower-bound limit on the achievable motional energy (which we will measure by the average vibrational number $\overline{n}$).

[**37**] computes this sideband cooling as $\overline{n} = \frac{5}{16}\gamma^2/\omega_T^2$. This is achieved at $\delta = -\omega_T$ and $\Omega \ll \gamma$, as this configuration minimizes off-resonant excitation. However, this result assumes that the atom is unpolarized and that there is collision-induced thermalization between all three motional degrees of freedom. In our case, both of these assumptions are incorrect as we excite the atom to a well-defined rotational sub-level and there is no collisional thermalization for single atoms.

To compute the true limit in our configuration, we have to take into account the dipole radiation pattern $D(\theta, \phi)$ of spontaneously emitted photons and assume

no thermalization between motional directions. This is already done by Eq. 2.63. We find the steady-state $\overline{n}$ by numerically computing the ρ that satisfies $\partial_t \rho = 0$. Assuming a linear polarization orthogonal to the direction of motion we numerically find that the fundamental limit to $\overline{n}$ under these assumptions is

$$\overline{n} \approx 0.17 \times \gamma^2/\omega_T^2. \tag{3.49}$$

Along the cooling direction the result is quite the same, almost better, nevertheless, as mentioned in the previous section, we note that this cooling happens only along one direction.

We will now examine what happens when the ground and excited state have different trapping potentials. This happens e.g. in Sr on the red transition when the trap is not at a magic condition (Sec. 2.3.4). Two essential effects occur for an optically driven atom in a non-magic trap: (1) a state-dependent potential and (2) a position-dependent detuning, originating from a position-dependent differential light shift. This situation is reminiscent of **Sisyphus** cooling schemes in alkali atoms [**24**], except that in our case we have a detuning gradient instead of a polarization gradient. The situation in our case was recognized as a Sisyphus mechanism and studied theoretically in [**38**, **39**]. Its validity is guaranteed by the typical time scale of photon absorbion $\tau_a = \gamma_a^- 1$, where $\gamma_a = \gamma/2s(\frac{\gamma}{2\delta})^2$: $\tau_a \ll \gamma^- 1$. All we need here to recall is the energetic cooling gap the atom loses any time a Sisyphus effect occours: $E_S = \frac{2}{3} C_G \frac{\Omega^2}{4\delta}$, where $C_G = 1$ is our intercombination transition ($^1S_0 \rightarrow ^3P_1$) Clebsch-Gordan coefficent, since we are using polarized light driven transition, $J = 0 \rightarrow J = 1$.

Therefore, Sisyphus mechanisms can be exploited for cooling in a way similar to sideband cooling, and it can produce cooling in any direction regardless of the orientation of the drive beam. A significant difference, however, is that Sysiphus transitions cannot change the parity of a motional state, so if an atom is *stuck* in an odd parity motional state, a Sisyphus transition cannot bring it to the ground state [**38**].

3.3.3 Heating Processes

So far, we have introduced just how to cool atoms and imaging Photon Recoil heating. Let me introduce other spurious **heating effects**. Fluorescence and other many sources affect the system with different heating rates. The spontaneous emission rate would be simulated later, but its energetic contribution, Photon Recoil Energy E_R, could be discussed now.

Photon Recoil

Every photon absorbed by the atom leads to a kick due to the momentum $\hbar\mathbf{k}_\gamma$ of the photon. If the atom has initially a mean momentum $\mathbf{p}$, the final momentum is $\mathbf{p}+\hbar\mathbf{k}_\gamma$ and the energy changes by $E_R + \hbar\mathbf{k}_\gamma \cdot \mathbf{p}/M$. For an atom in any H.O. eigenstate $|n\rangle$, the mean initial momentum is zero, so the heating rate due to absorbion Λ_{abs}, for imaging and repump beams is one Recoil Energy times the total scattering rate Γ_{tot}:

$$\Lambda_{abs} = \Gamma_{tot} E_R. \tag{3.50}$$

It is, thus, directly proportional to the cooling intensity s_2 and in our case totally negligible. Note that absorption heating is not isotropic and only affects the axis of the repump beam. In the case of insufficient cooling, this leads to the loss of the atoms in this direction, once they reached high H.O. levels. This can be observed in tunneling measurements, where one sees the atoms being pushed out by the repump beam. Also the emitted photons have a recoil which heats the atom with the same strength as an absorbed photon, but isotropically with $E_R/3$ on average per H.O. axis

$$\Lambda_{em} = \Gamma_{tot} E_R/3. \tag{3.51}$$

This contribution came also from repumps beams but very rarely.

Rescattering

An atom can scatter a photon that has been emitted from another atom. If the other atom has been excited resonantly by a decay to state i, the photon is resonant for state i. For the exact results it would be necessary to know the very geometry of the atomic array, anyway the weak optical density and large distance between the atoms allow us to safely neglect this term [**40**].

3.3.4 Quantum Monte Carlo

So far, we have been studing the fluorescence problem only considering γ as a continuous decay contribution. On the other hand, since we are looking for photons number (and possibly its distribution function) - it implies discrete loss of information - we must treat our system as an Open Quantum System, by introducing *Lindblad Master Equation* to describe this *Noisy Evolution*:

$$\dot{\rho} = \frac{1}{i\hbar}[H, \rho] + \sum_j (2L_j \rho L_j^\dagger - \left\{ L_j^\dagger L_j, \rho \right\}), \tag{3.52}$$

where we have added L_j Lindblad Operators - carrying their no-unitary contribution - to *Louiville-Von Neumann Unitary Equation* [**41**].

We must now introduce a couple of approximations, mandatory for the validity of Eq. (3.52):

1) Born's one: system-environment correlations must vanish in the experimental time scale.

2) Markov's one: environment excitations decay quickly due to weak system-environment coupling. "Noise time-independence" implies damping terms.

Being both satisfied by experimental conditions, these two jointed conditions guarantee L_j operators existence and, therefore, Eq.(3.52) validity.

The simplest Lindblad Operator is $L_\gamma = \sqrt{\gamma}\sigma_-$ (Eq. 3.30), which represents the spontaneous emission of photons from a two-level atom excited state $|e\rangle$ to its ground state $|g\rangle$, in such a way we can write the reduced atomic *Master Equation*:

$$\dot{\rho_A} = \frac{1}{i\hbar}[H_A, \rho_A] + \gamma(2\sigma_- \rho_A \sigma_+ - \{\sigma_+ \sigma_-, \rho_A\}). \tag{3.53}$$

If we are interested in fluorescence, it would be useful to underline that $< L_\gamma^\dagger L_\gamma >= tr[\rho L_\gamma^\dagger L_\gamma]$ is the atomic photon counting rate of spontaneous emission.

We can see the whole *Noisy evolution* represented by SuperOperator $\mathcal{L}$ such that $\rho(t) = e^{\mathcal{L}t}\rho(0)$. In such a way, we will be able to find the steady state as $\mathcal{L}\rho^{s.s.} = 0$. Since the spontaneous emission is a stochastic phenomenon, it would be necessary to have a look on *Quantum Monte Carlo* and exploit its idea to simulate the entire process of fluorescence.
We could see the imaging fluorescence process as a "level-closed" system formed by just two main levels ($^1S_0$ and $^1P_1$) and a metastable one $^3P_1$, coupled with $^1S_0$ by the cooling laser. By "level-closed" we mean here that we can consider just these three levels, ignoring possible decays through other states.In this view, it is possibile to reconnect out system to Dehmelt's work and its implemetantions [**41**], where we can see how sometimes the atomic system is available in excited state of fluorescence, passing to ground state, or in and out-of-fluorescence metastable state.

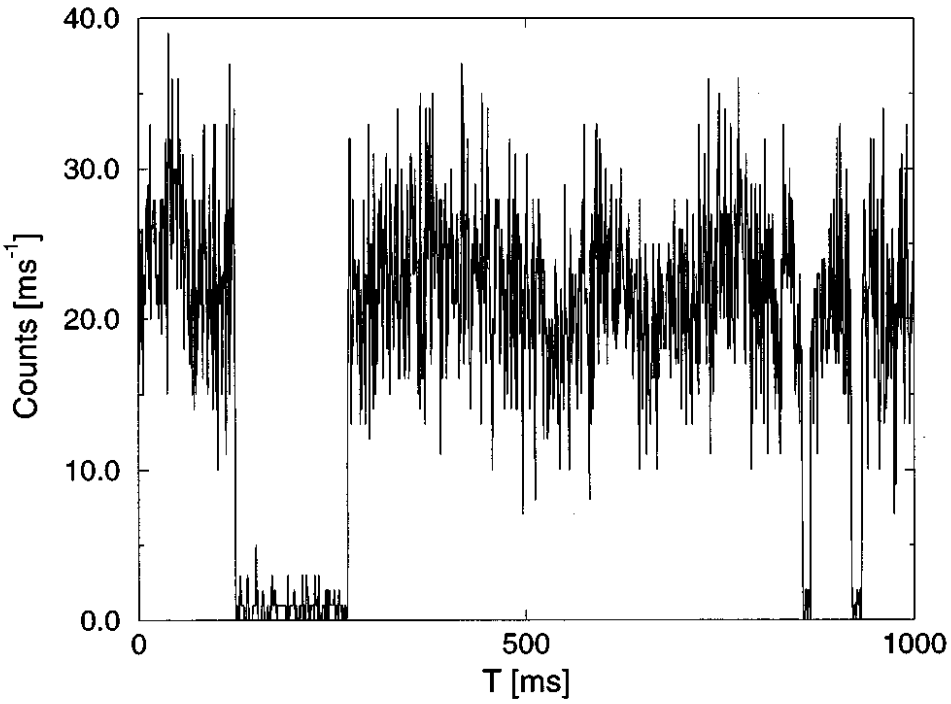

Figure 3.5: When the profile is up, it does fluorescence, when it is down it is locked out of fluorescence, in metastable state(s). Image taken from [**41**].

Anyway, the imaging cycle we are working on allows us to consider the atomic system as just a two-level system, but we still have to consider spontaneous emission in a analog way and to find a proper model to include cooling contributions. Following this idea,
We will consider many trajectories: many different evolutions of the system characterized by different random events - just fluorescence in our case - that project the system in a classical state any time they occur; this means that any trajectory would be statistical equivalent but describing different state evolutions. Since these trajectories are just simulations, we are going to use their average values to predict the mean parameters to optimize the entire imaging process.
Once the optimal parameters are identified, we will collect the resulting photons numbers in an histogram.

Let me now consider the amount of time from the starting "photon-less" state to the first photon emission event, and call it (t_0, t_1). We can now decide to make projective measurements every finite time $\Delta t < \tau$ ($10^{-13} - 10^{-10}$ s); if $\Delta t \ll \omega_0^{-1}, \gamma^{-1}$ we are confining the system to a *Zeno Dynamics*. It has to be clear that, any time-step we pass through without photon emission, we are shrinking the state in a sub-ensamble of the all possible trajectories. Hence, now we have to consider the *Conditional Hamiltonian*, that represents the energetic evolution of the system at time t under the condition that no photon has been emitted between t_0 and t. Under *II Order Perturbative Theory* - guaranteed by Δt, we can write:

$$H_c(t) = H_A(t) - i\hbar\Gamma, \tag{3.54}$$

with $\Gamma = \sum_{i,j,\alpha<(i,j)} \Gamma_{i\alpha,\alpha,j} |i\rangle \langle j|$ *Generalized Damping Term*, where $\Gamma_{i,\alpha,\alpha,i} = A_{i,j}/2$, i.e. Einstein Transition Coefficients. In this conditional space the atomic wavefunction would be represented by:

$$|\psi_A(t)\rangle = \tau_R \cdot exp\left\{-i \int_{t_0}^{t} \frac{H_c(t')}{\hbar} dt'\right\} |\psi_A(t_0)\rangle \tag{3.55}$$

with τ_R "renormalization time". Since, $|\psi_A(t)\rangle = \mathcal{U}_c(t, t_0) |\psi_A(t_0)\rangle$, if we work with ρ representation, we can also write:

$$\rho_A(t) = \mathcal{U}_c(t, t_0)\rho_A(t_0)\mathcal{U}_c^\dagger(t, t_0). \tag{3.56}$$

Since we are interested in photon emission events, we perform a projective measure, such as "zero-photon" projector $P_0 = |0\rangle_F \langle 0|_F \otimes \mathbb{1}_A$, every Δt, the global time evolution will follow this scheme:

$$|\psi_A(t)\rangle = P_0 \left[\mathbb{1}_F \otimes \mathcal{U}_c(t = n\Delta t, (n-1)\Delta t)\right] P_0 \otimes - \otimes P_0 \left[\mathbb{1}_F \otimes \mathcal{U}_c(\Delta t, t_0 = 0)\right] |\psi_A(0)\rangle . \tag{3.57}$$

In order to understand the probability of having no photon emission until $t = n\Delta t$, we need to calculate:

$$Prob_0(t) = tr\left[\rho_A^0(t)\right], \tag{3.58}$$

where $\rho_A^0(t)$ is the reducted atomic state density matrix conditionated by the assumption that no photon has been emitted. This probability will follow an exponential decay according to γ rate. In this trace losing process, we can introduce Reset Operator $\mathcal{R}(\rho) = \sum_{j,i>j,m,l>m} \Gamma_{jilm} + \Gamma_{lmji} |j\rangle \langle i| \rho |l\rangle \langle m|$, such that *Lindblad Master Equation*

$$\dot{\rho} = -\frac{i}{\hbar}[H, \rho] + \mathcal{R}(\rho), \tag{3.59}$$

then it would be enough to solve

$$Prob_1(t + dt, t) = tr\left[\mathcal{R}(\rho(t))dt\right], \tag{3.60}$$

in order to know the probability of having a photon emission in (t, t+dt).

Proceeding with Quantum Trajectories gives us the opportunity to simulate the entire imaging process with a extremely helpful dimensional reduction: the jump operators effect is to replicate the contribution of coherences, off-diagonal density matrix elements; in this way we can now perform any simulation just with N dimension $|\psi\rangle$ instead of $N \times N$ ρ.

3.3.5 Three-Level Atom

Atom cannot be considered as a two-level system any more, but we need to simulate a 3 levels 'V' system since we simultaneously perform imaging excitation and cooling process. Since the Lindblad Master Equation is still feasible in this case, the unpertubed atomic Hamiltonian can be represented in the following way:

$$H = \hbar \begin{pmatrix} \omega_1 & 0 & 0 \\ 0 & 0 & 0 \\ 0 & 0 & -\omega_2 \end{pmatrix} = \hbar(\omega_1 \sigma_1^+ \sigma_1^- - \omega_2 \sigma_2^+ \sigma_2^-) \tag{3.61}$$

where ω_1 is the separation energy between $|1\rangle(^1P_1)$ and $|0\rangle(^1S_0)$ and ω_2 between $|2\rangle(^3P_1)$ and $|0\rangle$. As done before (Eqs. 3.29 and 3.30), we easily identify in $\sigma_i^{+,-}$ creation and destruction operators for $i = 1, 2$ excited states. We therefore neglect spontaneous decay from $|1\rangle$ to $|2\rangle$.

In order to get things simpler, we go straight with RWA approximation: in this way it is possible to describe Interaction Hamiltonian in perturbative regime as

$$H = \hbar(\Omega_1 \sigma_1^x + \Omega_2 \sigma_2^x). \tag{3.62}$$

For notation simplicity, the Rabi frequencies are assumed to be real.

In this formulation (3 levels system Quantum Monte Carlo), we can perform more than 10^2 quantum trajectories in fluorescence quantum jumps, driven by the following optimization parameters: exposure time exT, imaging beam saturation parameter s_1 ($|0\rangle \rightarrow |1\rangle$ transition) and cooling beam saturation parameter s_2 ($|0\rangle \rightarrow |2\rangle$ transition).

Many parameters have been chosen and fixed for different reasons. The first parameter to discuss is beams detuning. For cooling beam (s_2) δ_2 must follow sideband cooling necessities: $\delta_2 = -\omega_2$. For imaging beam it has been enough to fix $\delta_1 = 40$ MHz since it does not affect noticeably the system. We have chosen tweezer generation beam power $P = 20mW$ since $\omega_T \gg \sqrt{2\Omega_2^2 + \gamma_2^2}$: we get $\omega_T = 2\pi \times 107$ kHz. Such a ω_T determines Lamb-Dicke parameter $\eta = 0.45$. This is also a constraint for s_2 as well: $\Omega_2 \ll \omega_T$.

An important constraint for imaging beam (s_1) is that the scattering rate Γ_{s1} (3.39) has to be sufficiently large to guarantee enough emitted photons: since a *prior* Poissonian noise distribution has a 20 photons width (we will see that in the next chapter) it would be smart to identify a $\Gamma_{s1} > 30$ kHz in order to get enough scattered photons inciding on the camera in almost 50 ms of exT with collective efficiency $C_{(1)} = 0.094$ (more than 10^3 emitted photons).

Talking about energies, the tweezer depth (2 mK) has been taken as the cut-off energy to consider the atom loss. Atoms come out of the MOT with a mean temperature of 30 μK. If we consider an heating contribution of $2E_R$, where Recoil Energy is $E_R = \hbar^2 k^2 / 2M \sim h \times 2\pi 70$ kHz, any time an atom get excited and spontaneously emits, such a tweezer admits over 10^3 spontaneous emitted photons. Other heating contributions have to be considered, such that we need a cooling stage to not get atoms lost by heating.

With all spontaneous emission effects and Rabi contributions, we finally can determine an Effective Hamiltonian to run simulations on:

$$H_{eff}/\hbar = (\delta_1 - i\gamma_1)\sigma_1^+\sigma_1^- + (\delta_2 - i\gamma_2)\sigma_2^+\sigma_2^- + H_I. \tag{3.63}$$

We should have treated the whole problem taking termal H.O. Hilbert space $\mathcal{H}_T$, but two main issues has raised: the first one, to address a space with $3 \times N_T$ dimensions (where $N_T \sim 300$) is computationally highly expensive; the second one, physically talking about H.O. energy eigenstates for ${}^1P_0$ is not correct - $|1\rangle$ is almost a non-trapped state and its energetic spectrum is quite continuous, but the spontaneous emission rate guarantees it is still spatially trapped. We proceed reporting a energy variation according to the quantum jump the system does: if it does a fluorescence jump it gets $2E_R$, if it does a cooling jump it loses ω_T for sideband or E_S for Sisysphus.

We now need to re-formulate how cooling events and other heating processes can occur. In a weak Lamb-Dicke regime ($\eta^2 n \ll 1$) the decay sideband cooling rate could be expressed as $\Gamma_2^{sb} = \eta^2 n \gamma_2$, where n is the vibrational level, as done in [**40**]. Practically we will distinguish between Sideband cooling and Sisyphus cooling events by considering any not sideband cooling photon as a possible Sysiphus cooling one: assuming that the atom is always in the right state to get Sisyphus-cooled, only 2/3 of the times it actually get colder. It has been performed a simulation over 250 trajectories collecting the following histogram:

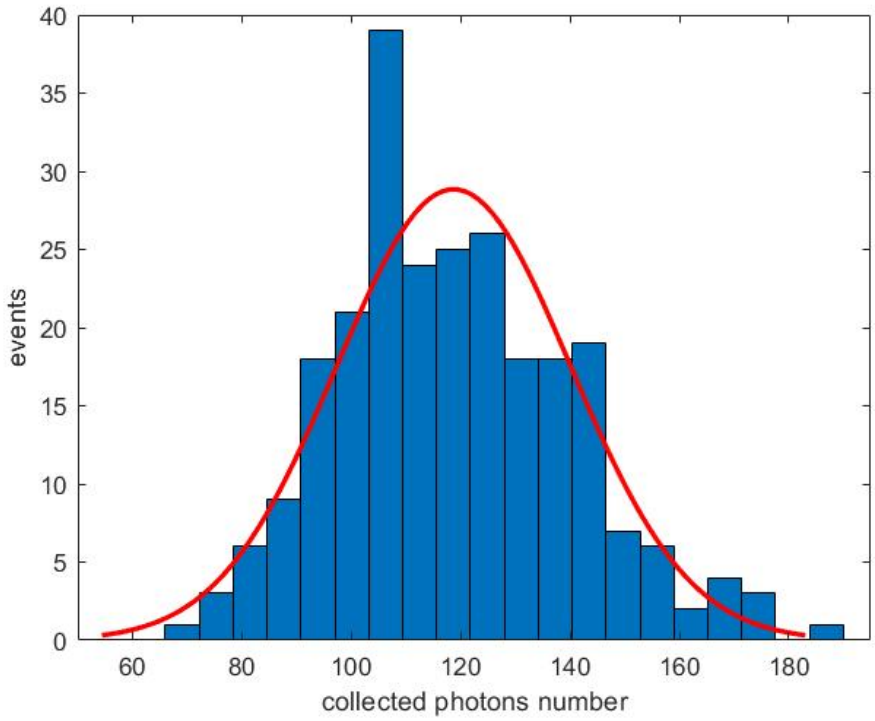

Figure 3.6: Histogram of scattered photons inciding on camera. Optimized parameters: $s1 = 0.0477$, $s2 = 54.67$, $exT = 10$ ms, $\omega_T = 2\pi 107$ kHz. A good fit has been found with Gaussian distribution with $\mu = 118.7$ and $\sigma = 21.4$. No atom got lost.

Let us have a look on how thermal energy changes along 10 different trajectories, in presence or in absence of cooling laser beam, in Figs. 3.7 and 3.8.

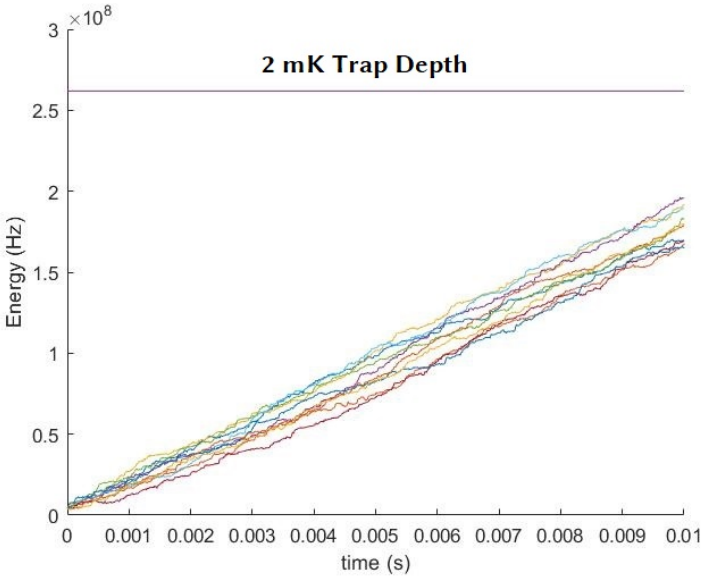

Figure 3.7: 10 different trajectories energetic evolution. Optimized parameters: $s1 = 0.0477$, $s2 = 54.67$, $exT = 10$ ms, $\omega_T = 2\pi 107$ kHz. The horizontal line identify the jump-out energy. No atom got lost.

The optimization has found the best s_1 and s_2 to guarantee $\sim 10^3$ emitted photon in the possible shortest exposure time: 10 ms. With these parameters no one out of 250 atoms has got lost. Sisyphus cooling occurs here more frequently than sideband cooling, but sideband cooling (red sideband transition), which gives stronger contribution (even if only in one direction), preserves atoms from sideband heating (blue sideband transition). For the sake of completeness, we show 10 cooling-less trajectories evolution in the figure below.

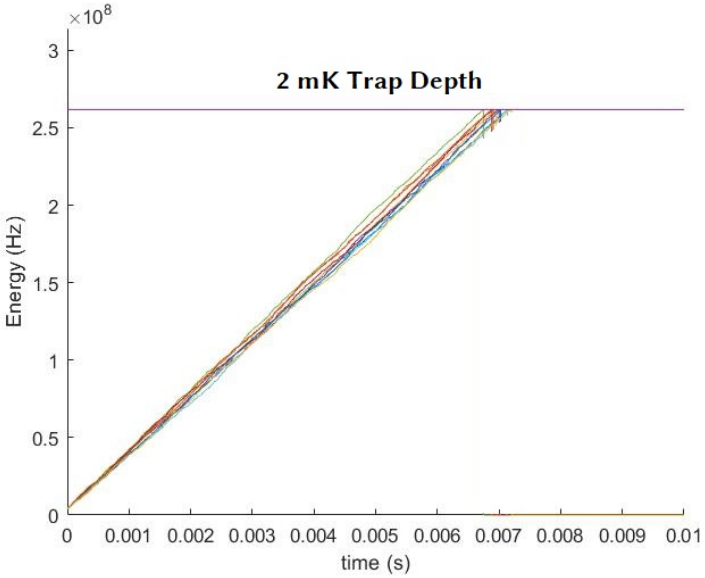

Figure 3.8: 10 different trajectories energetic evolution with parameters: $s1 = 0.0477$, $s2 = 0$, $exT = 10$ ms, $\omega_T = 2\pi 107$ kHz. The horizontal line identify the jump-out energy. All the atoms got lost.

3.4 EMCCD Camera

The photons that are collected through the *imaging* objective are imaged onto the sensor of an electron-multiplying charge-coupled device (EMCCD) camera - we use an Andor iXon Ultra 888. A CCD sensor detects photons by converting them to electrons. The feature that distinguishes an EMCCD from a normal CCD is an electro-multiplying (EM) gain before the readout register, which is important for detecting a small number of photons. The EM gain multiplies each electron into numerous electrons, which functions to overcome intrinsic readout noise in the camera's analog electronics. It is important to understand how this mechanism works and in what situation it is useful. In particular, we will see that the EM gain is only truly beneficial under circumstances of very low background counts, and that it is therefore important to minimize background.

We assume that n electrons are produced on a sensor pixel. In realistic imaging conditions, n is a probability distribution, but to begin with, we will assume it is a fixed number. The EM gain, whose module will be parametrized by a number g, will multiply this number of electrons into a larger number c of signal electrons, which then will be read out via the camera's electronics as count. So c will be given by a distribution which depends on n [**24**]:

$$P_n^{sig}(c) = \frac{c^{n-1}e^{-c/g}}{g^n(n-1)!}\theta(c), \tag{3.64}$$

$$P_0^{sig}(c) = \delta(c). \tag{3.65}$$

This last equation is correct for gain of zero electrons under the assumption that no spurious electrons are produced during the process of multiplication. If such an electron is produced, then it can be multiplied as well, however it may see an effectively smaller gain as it is already partway through the gain register. We will however ignore such effect for now and assume the given formulas are accurate.

These signal electrons are now counted by the camera's analog electronics and digitized to produce counts, which is the ultimate signal reported to the user. The conversion from signal electrons to counts is not without noise, however. Indeed, the number of counts resulting from a certain number of signal electrons is given by a Gaussian distribution parametrized by a standard deviation σ. The distribution of counts as a function of original electrons n is therefore a convolution of a Gaussian distribution between Eqs. (3.64) and (3.65). We will call this distribution $P_n^c(x)$. We point the reader to [**42**] for calibrating g and σ.
We will now calculate the overlap between two count distributions, one produced by n initial electrons and the other by m initial electrons. This will tell us how well we can tell the difference between these two possible signals. We will define such an *Overlap* by the following integral:

$$O(n,m) = 2\int \frac{P_n^c P_m^c}{P_n^c + P_m^c} dc. \tag{3.66}$$

This value is 0 when the two distributions are completley distinguishable, and is 1 when they are identical.

We plot this value in Fig. 3.8 as a function of g/σ for $n \in \{0,1,2\}$. We see that increasing the EM gain has the most significant effect when distinguishing between 0 and 1 initial electrons, whereas for higher values of n, the effect is not

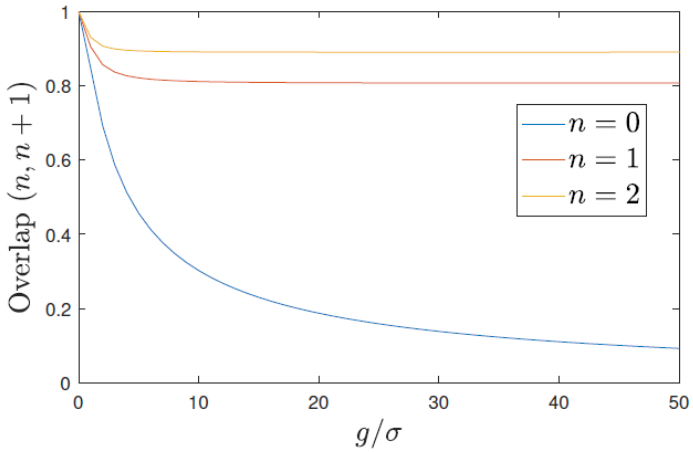

Figure 3.9: Overlap between counts distributions P_n^c and P_{n+1}^c as a function of the EM gain to readout noise ratio g/σ.

as pronounced and furthermore saturates at some value. Intuitively, this can be explained as so: multiplying zero electrons will always (ideally) produce zero signal electrons, whereas multiplying a finite number will always produce some number that scales with g. So there is always a benefit of increasing gain when distinguishing between zero and a finite number, whereas for two finite numbers the benefit is less and eventually vanishes for high enough gain. Thus, to really take advantage of the functionality of an EMCCD, *background light should be minimized as much as possible*. Distinguishing between 0 background photons and 1 atomic photon is much better than distinguishing between, e.g., 10 background photons and 10 background plus 1 atomic photons.

It is not advisable to use EM gain values greater than necessary to overcome the readout noise. A gain of 4 or 5 times the root mean square readout noise is more than sufficient to render this noise source negligible. In practice, this can be achieved with EM Gain of less than $\times 300$ at 10 MHz and $\times 600$ for $30MHz$ operation. Nevertheless pushing gain beyond this value would give little or no extra Signal-to-Noise benefit and would only reduce dynamic range.

Minimizing background becomes even more important when we also realize that the initial electron number n is itself a distribution. There are several stochastic processes that enter this: the number of photons scattered into the objective (either by an atom or by background), the number of photons that pass through the collection optics (characterized by some transmission efficiency), and the number of photons striking the sensor that are actually converted to electrons (characterized by the *quantum efficiency* of camera sensor). All of these distributions are either Poisson distributions or very close, and their convolution - giving n - is also Poissonian. The overlap between two Poissonian distributions of mean λ and $\lambda + m$ is also minimized when λ is small.

There are several contributions to the noise on an image.
• **Photon shot noise** This is the main source of noise on the images and arises directly from the photon quantization. It is strong because we may detect less than 20 photons per pixel of the camera from fluorescence. Its nature is Poissonian.

• **Background noise** There is light that reaches the camera, which was not scattered by our atoms e.g. stray light from the glass cell or background light. We can minimize this contribution to about 1.5 photons per pixel on $50\mu s$ of exposure time. Most of it is static, so we subtract an average background image from each new image before analyzing it. The shot-noise of the background counts remains.

• **Readout noise** The conversion of electronic charge to digital counts has a noise that depends on the readout speed of the camera. The readout noise is the noise of the on-chip amplifier which converts the charge (i.e the electrons) into a change in analogue voltage. It is assumed to be ~ 8 "converted photons" electrons. This contribution could be represented by a Gaussian distribution very well.

For shot noise, the precision of localization scales as $N^{-1/2}$ whereas, for background noise, the precision scales as N^{-1}. Thus, at low light levels, it becomes even more important to minimize the background noise.

Pratically, the way to minimize background is to minimize scattering of imaging beam off surfaces near the imaging objective, to minimize the intensity of the beam by selecting a detuning that is not too large, and to use narrow optical filters in front of the camera. The filters should be *especially* good at rejecting light at the trap wavelength, and also the wavelenghts used for cooling and repumping such as 689 nm, 679 nm , and 707 nm. It is furthermore also important to minimize background originating from dark counts on the camera, caused by things like thermal excitations or so-called "clock-induced charges" CICs [**43**]. These can be minimized by cooling of the sensor to a sufficiently low temperature (a common EMCCD feature is to work $\sim -80^o$ C) and optimizing readout parameters of the camera, such as the readout speed. For our exposure times (~ 10 μs) it is totally neglectable.
In general, background noise can be easily measured and determined performing imaging cycles withuout atomic flux.

Finally we note that some EMCCD cameras are able to be used in a "photon counting" mode which may help with detecting a small number of photons. The global idea is to take advantage of time resolution: instead of taking one image of many photons, a time-series of many low-exposure images is taken such that it is very unlikely that each image is exposed to more than 1 photon. Then each image ideally only records either 0 or 1 charges. If the EM gain is turned up high, then each photon can be detected with very high fidelity. This is called "fast kinetics" technique.
It allows to take multiple images within 100 μs from each other by using a masked part of the sensor as temporary storage for the sequence of images. The masking is done by inserting a narrow horizontal slit with a height of 200 μm in the intermediate focal plane of the imaging system and stray illumination is eliminated by carefully covering the imaging system. After each exposure, the acquired image is moved into the masked area of the CCD and the shift time sets the maximum acquisition rate. This could not be useful for us since all these repeated multiple images bring an

intractable Noise contribution during an average exposure time $\sim$ 10 ms without offering actual advantages. Becauase of these last considerations, we decided to not perform the "fast kinetics" mode but to use 1 Mhz camera rate.

3.4.1 Efficiency

It is important to note that the detection efficiency includes both the transmission efficiency of the optical detection system and the CCD camera quantum efficiency. Quantum efficiency (QE) is the measure of the effectiveness of an imaging device to convert incident photons into electrons. For example, if a sensor had a QE of 100% and was exposed to 100 photons, it would produce 100 electrons of signal.
The efficiency of the CCD could be measured by performing a conventional calibration of the losses in the optical channel through a transmissivity measurement, let us say it is 90%.
We have to consider that in the photon counting regime, the detection efficiency is a function of the threshold. Therefore, it is not possible to perform a direct comparison between the efficiencies for the two regimes. However, it is possible to calculate the dependence $QE(x_t)$ by the measured value of the analog quantum efficiency $QE(0)$ and to compare this with the measured efficiency in photon counting. The quantum efficiency measurements is the most significant limit of this section and takes advantage of the unique versatility in terms of the regimes of operation of our detector, as guaranteed by the constructor (Fig. 3.9).
In order to understand the theoretical behavior for the noise and for the quantum efficiency QE of our camera, we can analyze the typical model of an EMCCD. The most relevant noise contributions typically affecting an EMCCD are readout noise, dark current, and spurious charges. The dark current is due to thermally generated charges and it strongly depends on temperature and acquisition time. Generally, it can be independently measured and subtracted from data. In our case, the camera parameters can be set to have a neglectable contribution of dark current. At our working wavelenght, we can assume $QE \sim 85\%$. Therefore the total efficiency would result $E = 80\%$.

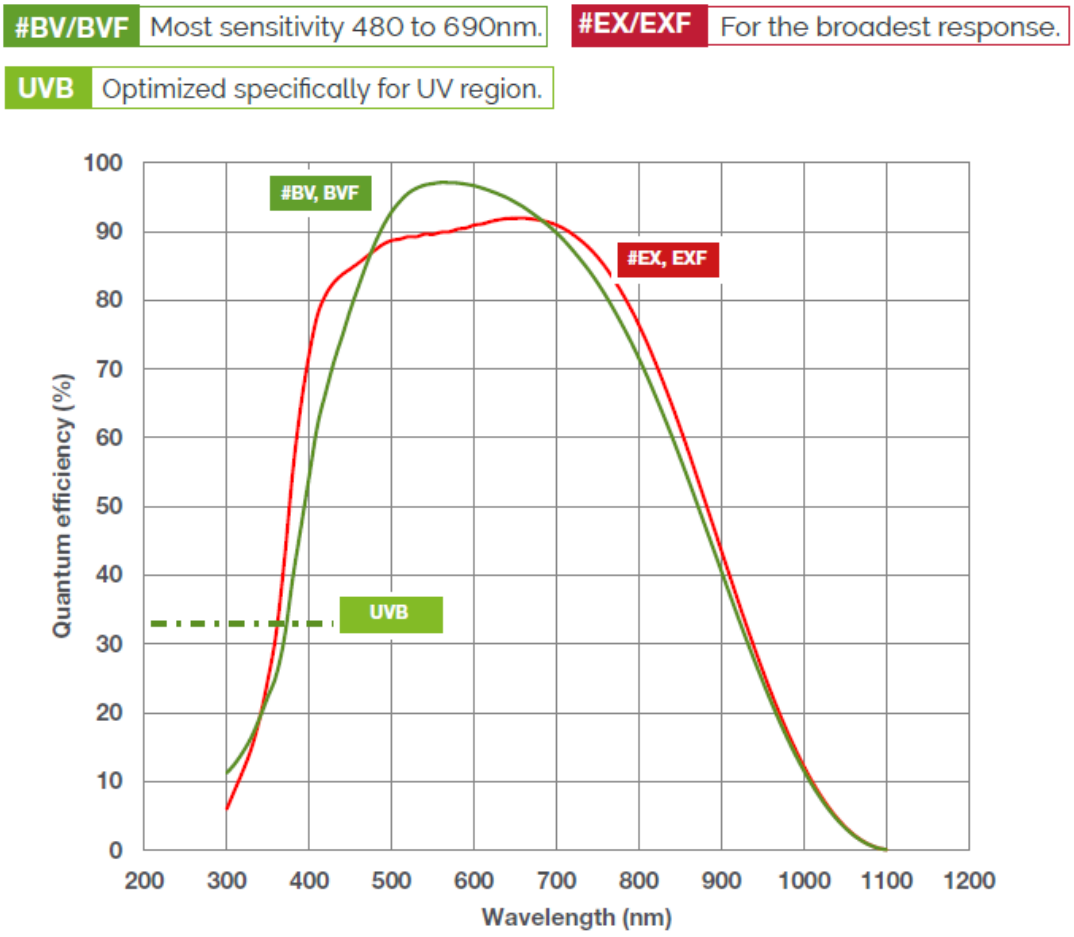

Figure 3.10: Andor iXon Ultra 888 certified Quantum Efficiency at differents wavelenghts.

3.5 Camera Analysis

In order to reveal the distribution of loaded atoms in optical tweezer array, we use the "fluorescence" imaging technique. The main experimental data we read is an histogram of detected photons from a single representative tweezer. Since our algorithm needs to know the exact number of loaded atoms and exactly the traps where they have been loaded in, it is necessary to take a look on the loaded system with the highest possible reliability in the shortest time. To do so, two points are stressed out: it is necessary to distinguish exactly the presence from the absence of any atom in any trap, as it is necessary not to disturb those atoms in such a way they get hot and jump out of those traps. In other words, the optimal imaging setup is the one that uses enough imaging power to get all the photons - scattered by atom in fluorescence - needed to distinguish the presence of that atom, but not enough power to make that atom jump out of its trap [**44**].

We are now looking to quantify two things: (1) what is the probability that we are correct about the presence or absence of n atom and (2) what is the probability that the atom will remain trapped after imaging. We call item (1) *Fidelity* of imaging and item (2) *Survival* probability.

3.5.1 Fidelity

After each image, we systematically classify the image as either "atom detected" or "atom not detected". We define the *imaging fidelity* F as the probability of this classification being true: it is the probability that we either decide that an atom is detected when one was present at the beginning of the imaging process, or that we decide that an atom is not detected when one was not present at the start of the image. This may also be termed "accuracy" of our binary classification. Note that it is important to specify that this definition applies to the start of the imaging procedure, as atoms may be lost during exposure time.

In order to determine F, we need to identify a model-dependent process by making some assumptions: our prior knowledge about the probability of an atom being present is important for determining F. If we had prior knowledge that, e.g., a trap contained an atom with probability 1, then we could have unity fidelity by just deciding "atom detected" every time, regardless of what an image says or whether an image has been taken at all. Our actual prior knowledge is that a trap contains an atom with probability $p = 0.5$. Note that this means that the possible lowest "reasonable" (without intentionally trying to be wrong) imaging fidelity is 0.5: you can simply guess the result and be correct half the times.

We know that the signal histogram is the sum of a component coming from the absence of an atom and a component coming from the presence of an atom. If we have a model for the functional form of these contributions, we can compute the imaging fidelity F by integrating the areas of both contributions that are on the "correct" side of the chosen classification threshold. In particular if $P_{atom}(x)$ is the model function for the histogram distribution of an atomic signal and $P_{bg}(x)$ is that of an atomless backround (with both distributions separately normalized in areas to

1), where x is the number of detected photons, then the imaging fidelity is

$$F = (1-p)\int_{-\infty}^{x_t} P_{bg}(x)dx + p\int_{x_t}^{+\infty} P_{atom}(x)dx \tag{3.67}$$

or more sinthetically:

$$F = (1-p)F_0 + pF_1 \tag{3.68}$$

and, in our case (p=1/2),

$$F = \frac{1}{2}(F_0 + F_1) \tag{3.69}$$

where x_t is the classification threshold, i.e., the minimum number of photons to "call" an atom presence [**24**].

The remaining problem is now to figure out the proper function forms for the two probability distributions and to fit them to the measured histogram. For reasonably good imaging, the histogram often looks like two well defined peaks - one for background and one for an atom. Often, Gaussians are used to model these peaks. However, a more accurate model (especially important when imaging a small amount of photons) should include a skew that arises from the camera gain as well as the Poissonian nature of photon scattering and detection.

One possible model is a Gaussian convolved with Poisson distribution of the n parameter of these distributions. Such a model takes into account camera readout noise, camera gain, and Poissonian scattering/detection.

Under certain circumstances, it might be necessary to add another contribution to $P_{atom}(x)$. In particular, we find that when imaging at a trap wavelength of 515.2 nm, every photon scattered by the atom entails a small probability of the atom being immediately lost. To account for this effect in the imaging fidelity, we must add an exponential distribution to $P_{atom}(x)$. This exponential distribution has a maximum at the signal value corresponding to one scattered photon (counter-intuitively, it is most likely that an atom is lost at the very first scatter) and decreases exponentially until it reaches the atom signal peak corresponding to atoms that were not lost. In principle, if imaging proceeds for an enough long time, all atoms are lost and the entire atom signal histogram looks entirely exponential (with some convolution of readout/detection distributions). Other loss mechanisms, such as those caused by heating, are generally not exponential but can also contribute to some kind of smearing of the atom signal histogram [**24**].

Once a correct model is found and the histogram are properly fit, there should exist a unique choice of classification threshold x_t, that maximizes the fidelity F.

It is possible to adjust x_t such as to favour one or the other of these. For example, if one wants to avoid false positives as much as possible but does not care about potentially "missing" some atoms (false negative), the x_t can be increased beyond its optimal value for F.

3.5.2 Survival

Imaging fidelity is not everything: we still really care about the atom still being there trapped after imaging. Indeed, we also need to optimize the imaging process for *Survival* S: the probability that an atom which was present at the start of the imaging process is still there after the end of the imaging process.

If we had an imaging scheme that had perfect fidelity ($F = 1$), this would be easily to be measured: one just takes two consecutive images and computes the probability that an atom is detected in the second image too. We will call the result of such a measurement S_0. If $F = 1$, $S_0 = S$. In realistic cases ($F < 1$), we need to correct S_0 for imaging errors before being interpreted as the true survival.

S_0 is given by the probability of positive detection in both images divided by the probability of positive detection in the first image. Under the assumption of a filling chance of p=0.5, this is given by:

$$S_0 = \frac{F_1^2 S + F_1(1-F_0)(1-S) + (1-F_0)^2}{F_1 + (1-F_0)}. \tag{3.70}$$

Inverting for S, we get

$$S = \frac{(F_1 + 1 - F_0)(S_0 + F_1 + F_0 - 1)}{F_1(F_0 + F_1 - 1)}. \tag{3.71}$$

This calculation assumes both images having the same fidelities, but a similar calculation is possible even if that is not the case [**24**].

Finally, we note that survival itself may enter into the calculation of F_1, as an atom may be lost during imaging *before* it scatters enough photons to be positively detected, which reduces F_1. Such a situation requires an indipendent model for the loss.

We understood how to compute F (by fitting the histogram) and how it affects S. However, this approch can be highly dependent on the functional form of the histogram in its low probability wings. For all these reasons, it has been useful to simulate the entire imaging process, obtaining a *priori* S: on 250 simulations the atom never got lost, this could signify that statistically $S > 99,8\%$.

3.5.3 Camera Results

Although an atom is essentially a "point-source" because its characteristic size is much smaller than the wavelength that it emits, its fluorescence image will have some intrinsic spread with a functional form sometimes called the *point-spread function* or PSF. This size of the PSF is important as it gives a length scale beyond which two atoms can be easily distinguished. This is one of the various limits on how tightly spaced an atom array can be, though practically there are usually other limits that become important at long scales.

The physics of the PSF is practically identical to diffraction of light through a finite aperture. Indeed the same procedure can be applied simply by propagating in reverse the fluorescence light which scatters into the solid angle collected by the imaging objective. Approximating the dipole radiation pattern to be isotropic with no polarization gradients, the result is an Airy disk, such that the characteristic size of the ideal PSF scales as $f/kR \sim \lambda/NA$. If we take a look on the first Airy circle

we are going to see only 84% of total fluorescence intensity, i.e. 84% of photons arriving on the camera within that spot. We see from this result that imaging with shorter wavelengths beneficially allows for a smaller PSF. This results assumes ideal "diffraction-limited" imaging conditions [**45**]. In practice, a few things may degrade the PSF, such as defocus, optical aberrations, thermal spread of the PSF atomic motion and pixelation on the camera sensor.

In our apparatus, we can use a $\times 8$ magnification lens M_L, in such a way the atom image spread on the camera would be $spr = 2.44 M_L \lambda_1 NA = 4.5$ μm. In terms of pixel it corresponds to a matrix 3x3. It would be interesting to understand if such a magnification is the optimal for Fidelity F. We can now consider that we know almost exactly where the atom is supposed to be trapped. Atom's relative motion could be evaluated as done before as $\Delta x = \hbar k \Gamma_s / m \omega_T^2 \sim 13$ nm and then neglected. We could even evaluate a Noise contribution due to the sum of a nxn pixel matrix, which the atom imaging is supposted to be in.

Considering a separated contribution of Background Noise (10 μs), Shot Noise and Readout Noise, we can simulate the total Noise contribution on a 3x3, 4x4, 5x5 or 6x6 pixel matrix then compare them with Signal distribution, in order to identify the best Fidelity of our process. Under such assumptions we can simulate 10^3 imaging events on a $n \times n$ pixels matrix, whose total photo-count sum is represented by:

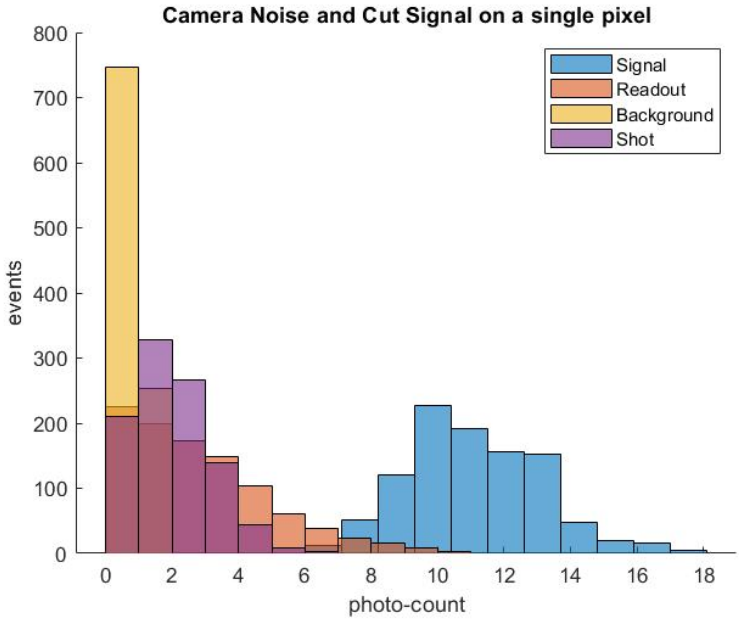

Figure 3.11: Noise and inciding photons on camera distribution, at the same optimized parameters as found before [$s1 = 0.0477$, $s2 = 54.67$, $exT = 10$ ms] in a $\omega_T = 2\pi 107$ kHz tweezer. Here we see a slight overlap between Signal and Noise pdf. In particular Signal-to-Noise Ratio is less than 10. The Readout Noise is here the biggest obstacle to threshold.

It is necessary to understand that considering just one pixel distribution would be difficult to analyze, mainly for thresholding, but secondly for the intrinsic loss of information. The first reason is easily to underline: the best cut-off parameter would be $x_{th} = 7.5$ that guarantees $F = 98\%$. The second point means that basing the entire analysis on a single pixel (maybe the brightest one) would lead to exclude all the other "fluorescence" pixel without any particular reason: this cause a SNR

bigger than usual. We could perform some particular PCA techniques or mainly simple mask filters, but it would be not totally useful and therefore not necessary. Changing M_L would help us in focusing the main Airy circle in just one pixel in order to overcome these problems, but a bigger one would rise: if e.g. $M_L = 2\ spr \sim 1.5\mu m$ (dimension of the pixel), this would mean that two atoms $5\mu m$ far from each other will be imaged 2 pixels apart; such a thing would be totally undesirable if the two atoms not center the pixels perfectly. Similar consideration could be made for a 2x2 pixels matrix. Since we started considering a 3x3 pixels PSF, we now analyze that configuration.

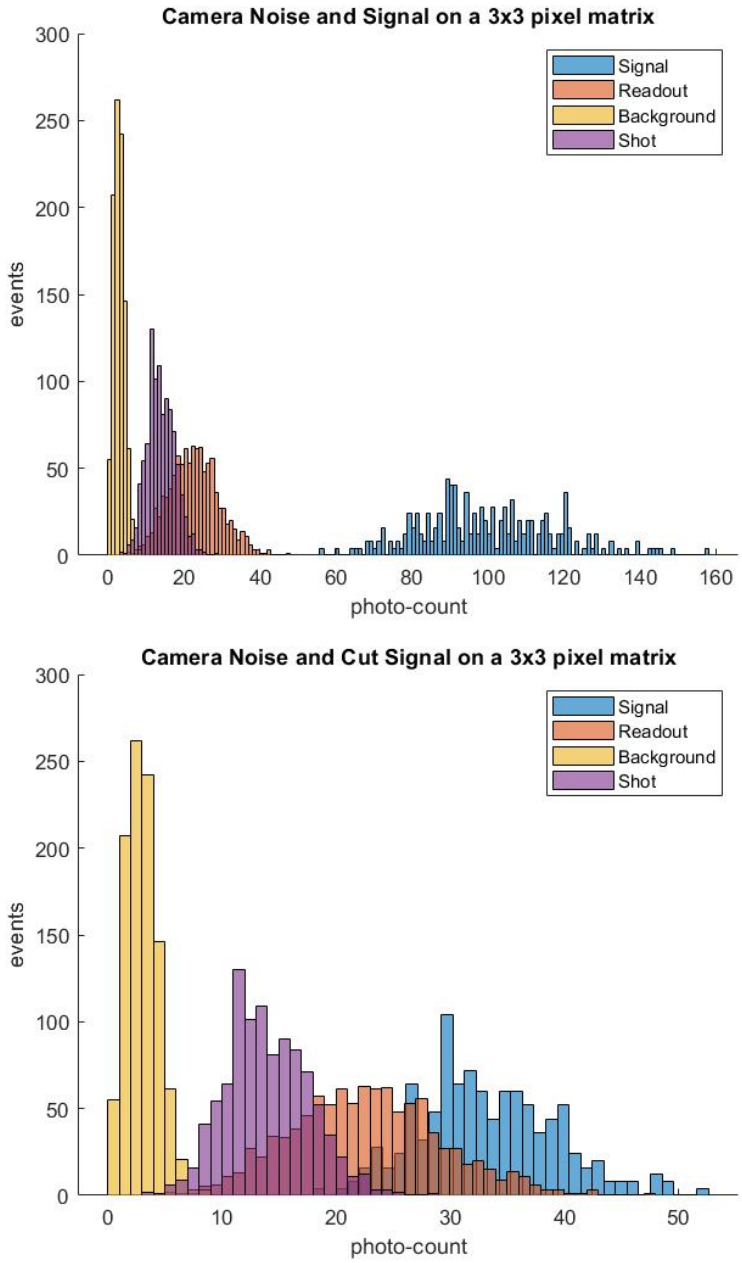

Figure 3.12: Noise and inciding photons on camera distribution, at the same optimized parameters as found before [$s1 = 0.0477$, $s2 = 54.67$, $exT = 10$ ms] in a $\omega_T = 2\pi 107$ kHz tweezer. In the upper image we see two well distingished distributions Signal and Noise pdf. The lower image shows how not centering the Airy disk on the pixel matrix may lead to an undesired overlap.

From these two images it should be clear that the less pixel we consider the less noise would raise. Nevertheless, if we study a 3x3 pixels PSF on a 3x3 pixel matrix we may get a loss on information due to not-centered image. The next step will lead us to consider then a 4x4 pixels matrix.

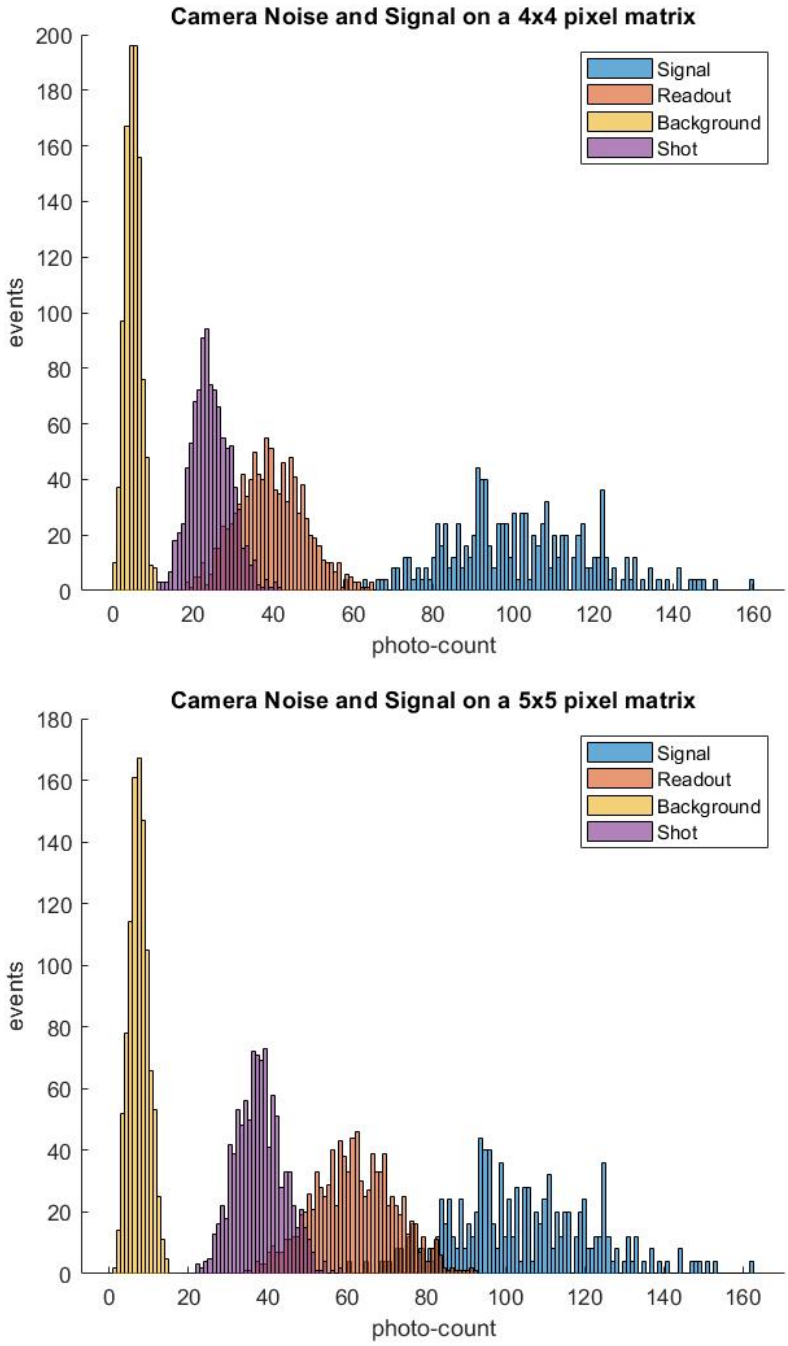

Figure 3.13: Noise and inciding photons on camera distribution, at the same optimized parameters as found before [$s1 = 0.0477$, $s2 = 54.67$, $exT = 10$ ms] in a $\omega_T = 2\pi 107$ kHz tweezer. In the first image we see two well distingished distributions Signal and Noise pdf.

Once again it is helpful to evaluate the Fidelity function. For the 4x4 we identify $x_{th} = 62$ to get $F = 99.3\%$. For the 5x5 we identify $x_{th} = 76$ to get $F = 92.5\%$.

The next point will be to study the EM amplified signal histogram. As said before a $g = 5 \times \sigma$ will be enough. With such a gain value, we obtain the following results:

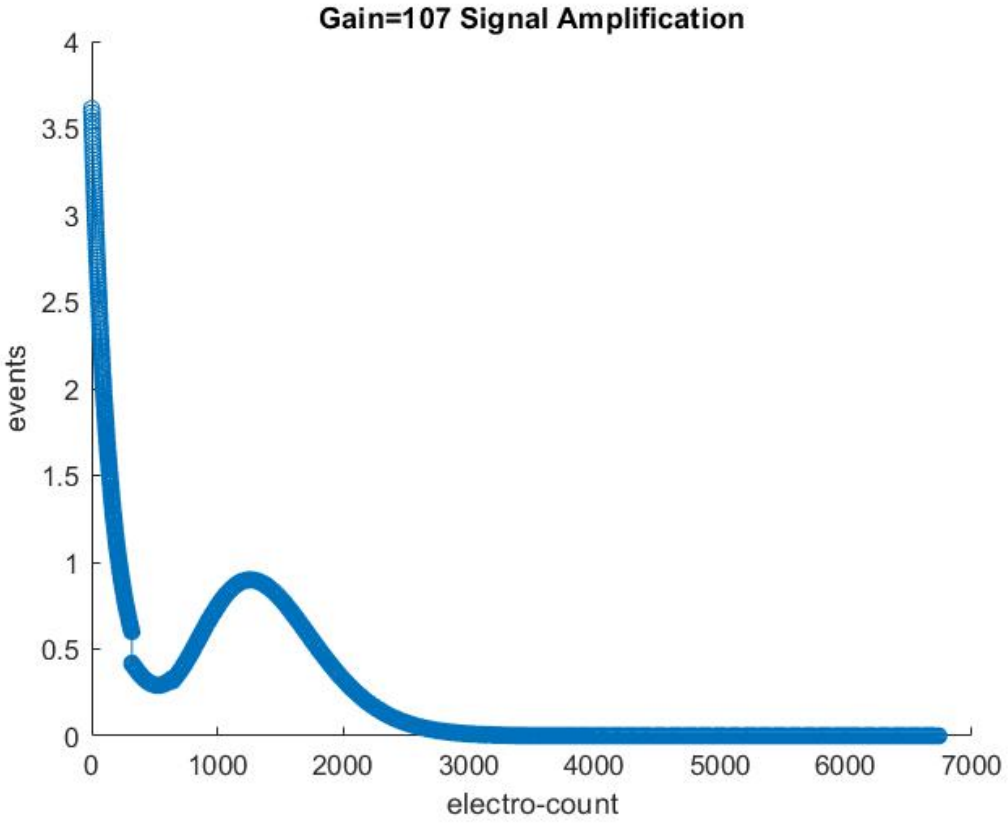

Figure 3.14: Amplified Camera Signal and Noise distribution for single pixel. We can easily identify the signal peak where $SNR \sim 10^2$. Around the value of 300 we can see a discontinuity that represents the separation between Noise and Signal gain-amplified distributions.

As guaranteed by the manufactures of the camera the $SNR \gg 10^2$ and the Readout Noise is negligible. In this case for a more further evaluation of F it would be necessary to measure it empirically.

With all these considerations and reliability, we proceed in our task. The next step will be to understand how to move those *imaged* atoms across the experiment plane in the shortest time.

Chapter 4

Loading and Reordering Processes

A key feature of optical tweezer platforms is the ability to isolate only one atom per tweezer. Not having to worry about short-range collisional or molecular interactions or hopping from site to site makes the relevant physics relatively "clear". Furthermore, having one atom per site makes the treatment of tweezer arrays as qubit registers natural. First, we will describe the loading of multiple atoms from a Sr red MOT into tweezers. Then, we will describe a technique for inducing pairwise loss such that tweezers end up loaded with either one or zero atoms. From here, defect-free arrays can be assembled via re-ordering. We will conclude with some potential techniques for beating the standard 50% filling fraction limit of pairwise loss and comparison with new state-of-art quasi-deterministic loading techniques.

4.1 Loading single atoms through Pairwise Loss

We load atoms into tweezers from the "red" MOT of Sr, which is usually generated as a second-stage MOT after a larger, hotter, and less dense "blue" MOT. The techniques for generating these MOTs are well established. The number of atoms trapped in a single tweezer could be calculated by estimating the number of atoms in the MOT occupying the trapping volume of a single tweezer, assuming they will be captured when the tweezer is instantaneously turned on. While in principle any atom with motional energy smaller than the tweezer depth will be trapped, it is sensible to require a more stringent condition for trapping that will allow us to consider only deeply trapped atoms localized close to the center of the tweezer.

Our ultimate goal is to prepare one atom per tweezer. One strategy for this might be to fine-tune the density of the red MOT or some other loading parameter such as to maximize the probability of loading only one atom. While this is possible, weakly-interacting atoms fill traps stochastically, usually following a Poisson distribution. The maximum possible probability of loading a single atom under Poissonian statistics is only about 37%(occurring at a mean atom number of $N = 1$). For the rest of the tweezers, 37% would be empty and 26% would be loaded with multiple atoms. A more robust way of preparing single atoms is to initially fill tweezers with many atoms and from there eliminate excess atoms. An ideal mechanism would expel atoms one-by-one, and stop as soon as only one atom is left. While such schemes have been realized to some extent in alkali atoms and will be discussed for Sr, they involve a high degree of fine-tuning.

A mechanism which instead is most ubiquitously found in single-atom physics is pairwise loss. Pairwise loss is the simultaneous loss of pairs of atoms, such that $N \rightarrow (N-2)$. One can therefore see that the ultimate result of pairwise loss is $N_f = N_i \mathrm{mod} 2$, where the subscripts stand for "final" and "initial". In other words, odd initial atom numbers end up at one, and even initial atom numbers end up at zero. This is why the end result of pairwise loss is also sometimes called "parity projection".

The average number of atoms remaining at the end of pairwise loss is therefore $N_f = p_i^{odd}$, where p_i^{odd} is the probability of initially having an odd number of atoms. Assuming N_i follows Poissonian statistics, this becomes

$$\overline{N}_f = \frac{1}{2}(1 - e^{-2\overline{N}_i}) \tag{4.1}$$

This tends to 1/2 for increasing values of $\overline{N}_i$, and already for $\overline{N}_i = 4$ there is only 1.7×10^{-4} difference from $\overline{N}_f = 1/2$. By inverting this equation, one can also estimate $\overline{N}_i$ (realistically, for values of $\overline{N}_f$ close to 0.5, this would give a lower bound limited by the statistical error of the measurement).

In the context of a tweezer array, pairwise loss in the large $\overline{N}_i$ regime means each trap will have a probability of 1/2 of ending up with a single atom or otherwise being empty. If we then ask how many total single-atom filled tweezers we expect to have in an array of N_{traps} traps, the answer will be a binomial distribution with a mean of $N_{traps}/2$. This distribution has a standard deviation of $\sqrt{N_{traps}}/2$. The mechanism for pairwise loss in neutral atoms is usually excitation to two-atom molecular states [**46**].

The specifics and subtleties of this process vary between atoms and transitions, but an overall theme is that a pair of atoms in an electronically excited molecular state gain a large amount of kinetic energy upon decay to the electronic ground state (formed by photoassociation processes induced by the cooling light in the presence of a tight confinement) — enough kinetic energy such that both atoms exit the trap.

4.2 Priority Algorithm

In order to minimize the experimental time, we devised an algorithm which analyzes the reordering problem before atoms get loaded. In such a way, we spend most of the computational time before the reordering phase. The algorithm will note which traps have priority to be filled before which others. That priority is going to be represented by a list (called "priority") of traps sorted by importance. We initialize a graph formed by our atomic traps as graph nodes. Graph geometry would be defined by atomic traps positions on a (x, y) plane.

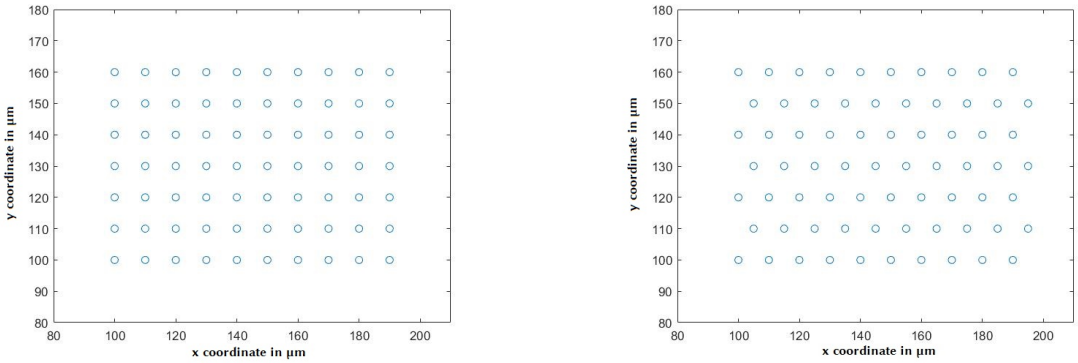

Figure 4.1: Two atomic traps arrays with compact geometry: Rectangular and Triangular. 70 traps.

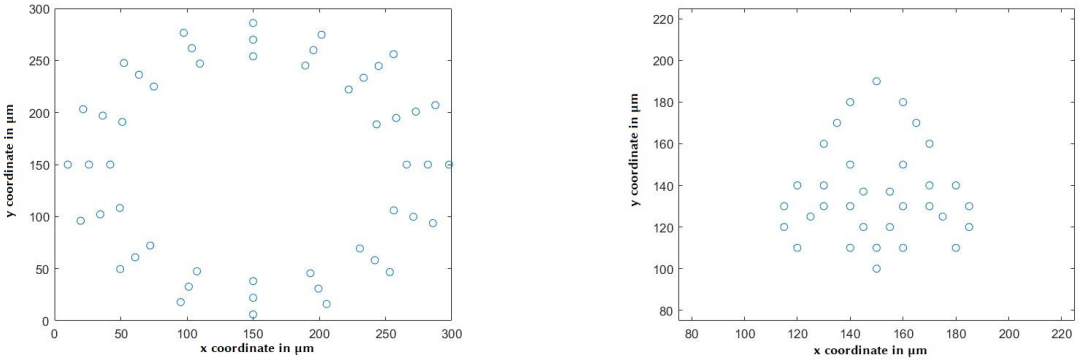

Figure 4.2: Two atomic traps arrays with arbitrary geometry: a Crown/Spiral and a Lily. 50 and 33 traps.

4.2.1 Reserve Traps

Since we can load atoms in SLM traps with a rough probability of 0.5, we need at least $2N$ traps to load N atoms. It is not guaranteed that we get a sufficiently loaded array: sometimes more than N atoms are loaded, sometimes less. In order to have a sufficiently loaded system (more than N loaded atoms) most of the times (more than 99%) we must create at least $2N+2\sqrt{3N}$ traps (or its rounded number). Let us suppose to have M total traps and let N be the minimum acceptable number of atom loaded in those traps (not more than one atom each trap). If any single trap has p probability to catch an atom, the total probability of having more than

N atoms in those M traps is:

$$P = \sum_{n=N}^{M} \binom{M}{n} ((1-p)^{M-n} p^n) \tag{4.2}$$

If $p = 0.5$, and $P > 0.99$ we need to find M such that:

$$\sum_{n=N}^{M} \binom{M}{n} \frac{1}{2^M} > 0.99 \tag{4.3}$$

if we remeber "Newton's Binominal Rule" $(a+b)^M = \sum_{n=0}^{M} \binom{M}{n} a^{M-n} b^n$ we conclude that the prevoius constraint is equal to:

$$\sum_{n=0}^{N-1} \binom{M}{n} \frac{1}{2^M} < 0.01. \tag{4.4}$$

The first and most trivial case is $N = 1$: $1/2^M < 0.01$: we have found the minimum value of $M = 7$. The case $N = 1$ does not accept any kind of reordering problem. The naturally second and more interesting case is $N = 2$: $(M + 1)/2^M < 0.01$. In this case $M > 11$. This "attempt" procedure is not practicle for high values of N.
For higher values of N, we are able to approximate the binomial distribution to a Gaussian one, with *centroid* $= M/2$ and $\sigma = \sqrt{M}/2$; as we can see in Appendix C if we want to include 99% of events in our distribution we need to take N as cut off value at least 2.4 times standard deviation minor than *centroid*; we then get the expression

$$N = M/2 - 1.2\sqrt{M}, \tag{4.5}$$

that can be easly inverted as

$$M = 2[1.2^2 + N \pm \sqrt{1.2^4 + 3N}]. \tag{4.6}$$

If we suppose to take high values of N ($N > 18$), it is allowed to approximate it as:

$$M = 2N + 2\sqrt{3N}. \tag{4.7}$$

Where the positive contribution of the square root is taken to be as sure as possible about the loading percentage.
Eventually, we are having N final traps (where atoms are supposed to move to) and $N + 2\sqrt{3N}$ reserve traps. Since we are looking for an array with just those N atoms in the right position, we may have to drop all those extra atoms still in some other traps; it will cost as a regular tweezer movement, but the average time summing all those dropping movements is quite inferior than the time needed to re-load the system in case of unsufficently loaded atoms. That is the reason why we are proceeding with all those extra traps.
We need now to figure out what kind of algorithm we need, in order to create reserve traps. Since the less we move atoms the best we do, it would be smart to create reserve traps as close to final traps as possible: it does not make any sense to put reserve traps right next to final traps within a distance of 10 μm, because too close atoms will interact in such a way we could lose them. In this view, we need to find, close to each final trap, the closest free spot where to put their reserve traps. We can

create one reserve trap for each final trap and then we would need $2\sqrt{3N}$ more: we can just reiterate the process again around the graph center until the right number of traps is reached.
On the other hand, if we need a final array with a certain geometry, it is possible to create reserve traps following that geometry, but this is not implying notable advantages in problem complexity or efficiency.

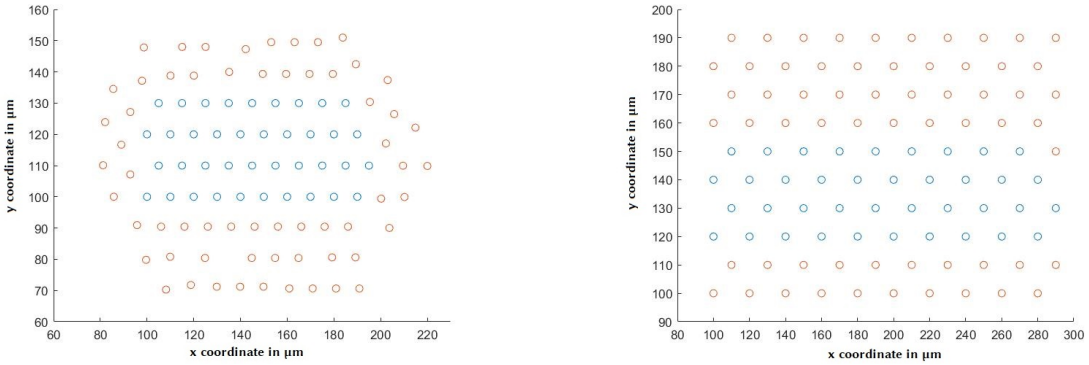

Figure 4.3: 39 final traps (blue) with their 61 reserve traps (red). In free-searching way on the left, in geometry-following way on the right.

4.2.2 Creating Paths

Graph edges have to be lined up to identify which path make atoms move through. They can be easily created by triangulation (quite common function of any programming platform), but it might be not enough. Since our algorithm tries to solve reconfiguration in any geometrical kind of array, it is necessary to check whether any edge gets too close to any other trap. If that happens, an experimental issue occurs: if we move an atom too close to an already trapped atom, they might interact, causing their probable loss. Hence, we perform a "cleaning" check on any graph edge, removing any of them passing too close to any trap. As that is the only actual constraint in creating edges - one can talk about triangulation topological advantages, but it does not really matter - we can easily draw a fully connected graph and then "clean" it up from those undesired edges.
Since our array dimension is around 300 μm and atomic tweezer need "turning on" time of 5 μs and around 10 μs each 1 μm of movement, in atomic moving we can consider any passed edge as a step, and this would tell us what average time any movement will cost.

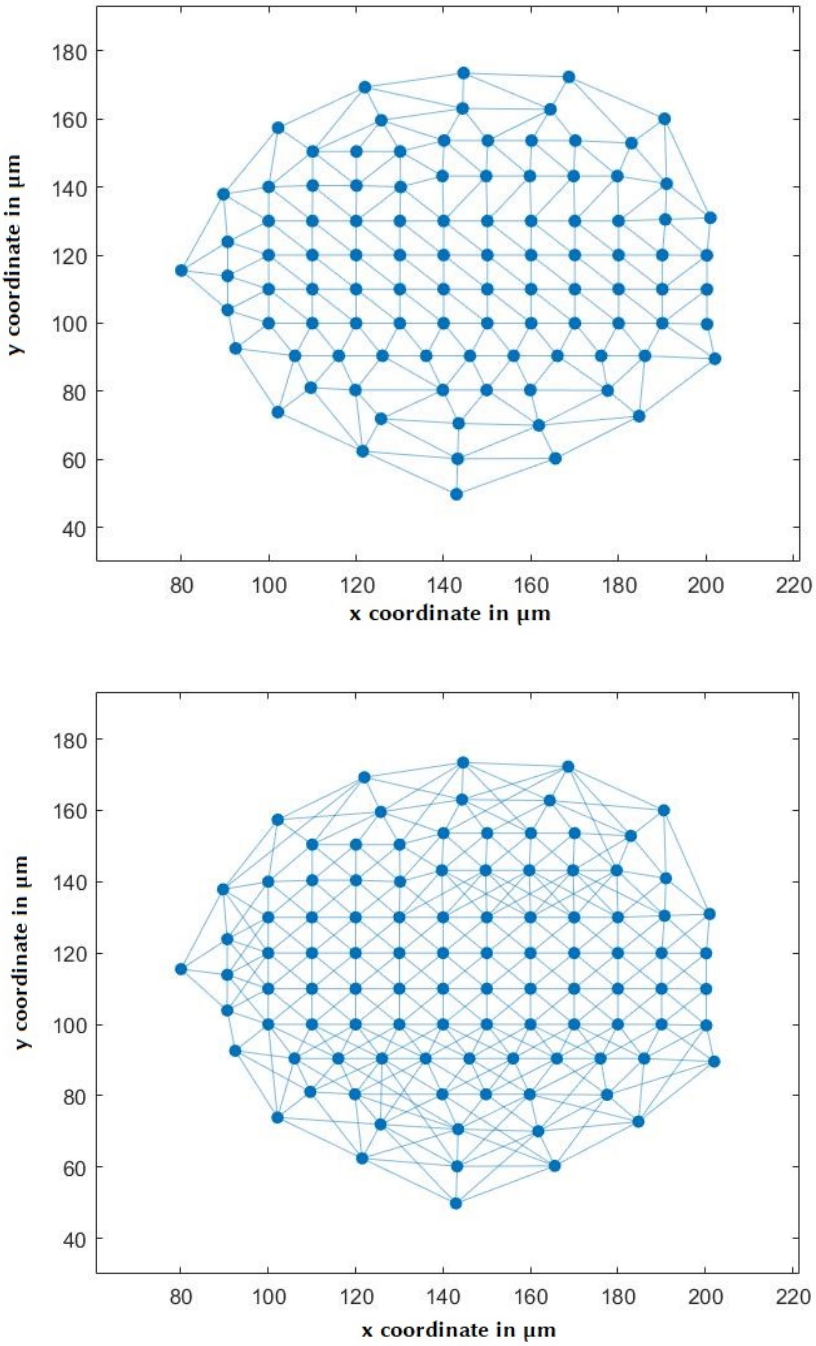

Figure 4.4: Array graph connected by "cleaned" triangulation (on top) and by "cleaned" full connection(on bottom): 39 final traps and 61 reserve traps.

4.2.3 Shortest Path Searching

After "cleaning" operation, the second massive computational challenge is to find the shortest path (in terms of total length) connecting two nodes across the graph. In other words, we have to tell what sequence of edges the optical tweezer has to move atom through, to bring that atom from its initial trap to its final trap.
The "Graph Shortest Path Problem" is a quite common problem, like for satellite navigation system, and its solution function is easily available on many programming platforms. We will discuss the first formulation, "Dijkstra's Algorithm", in Appendix *C*.
The most intuitive algorithm would take a look on loaded atoms distribution and then it would find the nearest atom to some final trap and elaborate atom shortest path to reach it [**49**]. Unfortunately, this is going to cost a lot in terms of total experimen-tal time; as outlined before, it would be useful to spend the most possible computational time before loading atoms. Hence, we store for any final trap its shortest path to any other trap; this means that we need to store $N \times (2N + 2\sqrt{3N})$ paths before the loading phase.
This operation will save a lot of experimental time, for another reason too: since we already know any shortest path between two nodes, it is possible to identify the closest filled trap to the final trap we are trying to fill. We just have to sort all other traps by their distance (in terms of shortest path length) from that final trap; this operation is easily done before the loading phase. In conclusion, we will store all shortest paths for any final traps and its closest traps in a "closeness" list. Taking some final trap to fill, it would be enough to look for the closest filled trap and its already found shortest path to that final trap.
One last question: how can we exploit knowledge on loaded atoms distribution? Something interesting to try cuold be to perform a "Shortest Path" function that counts more "length" to paths passing through nodes where atoms were already loaded, as inspired by traffic apps. This is not particular difficult and would have given the best path every time, but, as widely stressed out before, the first aim is to minimize experimental time, and, since this procedure needs to know were the atoms are loaded in, the whole "finding shortest path" phase would have been spent in experimental phase, increasing heavily the experimental time, even more with such a heavy function as that "atomic-traffic shortest path" one. But a "half-way" solution has been found with an updating parameter we will present soon.

4.2.4 Priority Weight Selection

Before optimization, it has been useful to identify a "weight-function" which could assign "weights" to nodes. I chose graph closeness centrality function, which assigns high weight to central nodes and low weight to external ones, according to node closeness to the mean coordinates values in the following way: the "closeness" centrality type is base on the inverse sum of the distance from a node to all other nodes in the graph. If not all nodes are reachable, then the centrality of node i is:

$$c(i) = (\frac{A_i}{N-1})^2 \frac{1}{C_i}, \tag{4.8}$$

A_i is the number of reachable nodes from node i (not counting i), N is the number of nodes in the graph, and C_i is the sum of distances from node i to all reachable nodes.

With all these values it has been possible to create "priority" list just sorting nodes by weight. In this way the algorithm will fill all the final traps from the most important one to the least important one just by the following that list. It has to be clear that starting filling one or another trap will make reordering process longer or shorter. Taking "centrality" weight-function as a starting point, the optimization aim is to identify a new weight-function that minimizes the total steps needed to reorder all the atoms. More steps mean more experimental time.

After 10^3 simulations, the optimization process has found a "priority weight function" identical to "closeness centrality weight function" except for one node: the node with the highest value of centrality weight has to be halfed in this value. A possible reason why that is the optimized priority weight function could be that, statistically, having a free central node until reordering process reaches its half-way is useful. We could even try to exploit some data mining with some Quantum Machine Learning techniques from [**50**], but will obtain the same weight profile.
Right before atoms loading and imaging process, it would be useful to set any reserve traps weight to zero: it will help in sorting process since those traps are not supposed to be filled by reordering.

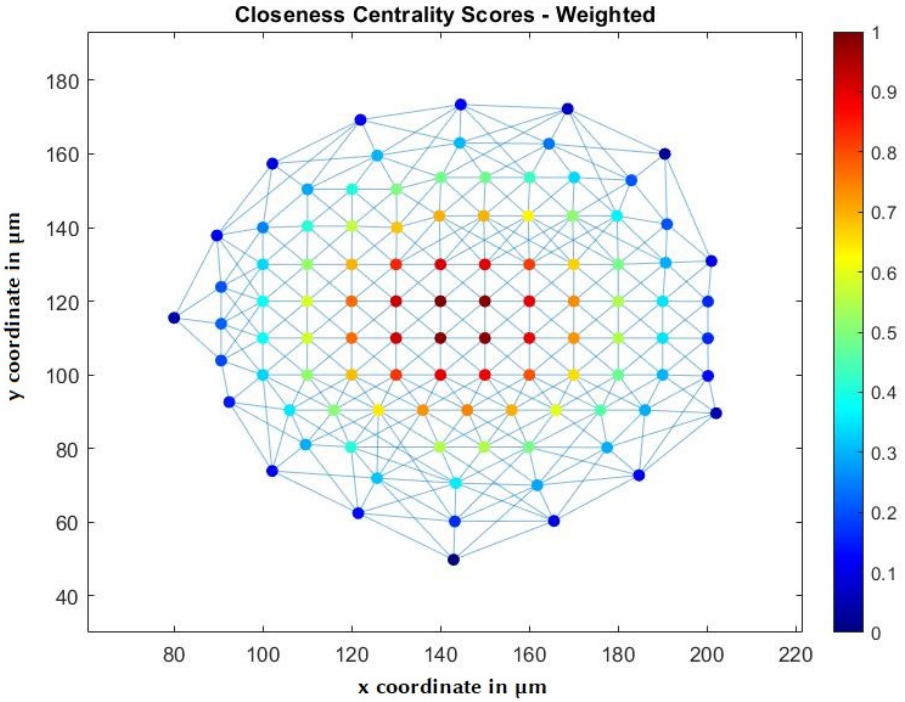

Figure 4.5: Weight function on 100 total traps graph, right before last zero setting for reserve traps.

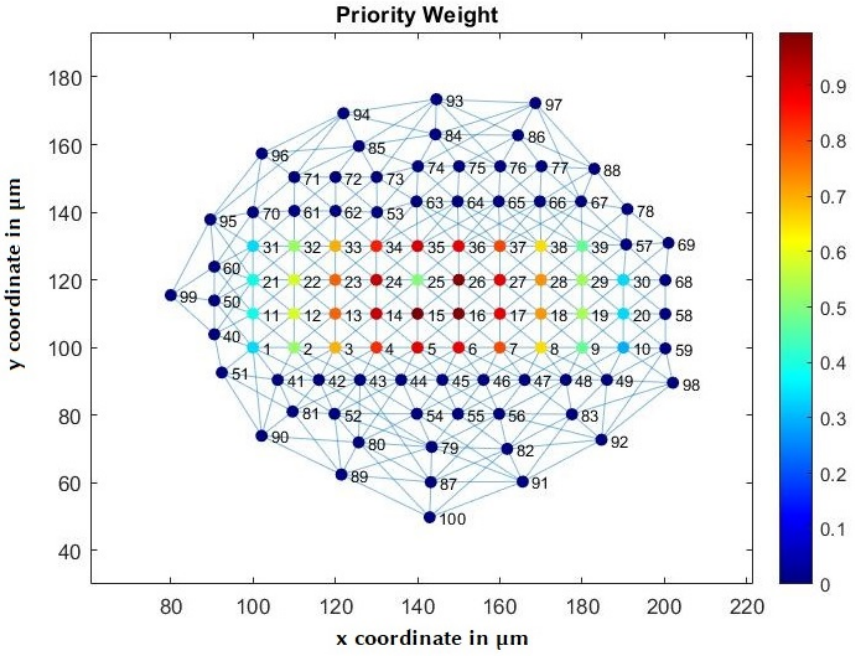

Figure 4.6: Weight function on 100 total traps graph, right before last zero setting for reserve traps.

4.2.5 Priority Weight Updating

Once the imaging process is completed, it is possible to take a look on loaded atoms system. It has been useful to update the "priority" list according to the known atoms distribution on traps, but in thenot computationally heavy way. It has been enough to update the node weight of the filled traps, in the following way:

$$weight(FilledTrap) = \lambda \times weight(FilledTrap), \tag{4.9}$$

with λ "updating" parameter. We thus have an updated "piority" list. Since we are looking for the shortest reordering sequence, we have to optimize "priority" list in terms of total steps. The first optimization has to be performed on the weight-function, the second one on λ, finding the average value $\lambda = 3$.
After this last updating, it is finally possible to sort nodes by priority weight and save that list in "priority". Any final trap is going to be filled starting from the first trap of "priority" to the last, as shown in Fig. 4.8.
This is also the answer to the question arisen in (5.3): how can we exploit our knowledge on the loaded atoms distribution? This would be the best substitution to an inconvenient "atomic-traffic shortest path" function.

Before proceeding further, it is necessary to stress out the following assumption: $\lambda = 3$. This is a good average value but the optimized value is highly sensible to the very geometry of the array. We will perform every simulation not changing the updating parameter λ, in order to show a more emblematic collection of results. It would be useful but not necessary to re-estimate λ according to the very geometry we are using in any experiment. We show below how easily λ changes in function of N and therefore it's very geometry.

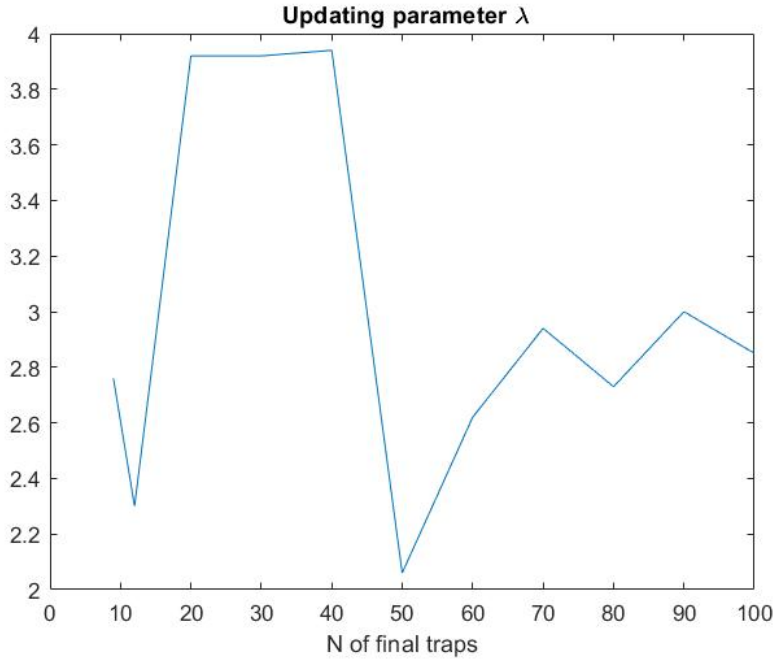

Figure 4.7: Different λ values for number $N$of atoms in a **Spiral Geometry**.

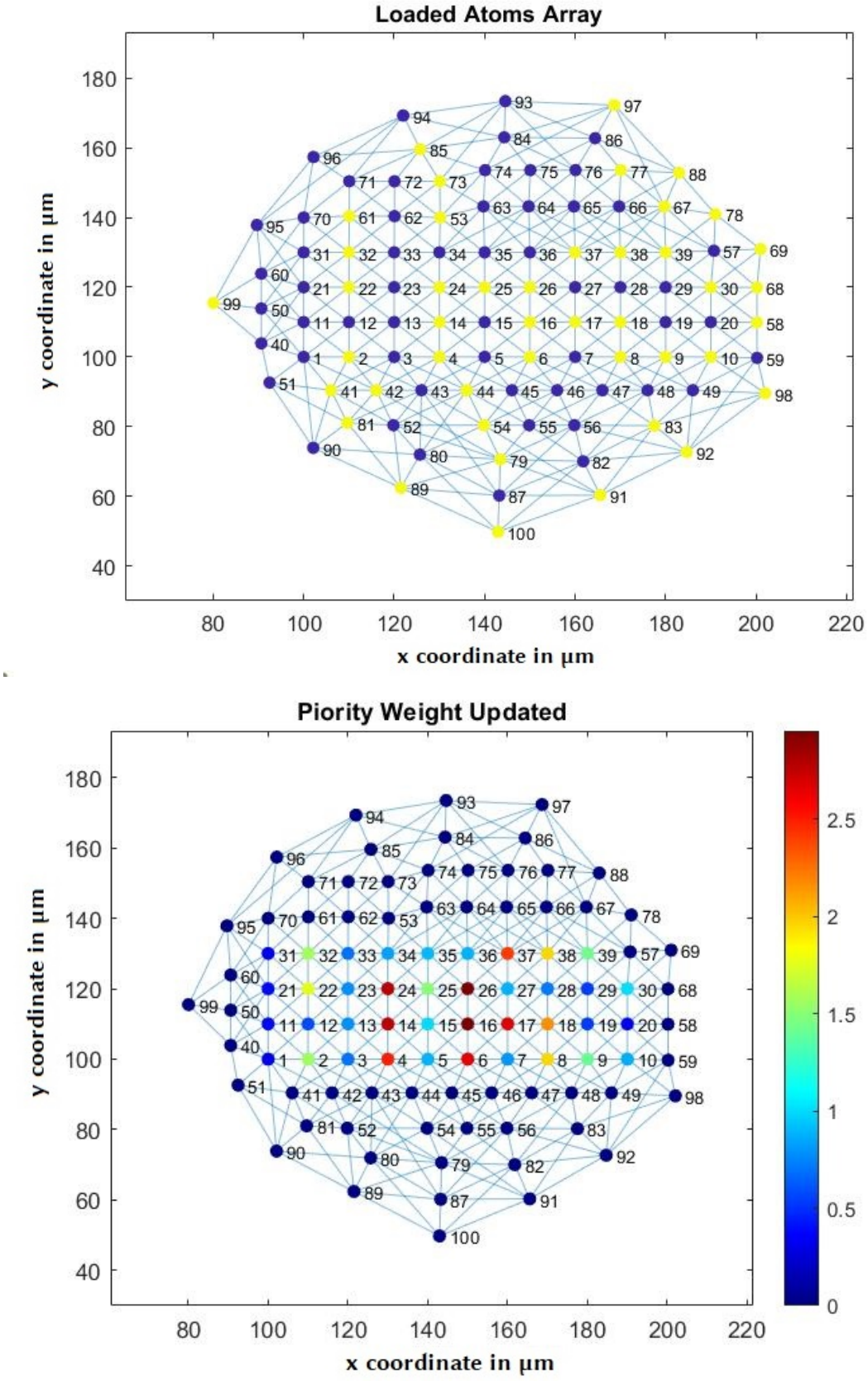

Figure 4.8: Up: Loaded atoms array: yellow dots are filled traps, blue are empty. Down: after imaging process final traps priority weight update. In this case, priority list would be: [16 26 24 14 17 6 4 37 18 38 8 22 32 2 25 39 9 30 15 35 5 36...].

4.2.6 Reordering Process

The last task in reording process is to handle cases in which the shortest path is not a "freeway" but it has to cross already filled nodes. A simple algorithm can give the solution, equally valid for freeway or obstacled paths. Once we store all the traps nodes in shortest path between the closest filled trap and the "to be filled" final trap (both included) in *Path* and if $Atom(i)$ array tells us if it is *true* that i-node is filled, we can then run this:

```
tt=length(Path) %target=to be filled final trap
fw=0; %freeway control
while fw=0
fw=1;
for oo=[1,_,tt-1]
ob=tt-oo; %obstacle flag
if Atom(Path(ob)) true
fw=0;
break
end(if)
end(for)
if fw=0
P=Path(ob,_,tt);
Atom=move(P,Atom,G,x,y);
tt=ob;
end(if)
end(while)
```

where G, x, y are Graph and Nodes Coordinates. The *move* function update *Atom* array according to the atomic distribution after tweezers moving action (through P nodes).

Once all the final traps are filled, we can drop extra atoms.

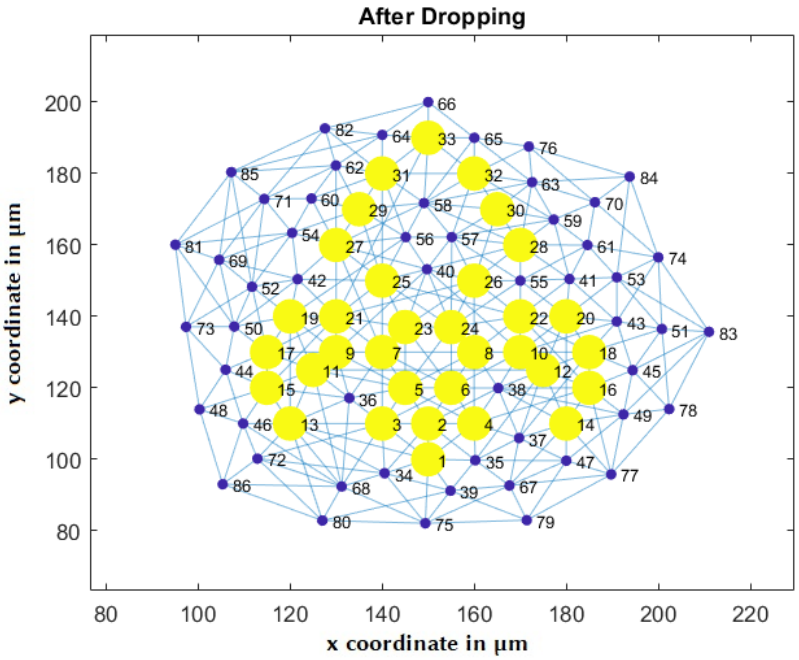

Figure 4.9: After dropping phase for a lily-shaped atoms array.

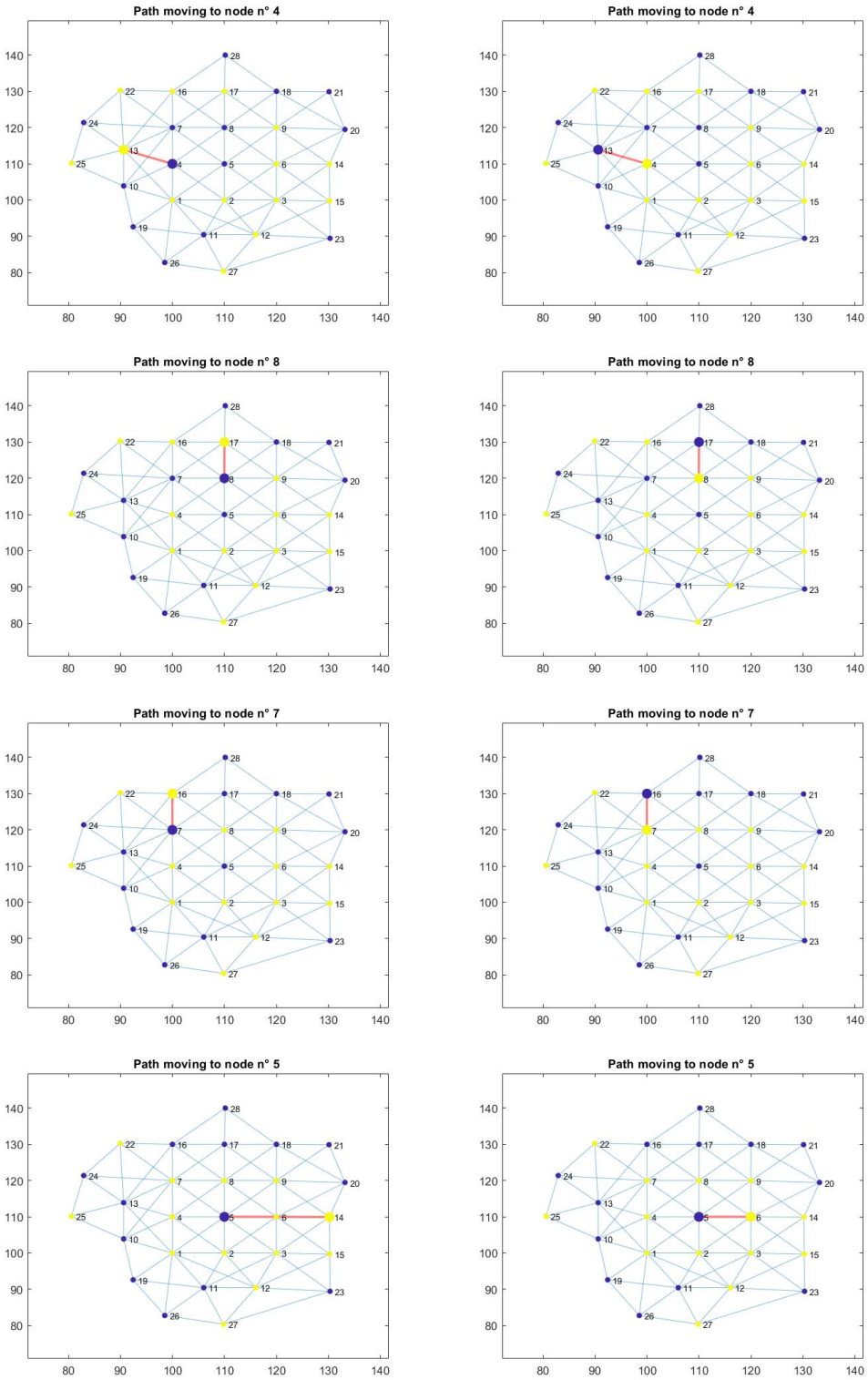

Figure 4.10: Reordering process for a 9 final traps dense rectangular array, illustrated step by step. In a particular step we can have a look on how the algorithm works in case of obstacles: it tries to move an atom from trap number 14 to trap number 5 but the path is blocked by the presence of an atom in 6. The “freeway” protocol has worked just fine.

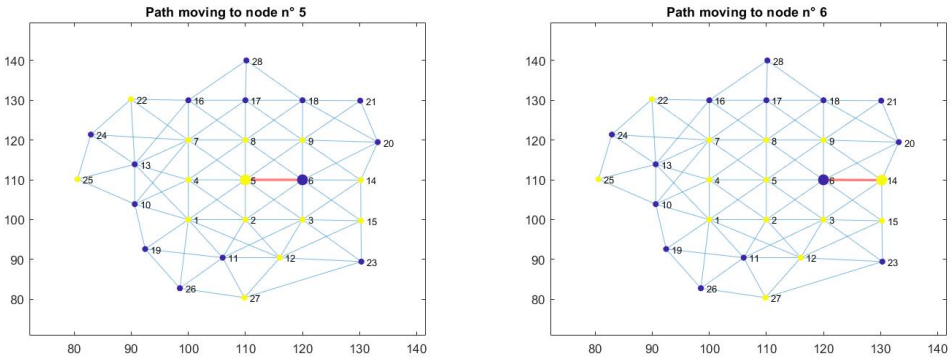

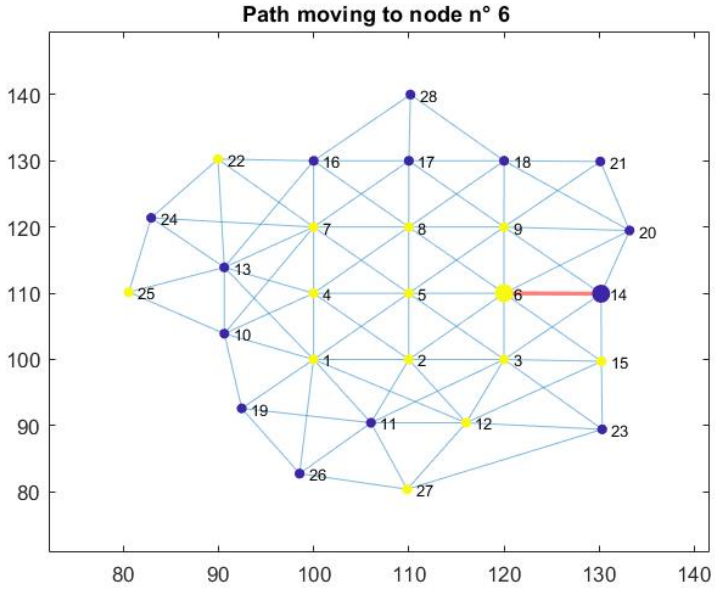

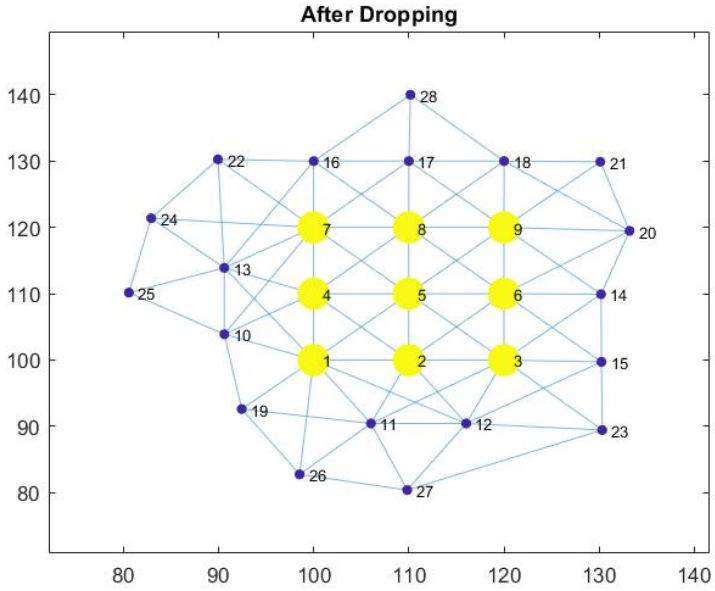

Figure 4.11: Last 4 steps of reordering process for a 9 final traps dense rectangular array, illustrated step by step in the previous Fig. After dropping phase we get the last image. The "priority" reordering algorithm has worked.

4.3 Performances

Finally, we can talk about **optimized performances** and compare them to the "shortest-moves-first" **basic algorithm** many articles have treated [**21**], but before analizing data, a couple of things are useful to be highlighted. The first point that we should stress out is the following: there is no need to talk about optimized computational time since every process is run before the reordering phase; in such sense, the experimental time is reduced to proper time in reading paths matrix and in sorting a list not longer than a couple of hundreds elements and, of course, all the mechanical tweezing time. The second point is about travelled distances: since we are taking examples of more or less dense shapes, the average distance any step counts is averaged to the same value and its quite constant for every graph. Hence, once we have found the effectively shortest path, we can just try to minimize the number of steps, instead of minimizing the effective distance: it leads anyway to the same results.
After noticing the improvement in number of steps between a basis algorithm (triangulation plus simple centrality weights) and the optimized one Fig. 4.12, we can also notice that the number of moved atoms is minimized as well. The first notable thing here has been discovering that optimizing on steps is totally equivalent, in results, to optimizing on moves.

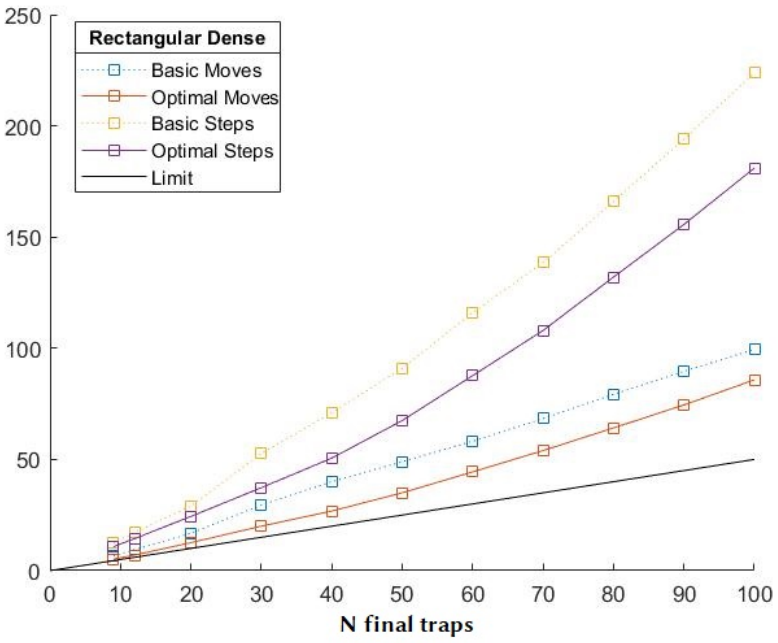

Figure 4.12: **Optimized Algorithm** with updating paratemer $\lambda = 3$ in red and purple, **Basic Algorithm** in blue and gold, for Rectangular Dense Geometry. In black, the "Theoretical Minimum" of $N/2$.

With the protocol we chose to create reserve traps, we are going to be sure of having enough atoms loaded and to exploit the closeness of many atoms to final traps, offering a wider choice. Its downside to our purpouse would be evident in the "dropping atoms" phase: statistically too many atoms were loaded and now they need to be dropped. The basic technique would be to tweeze them away from the array region, one by one. This could be difficult if we are handling a non dense array,

e.g. Spiral Geometry, where many reserve traps could be created in the middle of the shape. In this case tweezing them away could not be the best option: something quick to do would be warming them up, in order to make them jump away from their traps and get lost; nevertheless, we cannot use so focused laser beams on the sample, the risk of losing all the atoms is high. An other option could be to use the same AOD tweezers in such a way they warm undesired atoms out of their traps, but its not as easy as said. The last option, and maybe the best for its global utility, would be having the possibility of using AOD tweezer working in the normal axis of the array plane: in this way it would be easy to lift all atoms up from the array plane and then release them in free space after a couple of μm. This last technique would be resolutive just in a bidimensional work, meanwhile on a 3D work it would be absolutely necessary already in reordering phase. For 3D array, dropping rules might be different: no reserve traps could be created if their atoms are going to be in an "atoms cage".
Once again, experimental time is going to follow the number of steps profile, multiplied by average tweezer switch on and switch off time plus moving time for a step mean length ~ 10 μm.

The theoretical limit $(N/2)$ would still not be violated just by the new "creating reserve traps" protocol since more traps in the array do not make more or less probable for atoms to be loaded directly on final traps.
Algorithm advantage would be more evident if we have been working on the same linked graph, i.e. still on a triangulation method [**19**]. Cleaned Full Connected Graph offers on its own many practical advantages, but a massively heavy computational weight, still spent before the experiment.
We can now take a look on the performance, keeping in mind that these "steps" results are taken including dropping tweezer actions as single steps each.

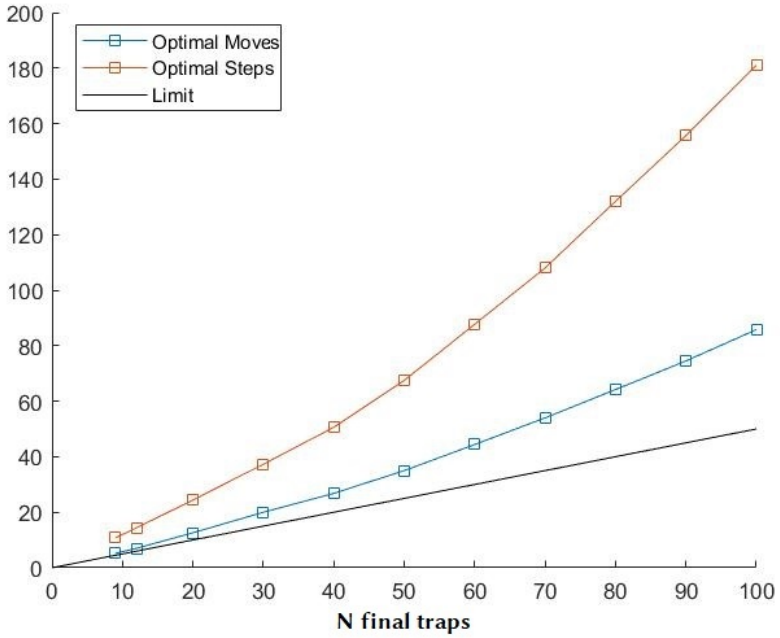

Figure 4.13: **Optimized Algorithm**. In red line Total Steps needed to reorder an N atom array in **Rectangular Dense Geometry**, in blue Total Moved Atom Number. In black the "Theoretical Minimum" $(N/2)$ $\lambda = 3$.

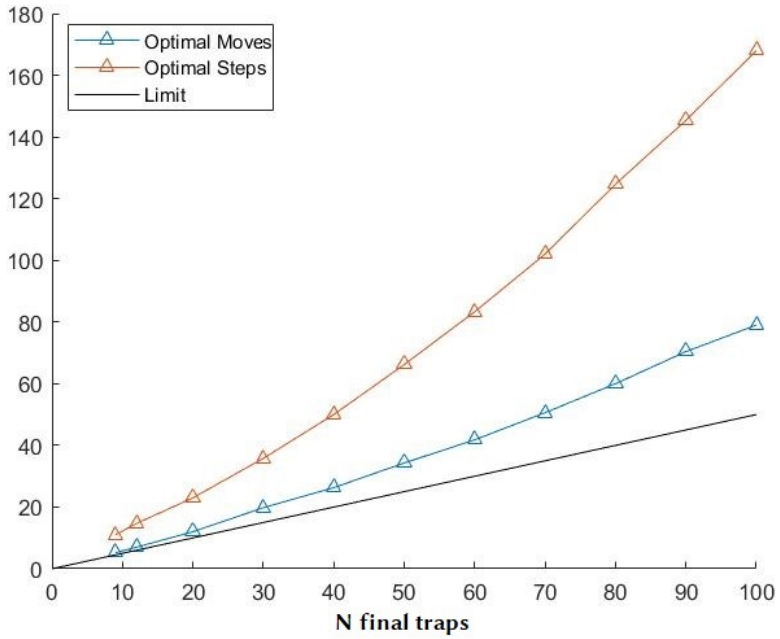

Figure 4.14: **Optimized Algorithm**. In red line, "Total Steps Number" needed to reorder an N atom array in **Triangular Dense Geometry**; in blue, "Total Moved Atom Number". In black, the "Theoretical Minimum" $(N/2)$ $\lambda = 3$.

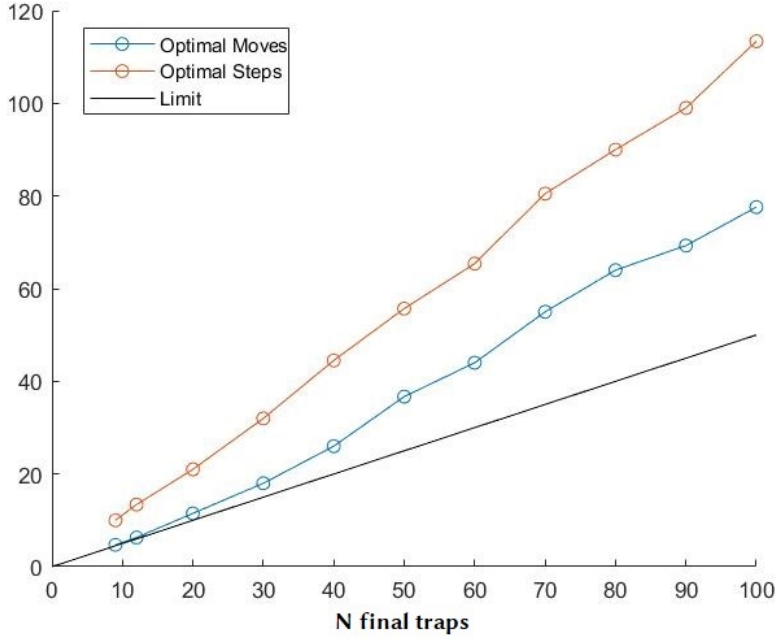

Figure 4.15: **Optimized Algorithm**. In red, line Total Steps needed to reorder an N atom array in **Spiral Geometry**; in blue, "Total Moved Atom Number". In black, the "Theoretical Minimum" $(N/2)$ $\lambda = 3$.

We can notice how the algorithm works and optimizes the reordering process. It is totally feasible on a kind of array geometry with different performances, according to their shape. Triangular Dense Geometry offers always slightly better performances than Rectangular one, but this is not that surprising. Really interesting is to notice

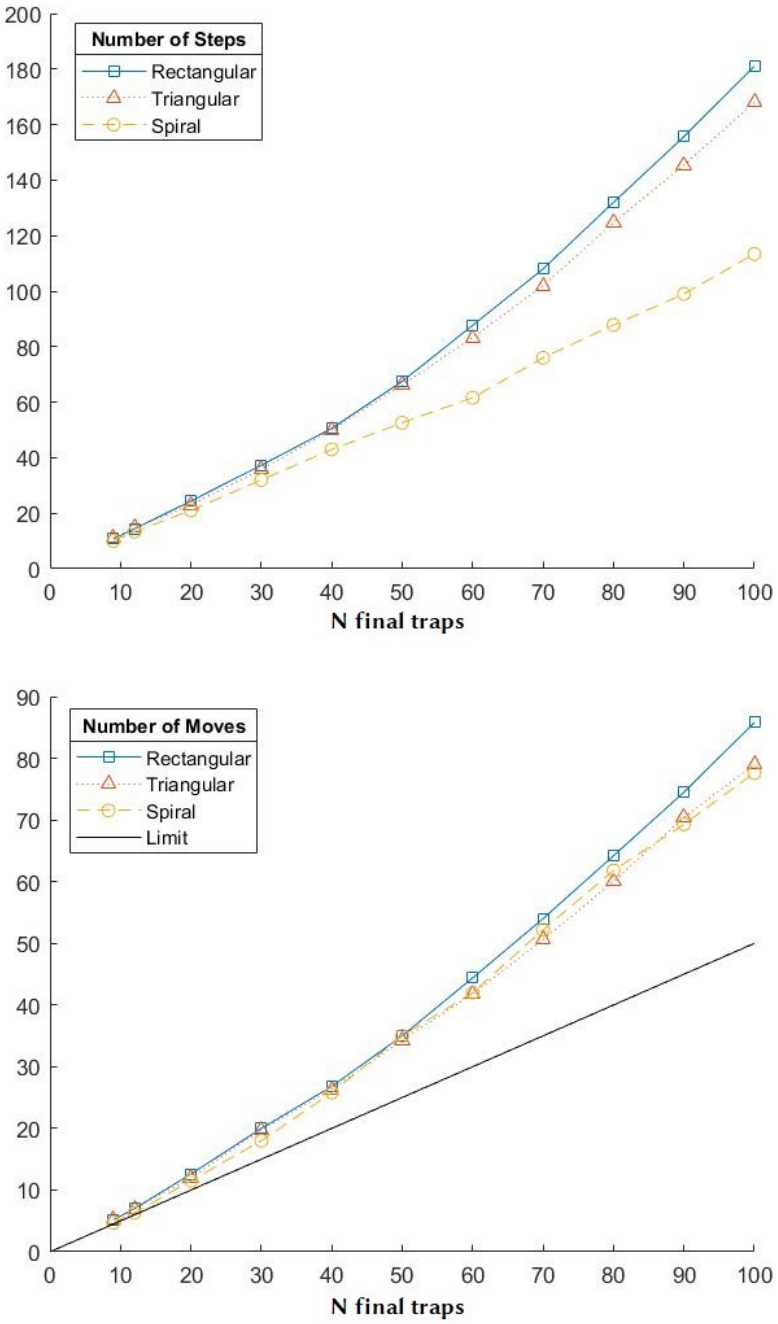

Figure 4.16: **Optimized Algorithm**. Comparison between the three different array geometry: two dense (Rectangular and Triangular) and one "empty" (Spiral). On top "Number of Steps", on the bottom "Number of Moves".

how spiral geometry does not exploit its "emptiness" in the center because of extra reserve traps protocol, but it still performs better than Dense ones in Number of Steps, even if Dropping phase would be more difficult. The Number of Moves is actually the most difficult parameter to further-optimize, since is strictly bound to loading probability.

4.3.1 Quasi-deterministic loading

Some of the most recent researches have proved the possibility to load alkali-earth atoms in a quasi-deterministic way, i.e. atoms in more than 90% of traps [**48**]. Let me now discuss how this might be an advantage in terms of experimental time and if with this new technique a reordering process may be not more necessary. The first point to clearify is "how many extra traps do I need?" Following the same calculation done in (4.2.1), we find the answer $0.13N$. This means that with $1.13N$ total traps, we should get enough atoms (more than N) most of the times (more than 90%). Once the atoms are loaded, we can start the reordering process. Statistically this means that we should move 1 out of 10 atoms into some empty trap, since the other 9 are already in their final traps. For 50 final traps we need 38 total steps and 30 total moves against 52 and 35 with $p = 0.5$, slightly better.

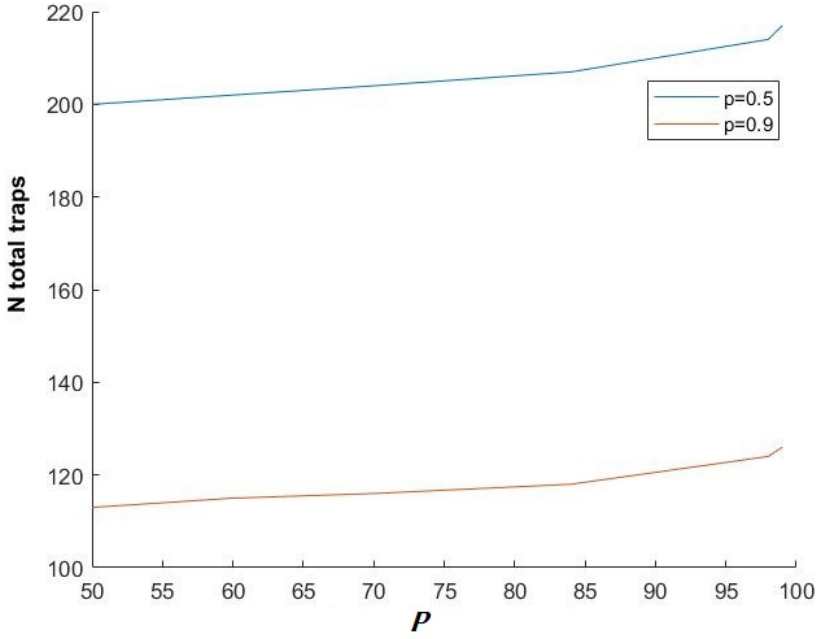

Figure 4.17: Comparison between number of total traps needed in order to have such a percentage of succesfully loaded samples P, as definied in Eq. (4.2), in quasi-deterministic setup($p = 0.9$) and stochastic one($p = 0.5$)

We could now discuss how many reserve traps we need in order to avoid the reordering process most of times, just rejecting those loaded setup not having already all the final traps filled. A simulation could clearify this point faster than statistical considerations: even with $100 \times N$ total traps, final configuration could not be reached without reordering process in 98% of times. Anyway, this is important because it underscores the necessity to reorder atoms in such loaded arrays.

The next point to understand is how extra atoms dropping would affect the performance of reordering such a loaded array. We can see from figure below that the extra-atoms number grows with number of extra traps (represented by success loading percentage) but it not only has a higher relative weight over total moves than stochastic ($p = 0.5$) arrays but it actually overcomes stochastic-array extra-atoms number after 90% of success loaded arrays. Anyway, the total experimental time for such quasi-deterministic loading, in steps terms, is way lower (over 4 times)

than stochastic one, as shown below.

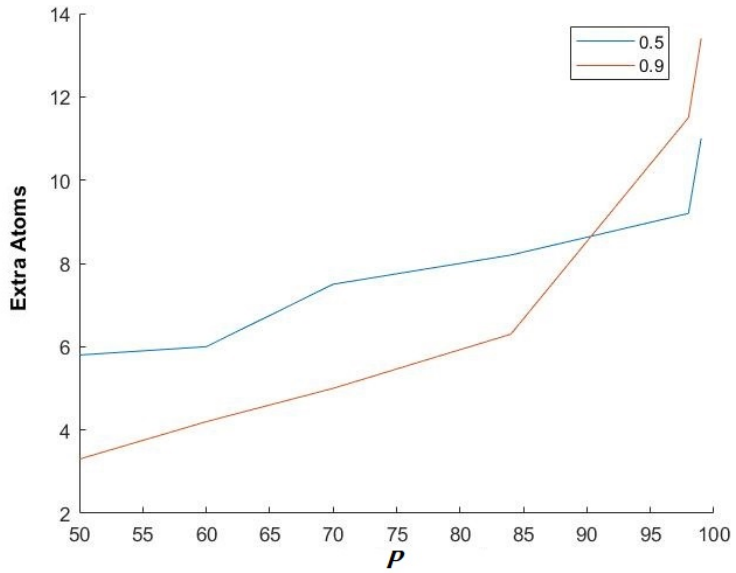

Figure 4.18: In order to compare number of extra-atoms to be dropped in the two different loading setups ($p = 0.9$, $p = 0.5$), it is more useful to visualize these on a x-axis reporting the percentage of success P, as definied in Eq. (4.2), for an "enough-atoms" loading.

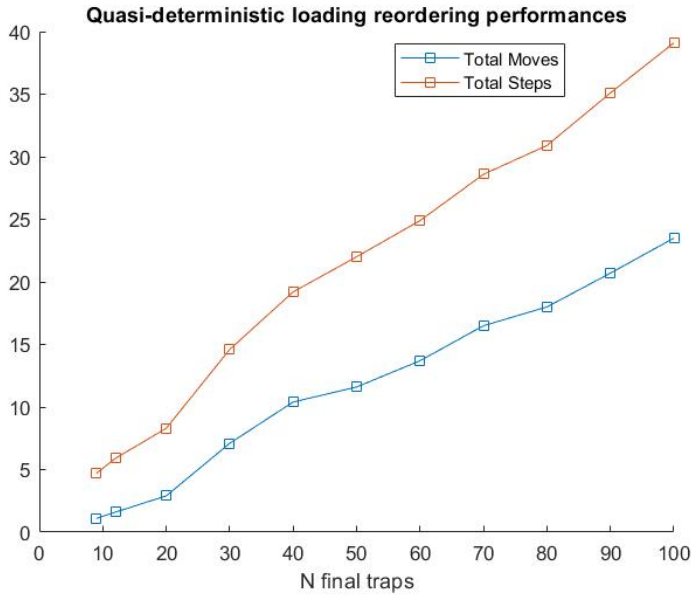

Figure 4.19: **Optimized Algorithm** on a quasi-deterministic loaded atoms array. **Rectangular Dense Geometry** has been chosen because it is well representative of Dense Geometry that intuitively affects more a loading process where only few empty traps could be localized in the center of the array, causing possible several reordering steps. $\lambda = 3$.

We suddenly say that a quasi-deterministic loading is always preferable but new and more efficient dropping techniques could be more necessary and useful than in the stochastic case.

Chapter 5

Conclusions

We will now summarize what we have here pursued and achieved and to find a conclusion. Firstly we have learned how to exploit Sr features through cooling and manipulation techniques, in order to create Rydberg atoms costumizing arrays and use them as multi-qbits machines. We have understood Optical Twezing importance and how to use OTs in AOD and SLM generation to trap and reorder single atoms with high reliability and high speed. The main issue while creating such arrays is the time: to load and reorder atoms very specific environment is required. We must provide in the void loading cell a Pressure $\sim 10^{-11}$ torr and a average atom lifetime ~ 60 s. The whole process has to be done in the lowest time.

The first main problem of this thesis has been the optimization of the fluorescence imaging process of a single atom only through simulations. Fluorescence and Cooling phases have been studied in a three-level system. In order to minimize the imaging time without losing reliability (i.e. *Fidelity* and *Survival* parameters), the best intensities of imaging and cooling laser beams have been identified to guaranteed in such short time (10 ms) the biggest amount of photon on the camera. After the signal and noise analysis we confirmed the succes of those parameters.

The following step was to develop a new protocol of reordering, a "priority" algorithm. Once again, the global aim was to minimize the experimental time. In this case an optimization was performed over the number of step the atoms must follow across the array in reordering phase. For this task a Machine Learning technique could have identified the global "priority" function, but the initial configuration has provided a luckly good solution. This optimization offers the possibility to load and reorder a high number of atoms in a reasonably short time. Number of steps grows quite linearly ($\sim N^{1.26}$) with the number of desired atoms. We have also treated the possibility of a quasi-deterministic loading and its advantages. In that occasion, we underlined the inconvenience of dropping time and how it affects reordering time optimization. We only considered solutions of tweezing all extra-atoms away, one by one, but another possible solution might be to switch off and then back on SLM OTs to drop all the extra atoms. But this solution is still far to be evaluated as practical.

Quantum computing theoretical advantages, such as [**51**, **52**, **53**], are coming and developed day after day and it is time to provide a good and concrete basis where to exploit those techniques. In future, these platforms will be highly useful and required and Rydberg atoms seem to be a truly promising basis [**54**, **55**]. New Machine Learning techniques, based on spontaneous emission of Rydberg atoms Neural Network, are capable of learning biological tasks and even run in multitasking [**56**]. Ref. [**57**] have developed procedures for measuring the similarity between graph-structured data, based on the time evolution of a quantum system. Hence, in conclusion, quantum optimization procedures have being discovered day after day [**59**] and I can see in this work a good starting point for the realization of bigger and bigger qbits arrays in less and less time.

Acknowledgements

At the end of this work, I sincerely need to spend couple of words for the very team behind this thesis. I offer my deepest gratitude to Prof. Filippo Caruso and Prof. Leonardo Fallani not only for helping and leading me along this thesis study but also for teaching and inspiring me during my Master exams and even beyond their respective fields. I also thank, countless times, Giacomo Cappellini, Vladislav Gavryusev and Luca Guariento for their infinite patience, absolute competence, and massive sympathy. More indirectly I want to thank the University of Florence and the Physics Department for the opportunity and the honor to learn and work in this important dimension.

Time has been the main topic of this work and, in a way, of my whole study. For me it is always the time to thank all the people that lived with me this university world, in particular Tommaso Rossetti and Gregorio Pekala who know best what this journey meant to me.

I want to thank the distracting friends who shared with me the other half of my life, especially Alessandro Visconti and Alessandro Cecchi.

The continuous support in this work came from my family, my brothers Alessandro and David, and my sister Micol, and more primarily from my parents, alias Babbo and Mamma, who dosed me relax and pressure, trust and love, in the most motivating way, without knowing how.

Bibliography

[1] Ehud Altman (2021) *Quantum Simulators: Architectures and Opportunities*, PRX Quantum 2(1) (2021): 017003.

[2] Luca Guariento (2021) *Development of Optical Tweezer techniques with Acousto Optic Deflectors for atomic quantum simulators.*

[3] Browaeys, A., & Lahaye, T. (2020).*Many-body physics with individually controlled Rydberg atoms*. Nature Physics, 16(2), 132-142.

[4] Bermejo-Vega, Juan, et al. *Architectures for quantum simulation showing a quantum speedup.* Physical Review X 8.2 (2018): 021010.

[5] Haferkamp, Jonas, et al. *Closing gaps of a quantum advantage with short-time hamiltonian dynamics.* Physical Review Letters 125(25) (2020): 250501.

[6] Sweke, Ryan, et al. *Stochastic gradient descent for hybrid quantum-classical optimization.* Quantum 4 (2020): 314.

[7] Islam, R., et al. *Emergence and frustration of magnetism with variable-range interactions in a quantum simulator.* Science 340 (2013): 583-587.

[8] Barends, Rami, et al. *Digitized adiabatic quantum computing with a superconducting circuit.* Nature 534 (2016): 222-226.

[9] M. A. Nielsen, I. L. Chuang, *Quantum Computation and Quantum Information.* ()Cambridge Univ. Press. 2000).

[10] Giovannetti, Vittorio, Seth Lloyd, and Lorenzo Maccone. *Advances in quantum metrology.* Nature photonics 5(4) (2011): 222-229.

[11] Georgescu, Iulia M., Sahel Ashhab, and Franco Nori.*Quantum simulation.* Reviews of Modern Physics 86(1) (2014): 153.

[12] Bakr, Waseem S., et al. *A quantum gas microscope for detecting single atoms in a Hubbard-regime optical lattice.* Nature 462 (2009): 74-77.

[13] Zeiher, Johannes, et al. *Microscopic characterization of scalable coherent Rydberg superatoms.* Physical Review X 5.3 (2015)

[14] Labuhn, Henning, et al. *Tunable two-dimensional arrays of single Rydberg atoms for realizing quantum Ising models.* Nature 534 (2016): 667-670.

[15] de Léséleuc, Sylvain, et al. *Observation of a symmetry-protected topological phase of interacting bosons with Rydberg atoms.* Science 365 (2019): 775-780.

[16] Schlosser, Nicolas, et al.*Sub-poissonian loading of single atoms in a microscopic dipole trap.* Nature 411 (2001): 1024-1027.

[17] Barredo, Daniel, et al. *An atom-by-atom assembler of defect-free arbitrary two-dimensional atomic arrays.* Science 354 (2016): 1021-1023.

[18] Endres, Manuel, et al. *Cold matter assembled atom-by-atom.* arXiv preprint arXiv:1607.03044 (2016).

[19] Schymik, Kai-Niklas, et al. *Enhanced atom-by-atom assembly of arbitrary tweezer arrays.* Physical Review A 102.6 (2020).

[20] Lee, Woojun, Hyosub Kim, and Jaewook Ahn. *Three-dimensional rearrangement of single atoms using actively controlled optical microtraps.* Optics express 24.9 (2016).

[21] Schymik et alter (2020) *Enhanced atom-by-atom assembly of arbitrary tweezer arrays*, Physical Review A 102.

[22] Morgado, M., and S. Whitlock. *Quantum simulation and computing with Rydberg-interacting qubits.* AVS Quantum Science 3.2 (2021).

[23] Saskin, Samuel, et al. *Narrow-line cooling and imaging of ytterbium atoms in an optical tweezer array.* Physical review letters 122.14 (2019).

[24] Ivaylo Sashkov Madjarov (2021) *Entangling, controlling and detecting individual strontium atoms in optical tweezer arrays.*PhD thesis, California Institute of Technology, Pasadena, California, 2021.

[25] Schmiedmayer, Jörg, Ron Folman, and Tommaso Calarco. *Quantum information processing with neutral atoms on an atom chip.* Journal of Modern Optics 49.8 (2002): 1375-1388.

[26] Urban, E., et al. *Observation of Rydberg blockade between two atoms.* Nature Physics 5.2 (2009): 110-114.

[27] Thompson, Jeffrey Douglas, et al. *Coherence and Raman sideband cooling of a single atom in an optical tweezer.* Physical review letters 110.13 (2013).

[28] Manuel Endres et al. *Atom-by-atom assembly of defect-free onedimensional cold atom arrays.* Science, 354(6315):1024–1027, (2016).

[29] H. Bernien et al. *Probing many-body dynamics on a 51-atom quantum simulator.* Nature, 551(7682):579–584, Nov 2017.

[30] Fuhrmanek, A., et al. *Light-assisted collisions between a few cold atoms in a microscopic dipole trap.* Physical Review A 85.6 (2012).

[31] Giacomo Cappellini (2015) *Two-orbital quantum physics in Yb Fermi gases exploiting the 1S0 to 3P0 clock transition*

[32] O. Svelto. *Principles of Lasers.* (Springer US, 2010.)

[33] Wang T.T. Levine H. et al. Ebadi, S. *Quantum phases of matter on a 256-atom programmable quantum simulator.* Nature Physics, 595:227–232, 2021.

[34] Schuler M. Williams H.J. et al. Scholl, P. *Quantum simulation of 2d antiferromagnets with hundreds of rydberg atoms.* Nature Physics, 595:233–238, 2021.

[35] Cooper, Alexandre, et al. *Alkaline-earth atoms in optical tweezers.* Physical Review X 8.4 (2018).

[36] Steck, Daniel A. *Quantum and atom optics.* (2007).

[37] Mølmer, K., Castin, Y. and Dalibard, J. *Monte Carlo wave-function method in quantum optics.* Journal of the Optical Society of America B 10, 524 (1993).

[38] Taïeb, R., Dum, R., Cirac, J.I., Marte, P. and Zoller, P. *Cooling and localization of atoms in laser-induced potential wells.* Physical Review A 49, 4876–4887 (1994).

[39] Ivanov, V.V. and Gupta, S. *Laser-driven Sisyphus cooling in an optical dipole trap.* Physical Review A 84, (2011).

[40] Hilker, Timon A. *Spin-resolved microscopy of strongly correlated fermionic many-body states.* Diss. Ludwig Maximilians Universität München, (2017).

[41] M. B. Plenio and P. L. Knight *The quantum-jump approach to dissipative dynamics in quantum optics* (1998)

[42] Bergschneider, Andrea, et al. *Spin-resolved single-atom imaging of Li 6 in free space.* Physical Review A 97.6 (2018): 063613.

[43] Urech, Alexander, et al. *Narrow-line imaging of single strontium atoms in shallow optical tweezers.* arXiv preprint arXiv:2202.05727 (2022).

[44] Vladislav Gavryusev *Imaging of Rydberg Impuritues in an Ultracold Atomic Gas.* (2016)

[45] Araneda, G.,Walser, S., Colombe, Y. et al. Wavelength-scale errors in optical localization due to spin–orbit coupling of light. Nature Physics 15, 17–21 (2019).

[46] Gallagher, Alan, and David E. Pritchard. *Exoergic collisions of cold Na.* Physical review letters 63.9 (1989): 957.

[47] M. Born, E.Wolf, et al. Principles of Optics: Electromagnetic Theory of Propagation, Interference and Diffraction of Light. (Cambridge University Press, 1999.)

[48] Dalibard, Jean, and Claude Cohen-Tannoudji. *Laser cooling below the Doppler limit by polarization gradients: simple theoretical models.* JOSA B 6.11 (1989): 2023-2045.

[49] Jenkins, Alec, et al. *Ytterbium nuclear-spin qubits in an optical tweezer array.* Physical Review X 12.2 (2022).

[50] Chopde, Nitin R., and Mangesh Nichat. *Landmark based shortest path detection by using A* and Haversine formula.* International Journal of Innovative Research in Computer and Communication Engineering 1.2 (2013): 298-302.

[51] Peter Wittek (2014) *Quantum Machine Learning*

[52] D. Gross, S. T. Flammia, and J. Eisert *Most quantum states are too entangled to be useful as computational resources* (2008)

[53] David T. Stephen, Hendrik Poulsen Nautrup, Juani Bermejo-Vega, and J. Eisert and Robert Raussendorf *Subsystem symmetries, quantum cellular automata, and computational phases of quantum matter* (2019)

[54] Wintermantel, T. M., et al. *Unitary and nonunitary quantum cellular automata with Rydberg arrays.* Physical Review Letters 124(7) (2020).

[55] Ramette, Joshua, et al. *Any-to-any connected cavity-mediated architecture for quantum computing with trapped ions or Rydberg arrays.* PRX Quantum 3(1) (2022).

[56] Bravo, Rodrigo Araiza, et al. *Quantum reservoir computing using arrays of Rydberg atoms.* arXiv preprint arXiv:2111.10956 (2021).

[57] Henry, Louis-Paul, et al. *Quantum evolution kernel: Machine learning on graphs with programmable arrays of qubits.* Physical Review A 104.3 (2021).

[58] Zhu, Cheng, et al. *Improved Harris Hawks Optimization algorithm based on quantum correction and Nelder-Mead simplex method.* Mathematical Biosciences and Engineering 19.8 (2022).

[59] Young, Hugh D., *Statistical Treatment of Experimental Data.* (McGraw-Hill Book Company, New York, 1962).

[60] E.W.Dijkstra (1959) *A Note on Two Problems in Connexion with Graphs*, Numerische Matematik 1, 269-271.

Appendix A

OBE Solutions and Radiative Forces

In order to evaluate d^{st}, we will start from the *adiabatic approximation*: we will consider a system internally evolving for a time scale much smaller than the external one ($T_{int} \ll T_{est}$) with the following results:
-We can now consider $\mathbf{R}, \mathbf{P}$ as classical variables,i.e. not operators anymore (with notation $\vec{R}$).
-A stationary internal state can be identifyiedby the the stationary Optical Bloch Equations (OBE) solutions (Sec.3.3). We theore obtain:

$$\mathbf{F} =< \hat{d}_i \nabla E_i(\vec{R}) > + < \nabla \hat{d}_i > E_i(\vec{R}), \tag{A.1}$$

where the second term is neglectable since *adiabatic approximation* makes $< \nabla \hat{d}_i >$ contribution fade out quickly, obtaining

$$\vec{F} = \hat{d}_i \nabla E_i(\vec{R}), \tag{A.2}$$

If we now recall $\hat{\vec{d}} = -e\hat{\vec{r}}$, we study

$$tr[\hat{\rho}\hat{\vec{d}}] = e \cdot tr[\hat{\rho}\hat{\vec{r}}] = e \cdot tr[\begin{pmatrix} \rho_{00} & \rho_{01} \\ \rho_{01}^* & \rho_{11} \end{pmatrix} \begin{pmatrix} 0 & \vec{\mu}_{01} \\ \vec{\mu}_{10} & 0 \end{pmatrix}]. \tag{A.3}$$

Hence, we can write:

$$\vec{d} = (\rho_{01}\vec{\mu}_{10} + \rho_{10}\vec{\mu}_{01}) = -e\vec{\mu}_{01}(\tilde{\rho}_{10}e^{-i\omega t} + \tilde{\rho}_{01}e^{+i\omega t}) \tag{A.4}$$

where with $\tilde{\rho}$ we denote RWA variables. If we now consider steady solution to Bloch Equations in (3.39):

$$\begin{cases} \Delta\dot{\tilde{\rho}} = -i(\Omega\tilde{\rho}_{ge} - \Omega^*\tilde{\rho}_{eg}) - \gamma(\Delta\tilde{\rho} + 1) \\ \dot{\tilde{\rho}}_{ge} = i\delta\tilde{\rho}_{eg} + \frac{i}{2}\Omega\Delta\tilde{\rho} - \frac{\gamma}{2}\tilde{\rho}_{eg} \\ \dot{\tilde{\rho}}_{ge} = i\delta\tilde{\rho}_{ge} + \frac{i}{2}\Omega^*\Delta\tilde{\rho} - \frac{\gamma}{2}\tilde{\rho}_{eg} \end{cases} \tag{A.5}$$

with $\Delta\tilde{\rho} = (\tilde{\rho}_{ee} - \tilde{\rho}_{gg})$ and if we now recall new variables u^{st} and v^{st} from (2.7)

$$\begin{cases} u^{st} = \frac{\Omega\delta}{\delta^2+\gamma^2/4+\Omega^2/2} \\ \\ v^{st} = \frac{\Omega\gamma/2}{\delta^2+\gamma^2/4+\Omega^2/2} \end{cases}, \tag{A.6}$$

we notice that we can write the "steady state" solution $\tilde{\rho}_{10}^{st} = \tilde{\rho}_{10}(t \to \infty)$ as

$$\tilde{\rho}_{10}^{st} = \frac{\Omega}{2} \cdot \frac{\delta - i\gamma/2}{\delta^2 + \gamma^2/4 + \Omega^2/2} = \frac{1}{2}(u^{st} - iv^{st}). \tag{A.7}$$

Coming back on $\vec{d}^{st}$ evaluation:

$$\begin{aligned} \vec{d} &= -\tfrac{e}{2}\vec{\mu}_{10}[(u^{st} - iv^{st})e^{-i\omega t} + (u^{st} + iv^{st})e^{+i\omega t}] = \\ &= -e\vec{\mu}_{10}[u^{st}\cos\Big(\omega t + \phi(\vec{R})\Big) - v^{st}\sin\Big(\omega t + \phi(\vec{R})\Big)] \end{aligned} \tag{A.8}$$

where ϕ is the $\vec{E} = \vec{e}\epsilon\cos(\omega t + \phi)$ electric field fase, therefore u^{st} is in phase with $\vec{E}(\vec{R})$ driving electric field and v^{st} is in counterphase with it.
If we now want to extend the study to the global $\vec{F} = \sum_{i\in[x,y,z]} d_i^{st}\nabla E_i(\vec{R})$, introducing $\theta(t, \vec{R}) = \omega t + \psi(\vec{R})$, with $\vec{i}$ canonical base $x - y - z$ versor, we obtain

$$\begin{cases} \vec{F} = \sum_i e(\vec{i}\cdot\vec{\mu}_{10})(u^{st}\cos\theta - v^{st}\sin\theta) \\ \nabla E_i(\vec{R}) = (i\cdot\vec{e})[\nabla\epsilon\cos\theta - \epsilon\nabla\phi\sin\theta], \end{cases} \tag{A.9}$$

where $\vec{e}$ is $\vec{E}$ polarization versor and ϵ is its intensity. Combining these two equations together, we get

$$\vec{F} = -e(\vec{\mu}_{10}\cdot\vec{e})[u^{st}\nabla\epsilon\cos^2\theta + v^{st}\epsilon\nabla\psi\sin^2\theta + u^{st}\epsilon\nabla\phi\cos\theta\sin\theta - v^{st}\nabla\epsilon\sin\theta\cos\theta]. \tag{A.10}$$

Since we are conisdering average value of $\vec{F}$, in particular on a time scale that is associated to the motion of the atom, this expression has many time dependences in θ, we can consider these time dependences as relatively fast, i.e. θ has *optical* frequency ($10^{15}Hz$). Hence, the dynamics of the atom is much slower and we can take the time average value of this expression.

$$< \vec{F} >_t = -e(\vec{\mu}_{10}\cdot\vec{e})\frac{1}{2}[u^{st}\nabla\epsilon + v^{st}\epsilon\nabla\phi] \tag{A.11}$$

Now, if we remember *Rabi Frequency* $\Omega = e\epsilon\vec{\mu_{01}}\cdot\vec{e}/\hbar$ and we notice that $\nabla\epsilon = \nabla\Omega$, we finally obtain a simple time-averaged expression of $\vec{F}$

$$\vec{F} = -\frac{\hbar\nabla\Omega}{2}u^{st} - \frac{\hbar\Omega\nabla\phi}{2}v^{st}, \tag{A.12}$$

where we must distinguish the first term as *Dipole Force* and the second one as *Radiation Pression Force* as outlined in Eq.(2.8).

Appendix B

Binomial to Gaussian distribution

Despite their differences, there is a connection between Binomial and Gaussian distributions [**58**]. If we consider Binomial distribution - $B_{M,p}(n) = \binom{M}{n} p^n q^{M-n}$, where n is the number of successes and M is the number of attempts, with p fixed single event probability and $q = 1 - p$ - for high values of M attemps, $B_{M,p}(n)$ is well approximated by a Gaussian distribution

$$G_{X,\sigma}(n) = \frac{1}{\sigma\sqrt{2\pi}} e^{-(n-X)^2/2\sigma^2} \tag{B.1}$$

with $X = Mp$ and $\sigma = \sqrt{Mpq}$.
Here we show the demonstration. To evaluate the sum:

$$X = \sum_{n=0}^{M} n \binom{M}{n} p^n q^{M-n}. \tag{B.2}$$

we note that is similar to the expression of the normalization of the binomial distribution, namely,

$$\sum_{n=0}^{M} \binom{M}{n} p^n q^{M-n} = 1. \tag{B.3}$$

The difference is that the sum in Eq.(B.2) contains an extra factor, n. By the way, by a means of a trick we can convert this into the form of the sum in Eq.(B.3).

From here on we drop the limits on the sum, remembering always that n ranges from 0 to M. Now we differentiate both sides of Eq.(B.2) with respect to p, which is legitimate bacause the equation is true for all values of p between 0 and 1, as observed earlier. The advantage of doing this will appear clearer shortly.
Taking the derivative,

$$\sum_{n=0}^{M} \binom{M}{n} [p^{n-1} n(1-p)^{M-n} p^n (1-p)^{M-n-1}] = 0, \tag{B.4}$$

we can now rewrite it as

$$\begin{aligned} \sum \binom{M}{n} np^{n-1}(1-p)^{M-n} &= \sum \binom{M}{n} (M-n) p^n (1-p)^{M-n-1} \\ &= M \sum \binom{M}{n} p^n (1-p)^{M-n-1} - \sum \binom{M}{n} np^n (1-p)^{M-n-1}, \end{aligned} \tag{B.5}$$

or, in another way,

$$\sum n \binom{M}{n} [p^{n-1}(1-p)^{M-n}+p^n(1-p)^{M-n-1}] = M \sum \binom{M}{n} p^n(1-p)^{M-n-1}. \quad \text{(B.6)}$$

We now multiply both sides of equation by $p(1-p)$, obtaining

$$\sum n \binom{M}{n} [(1-p)p^n(1-p)^{M-n} + p \times p^n(1-p)^{M-n}] = Mp \sum \binom{M}{n} p^n(1-p)^{M-n}. \quad \text{(B.7)}$$

Now, combining these two terms on the left side, and using Eq.(B.2) on the right side,

$$\sum n \binom{M}{n} (1-p)p^n(1-p)^{M-n} = Mp \sum n f_{M,p}(n) = Mp. \quad \text{(B.8)}$$

Hence, the left side of this expression is just our original expression for X (B.2), therefore we conclude that

$$X = Mp. \quad \text{(B.9)}$$

The calculation of σ proceeds in analog manner. The variance is given by

$$\sigma^2 = \sum (n - Mp)^2 f_{M,p}(n). \quad \text{(B.10)}$$

To evaluate this sum, we first rewrite Eq.(B.9) as

$$\begin{array}{c} \sigma^2 = \sum (n^2 - 2nMp + M^2p^2) f_{M,p}(n) \\ = \sum n^2 f_{M,p}(n) - 2Mp \sum n f_{M,p}(n) + M^2p^2 \sum f_{m,p}(n). \end{array} \quad \text{(B.11)}$$

The sums in the second and third position are already known from Eqs.(B.8) and (B.3), respectively. Using these, we find

$$\sigma^2 = \sum n^2 f_{M,p}(n) - (Mp)^2. \quad \text{(B.12)}$$

To evaluate the second term sum, we differentiate Eq.(B.8):

$$\sum n \binom{M}{n} [np^n(1-p)^{M-n} - (M-n)p^n(1-p)^{m-n-1}] = M. \quad \text{(B.13)}$$

We now multiply by $p(1-p)^{M-n}$, obtaining

$$\sum n^2 \binom{M}{n} p^n(1-p)^{M-n} = -Mp \sum \binom{M}{n} p^n(1-p)^{M-n} = Mp(1-p). \quad \text{(B.14)}$$

Finally, using Eq.(B.8) once again,

$$\sum n^2 \binom{M}{n} p^n(1-p)^{M-n} = (Mp)^2 + Mp(1-p) \quad \text{(B.15)}$$

That is $\sum n^2 f_{N,p}(n) = Mp(1-p+Mp)$. Now, inserting this result into Eq.(B.12), we obtain

$$\sigma^2 = Mp(1-p+Mp) - (Mp)^2 = Mp(1-p) = Mpq, \quad \text{(B.16)}$$

Therefore $\sigma = \sqrt{Mpq}$.

Appendix C

Dijkstra's Algorithm

The first step to understand how to find the shortest path connecting two different nodes in a graph is to study Dijkstra's algorithm and its implementations.
"Diijstra Shortest Path" algorithm computes the shortest path between nodes and it is feasible on weighted (or unweighted: all edges would have the same weight) graphs. For our interests, we will consider only undirected graphs, which have direction-less edges connecting the nodes [**60**].

We start considering n nodes, some or all pairs of which connected by an edge. We know the length (weight) of each edge. Let us suppose that at least one path exists between each pair. The solution has two tasks.
First Task Construct the tree of minimal length between n nodes and its 'root' node. The root node is called *house*. That tree is going to be formed by all the nodes connected by *branches*. The algorithm will choose which edges are going to be used as *branches*.
Initialization:
Let us start putting all the nodes in the U set and considering the *distance* array reporting nodes distance from the root node. It is clear that $distance(house)$ is initialized as zero. Let's be agnostic about other nodes distances, supposing them infinite - just initially.

```
U=[graph nodes];
distance(U)=inf;
distance(house)=0;
```

Those distances will be updated and defined in algorithm running: any time it processes a node, it gives it its distance and removes that node from U. Hence, U represents the unprocessed nodes. The algorithm stops as U is empty. Let's introduce $previous(u)$, that represents the previous node of u node in the tree *branches*.
Processing:
At each iteration, the v node in U that has the minimum distance is chosen and processed. The *house* node is obviously the first to be processed.

```
while Q is not empty
v: distance(v)<distance(U-v);
U=U-v;
for n:Neighbour(v)
alt=distance(v)+weight(edge(v,n))
if alt<distance(n):
```

```
  distance(n)=alt;
  previous(n) = v;
  end (if)
  end (for)
  end (while)
```

The algorithm will consider all v neighbours nodes, one a time, and will check their distance from v, with this operation: let's call $alt = distance(v)+weight(edge(v,n))$, where n is the neighbour node considered, and ask '$alt < distance(n)$?' If it is *true* - as it is any time an unvisited node is been checked - $distance(n) = alt$ and $previous(n) = v$ are updated. Those values are going to be confirmed and defined as that n node is chosen to be the new v node for new iteration. At that point it is possible to make the tree grow connecting nodes as pointed out by *previous* array.
Second Task Find the path of minimum total length between two given nodes: *house* and *destination*. It would be enough to take a look on the branches connecting *house* to *destination* to find the shortest path.
Its distance is obviously $distance(destination)$.

Appendix D

MatLab Codes

D.1 Constants

```
%% Constants%%%%%%%%%%%%%%%%%%%%%%%%%%%%%%%%%%%%%%%%%%%%

pi=3.1415;
ep0=8.85e-12;%C^2/Nm^2
hbar=1.054e-34;%Js
c=3e8;%m/s
e=1.58e-19;%Coulomb
kB=1.380e-23; %J/K

MASS=87.9*1.6e-27;

workLength=14;%mm
Magni=8;
NA=0.5;
CA=1/2*(1-sqrt(1-NA^2));
CA1=(4+(NA^2-4)*sqrt(1-NA^2))/8;

phi=0; %phase
omega1=2*pi*c/461e-9; %Hz% atomic transition frequency
omega2=2*pi*c/689e-9;

MASS=87.9*1.6e-27;

%%Linewidths
gamma1=2*pi*30e+6;
gamma2=2*pi*7e+3;

omegap=6.62606957e-34;
%%%%%%%%%%%%%%%%%%%%%%%%%%%%%%%%%%%%%%%%%%%%%%%%%%%%%%%%%%
save('constants')
```

D.2 QMC Thermal Fluorescence

```
%% Fluorescence and Cooling Trajectories Simulation
%by Andrea Fantini
%28/01/2022

clf
clear all
close all

%%
load('constants')

exT=10e-3;%s expositionTime
omegaT=6.7410e+5;  %for a 2000 muK depth (20 mW) SLM tweezer

%% Dynamics parameters
dt=1e-8;      %not less than 8
Tmax=1*dt*1e+6;
%           Tmax=exT;
imax1=round(Tmax/dt);

det1=1*omega1*1e-8;   % imaging detuning  (fixed or 8 or 9)
det2=1*omegaT;        % Sideband cooling

omegai=omega1+det1; %imaging beam blue
omegac=omega2-det2; %cooling beam red

Is1=2/3*pi^2*hbar*gamma1*omegai^3/c^2; %Saturation Intensity
Is2=2/3*pi^2*hbar*gamma2*omegac^3/c^2;

b1=1e-2; %Intensity module x mW  Gammas1>3*10^4 Hz
b2=0.8e-3; %it is important that omegaT>2*sqrt(2*Rabi2^2+gamma2^2)

OH=377;
W0=0.001;  % imaging and cooling beams waist

EW1=b1*1e-3;                  % Watt(J/s) Electric Field Intensity
                    in Power
EV1=sqrt(4*OH/pi/W0^2*EW1);  % Electric Field Intensity in Volts/
                    meters
EW2=b2*1e-3;                  % [J/s]
EV2=sqrt(4*OH/pi/W0^2*EW2);  % [V/m]

r1=2*EW1/pi/W0^2/Is1;
r2=2*EW2/pi/W0^2/Is2;

RDME1=3*pi*ep0*hbar*c^3/omega1^3*3*gamma1;
RDME2=3*pi*ep0*hbar*c^3/omega2^3*3*gamma2;

% Rabi oscillations%%%%%%%%%%%
Rabi1=e*sqrt(RDME1/e^2)*EV1/hbar;
Rabi1_g=sqrt((det1)^2+Rabi1^2);

Rabi2=e*sqrt(RDME2/e^2)*EV2/hbar;
Rabi2_g=sqrt((det2)^2+Rabi2^2);

T=2*pi/Rabi1;
```

```
T_g=2*pi/Rabi1_g;
%%%%%%%%%%%%%%%%%%%%%%%%%%%%%%%

s1=2*Rabi1^2/gamma1^2;
s2=2*Rabi2^2/gamma2^2;

gammas1=gamma1*sqrt(1+s1);
gammas2=gamma2*sqrt(1+s2);

Gammas1=gammas1/2/pi/2*s1/(1+s1+(4*det1^2/gammas1^2)) %scattering
                    rate

Gammas2=gammas2/2/pi/2*s2/(1+s2+(4*det2^2/gammas2^2));

%% Thermal Parameters
AT=sqrt(hbar/MASS/omegaT);
eta=2*pi/461e-9*AT;

k1=1/c*omegai;
k2=1/c*omegac;

ER=hbar*k1^2/2/MASS; %Recoil Energy for Imaging
Ej=0.002*kB/hbar; %Jump Energy
E0=hbar*k2^2/2/MASS; %cooling recoil

CG=1; %Clebsch Gordan Coefficient
Ud=2/3*CG*Rabi2^2/4/det2; %Sisyphus Cooling

%Repumps beam and Heating rate
gam1=13e+6;
gam2=39e+6;
gam3=67e+6;
lam1=679.3e-9;
lam2=688.0e-9;
lam3=707.2e-9;
ER1=(2*pi/lam1)^2*hbar/2/MASS;
ER2=(2*pi/lam2)^2*hbar/2/MASS;
ER3=(2*pi/lam3)^2*hbar/2/MASS;
%heating rate
HR=ER1*gam1+ER2*gam2+ER3*gam3;
HR=(HR/3)*dt;
%% 3 levels Atom

% 3Level matrices %%%%%%%%%%%
sx1=[0 1 0;1 0 0; 0 0 0];
sx2=[0 0 0;0 0 1;0 1 0];
sy1=[0 -1i 0; 1i 0 0; 0 0 0];
sy2=[0 0 0; 0 0 +1i ;0 -1i 0];
sz1=[1 0 0; 0 -1 0;0 0 0];
sz2=[0 0 0;0 -1 0; 0 0 1];

sp1=1/2*(sx1+1i*sy1);
sm1=sp1';

sp2=1/2*(sx2+1i*sy2);
sm2=sp2';
%%%%%%%%%%%%%%%%%%%%%%%%%%%%%%%

```

```
%% Hamiltonians

% Atomic Hamiltonian
Ha=omega1*sp1*sm1+omega2*sp2*sm2;

%Interaction H
Hi=Rabi1/2*sx1+Rabi2/2*sx2;

% Total H
H=0*Ha+Hi;

Delta1=omegai-omega1;
Delta2=omegac-omega2;

% Effective H
Heff=(Delta1-1i*gamma1)*sp1*sm1+(Delta2-1i*gamma2)*sp2*sm2+Hi;

% Lindblad Operators
C=zeros(3,3,2);
C(:,:,1)=sqrt(gamma1)*sm1;
C(:,:,2)=sqrt(gamma2)*sm2;

% Number operator for the Atomic Photonic system
NopA=sp1*sm1+sp2*sm2;

%% Trajectories
qt=1; %number of quantum trajectories

Y=zeros(qt,1,3); % reduced traces
EN=zeros(1);

for ii=1:qt  %Quantum Trajectories Loop
kk=1;
% Density matrix for initial state
psi=zeros(3,1);
psi(2)=1; %|0>
cool=0;
sycool=0;
photon=0;
loss=0;

x=zeros(1);      % time
y=zeros(1,3);    % populations

En=30e-6*kB/hbar; %initial Energy: MOT temperature

for jj=1:imax1

if En>Ej
rho=zeros(3); %atom lost
loss=1;
break
end

psi=psi-1i*dt*Heff*psi;
psi=psi/norm(psi);
En=En+HR/1000;

```

```
if mod(jj,10)
if rand<(norm(C(:,:,2)*psi)^2*10*dt)/2/pi % Cooling
nv=En/omegaT;
if  rand<(norm(C(:,:,2)*psi)^2*10*dt)/2/pi*eta^2*nv
En=En-omegaT; %Sideband Cooling
cool=cool+1;
else

if rand<2/3 %assuming it is always sisyphus position
En=En-Ud;     %Sisyphus Cooling
sycool=sycool+1;
sisyphustime=0;
end
end

psi=C(:,:,2)*psi;
psi=psi/sqrt(psi'*psi);

if En<2*E0
En=2*E0;
end
else
end
end

if mod(jj,3)==0
if rand<(norm(C(:,:,1)*psi)^2*3*dt)/2/pi     % Fluorescence
psi=C(:,:,1)*psi;
psi=psi/sqrt(psi'*psi);
photon=photon+1;
En=En+2*ER;
end
end

if mod(jj,10)==0   %saving section
x(kk)=jj*dt;
y(kk,:)=diag(psi'.*psi);
EN(kk,ii)=En;


kk=kk+1;
end

ProcessedPercentage(ii)=jj/imax1*100

end
Photo(ii)=photon;
Loss(ii)=loss;
end
%% Plotting
% hold on
% plot(x,y)
%  legend('1','0','2')
% hold off

photon
cool
sycool
```

```
228
229 jumpenergy=Ej*ones(kk-1,1);
230 %%
231 figure ()
232 L=length(EN);
233
234 for kk=1:L/100
235 %   plot(x,EN);
236 plot(x(1:kk*100),EN(1:kk*100));
237 %      plot(x,jumpenergy);
238 xlabel('time (s)')
239 ylabel('Energy (Hz)')
240 axis([0 1e-2 0 Ej])
241 pause(0.0001)
242 end
243 save('FCparameters')
244 %%
245 % figure()
246 % data=Photo'*0.8*CA1*10
247 % histogram(data)
248 % h=histfit(data,20,'normal')
249 % pd = fitdist(data,'Normal')
250 %   mean(Loss)
251 % save('fluorescence')
```

D.3 Noise Simulation

```
%% Camera Simulation
%by Andrea Fantini
%28/01/2022

clf
clear all
close all

load('fluorescencefinal')

Magni=8;

dpx=1.5e-6;      %pixel real dimension
lambda=461e-9;



tot=1e+4;
dt=0.00001;

I=3; %alalysis pixels

%% Noise
xx = 0:25;
noise=0.7;
yy = pdf('Normal',xx,0,noise); %Background
zz=poisspdf(xx,1.5);
ww = pdf('Normal',xx,0,sqrt(12));

back=zeros(1);
shot=zeros(1);
read=zeros(1);

kk=1;
hh=1;
gg=1;
for pp=0:24
for ll=1:round(1000*yy(pp+1))
back(kk)=pp;
kk=kk+1;
end
for ll=1:round(1000*zz(pp+1))
shot(hh)=pp;
hh=hh+1;
end
for ll=1:round(1000*ww(pp+1))
read(gg)=pp;
gg=gg+1;
end
end


%%
p=0;
bk=ones(1);
L=length(back)-1;
```

```
for kk=1:1000
camera=zeros(I);
t=0;
if t<tot
for ii=1:I
for jj=1:I
p=back(round(rand*L+1));
a=camera(ii,jj);
camera(ii,jj)=a+p;
end
end
t=t+dt;
end
bk(kk)=sum(sum(camera));
end
histogram(bk)
title('Background Noise')
%%
p=0;
L=length(shot)-1;
for kk=1:1000
camera=zeros(I);
for ii=1:I
for jj=1:I
p=shot(round(rand*L+1));
a=camera(ii,jj);
camera(ii,jj)=a+p;
end
end
sh(kk)=sum(sum(camera));
end
figure()
histogram(sh)
title('ShotNoise')
%%
p=0;
L=length(read)-1;
for kk=1:1000
camera=zeros(I);
for ii=1:I
for jj=1:I
p=read(round(rand*L+1));
a=camera(ii,jj);
camera(ii,jj)=a+p;
end
end
re(kk)=sum(sum(camera));
end
figure()
histogram(re)
title('Readout Noise')
%%
ph=Photo'*0.8*CA1*10*0.84; % 84% is Airy portion
d=[ph;ph;ph;ph];
%   data=[d;d;d;d;d;d;d;d;d;d]; %10^4 events

figure()
hold on
```

```
da=d+1*(I^2-9)*((mean(back)))
histogram(da,round(max(da)-min(da)) )
histogram(re, round(max(re)-min(re)))
histogram(bk,round(max(bk)-min(bk)))
histogram(sh,round(max(sh)-min(sh)))
legend('Signal', 'Readout', 'Background', 'Shot')

ylabel('events')
xlabel('photo-count')

title('Camera Noise and Cut Signal on a single pixel')

hold off

save('signal')
```

D.4 Camera Gain Simulation

```
%% Camera Gain
%by Andrea Fantini
%20/05/2022

clf
clear all
close all

load('signal1')

d=round(d/9);
sort(d);
r=[bk,sh,re];
signal=[r';d];

figure()
hold on
histogram(d)
histogram(r,10)
legend('Signal', 'Noise')

mean(10*d/9)/mean(r)

ylabel('events')
xlabel('electro-count')

title('Gain-Signal Amplification')

hold off
%%
pd = fitdist(d,'Normal')
sigma=pd.sigma;

rms=sqrt(12);          %readout noise

g=5*rms;         %gain

Magni=8;
```

```
39
40 dpx=1.5e-6;      %pixel real dimension
41 lambda=461e-9;
42
43 %%
44
45 for ll=1:10
46 g=round(sigma*ll*5);
47
48 %  d=[0,1,2,3,4,5,6,7,8,9,10,50,55,60,65];
49 d=signal;
50
51
52 m=round(max(r));
53 b=round(max(d));
54
55 %  d=[0,m-1,m,m+1,b-2,b-1,b]
56
57 c=3*g*m+1;
58 k=3*g*b+1;
59 C=1:c;
60 K=1:k;
61
62 P=0*ones(c,1);
63 P=sparse(P);
64 S=0*ones(k,1);
65 S=sparse(S);
66
67 for ii=1:length(d)
68 n=d(ii);
69 for jj=1:3*g*n-1
70 s=jj;
71 A=S(s,1);
72 S(s,1)=A+s^(n-1)*exp(-s/g)/g^n/factorial(n-1);
73 end
74 percentuale = ii*100/length(d)
75 end
76
77 C=C';
78 figure()
79 hold on
80 plot(K,S,'-o');
81 %  plot(C,P,'-o');
82
83
84 ylabel('events')
85 xlabel('electro-count')
86
87 str = sprintf('Gain=%d Signal Amplification', g);
88 title(str)
89
90 hold off
91 pause(0.2)
92 end
```

D.5 Function Simulating Tweezer

```
%Andrea Fantini 18/11/2021
function At=move(Path, At,G,x,y)
L=length(Path);
for ss=2:L %steps
plotting(G,At,Path,x,y)
At(Path(ss-1))=0; %updating
At(Path(ss))=1;
plotting(G,At,Path,x,y)
if ss>=L
break;
end
end
end
```

D.6 Edges Cleaning Function

```
%Andrea Fantini 18/11/2021
function G=edgesremoving(G,n,xy)

T=ones(1,height(G.Edges));
S=T;
for ee=1:height(G.Edges)
if ee>height(G.Edges)
break
end
for nn=1:n

K1=G.Edges.EndNodes(ee,1);
K2=G.Edges.EndNodes(ee,2);
nn ;

if nn~=K1 && nn~=K2
X1Y1=xy(K1, :);
X2Y2=xy(K2, :);

b= hypot(X1Y1(1)-X2Y2(1),X1Y1(2)-X2Y2(2));
a=b/2;%edgelength divided by 2 micron

for ii=1:round(a)
xx=X1Y1(1)+(X2Y2(1)-X1Y1(1))*ii/a;
yy=X1Y1(2)+(X2Y2(2)-X1Y1(2))*ii/a;
h=hypot(xy(nn,1)-xx,xy(nn,2)-yy);
if h<5 %micron
S(ee)=K1;
T(ee)=K2;
break;
end
end
end
end
PercentualeProcessata=ee*100/height(G.Edges)
end
G=rmedge(G,S,T)
end
```

D.7 Graph Creation Page

```
%Andrea Fantini 18/11/2021

clf
clear all
close all
%% Crown Spiral Geometry with N nodes (C)
N=80; %max 80
R=150; %Extrnal Ray
r=100; %Internal Ray
for ii=1:N
ray=(r+(R-r)/N*ii);
xyf(ii,:)=[150+ray*cos(ii*pi/8),150+ray*sin(ii*pi/8)];
end
plot(xyf(:,1),xyf(:,2), 'o');
%% Arbitrary Array with N nodes (A)
% xyf= randi(300,50,2); %random free %300 micron


% xyf=[150,100;150,110;140,110;160,110;
%       145,120;155,120;140,130;160,130;
%       130,130;170,130;125,125;175,125;
%     120,110;180,110;115,120;185,120;
%       115,130;185,130;120,140;180,140;
%     130,140;170,140;145,137;155,137;
%       140,150;160,150;130,160;170,160;
%     135,170;165,170;140,180;160,180;
%       150,190];% a Giglio
% save('xy')
%% Rectangular Compact Array with N nodes (R)
% N=39; %max 100
% for ii=0:N-1
%         xyf(ii+1,:)=[100+10*mod(ii,10),100+10*round(mod(abs(ii-5)
                    /10,10))];
% end
% xyf(1,2)=100;
%
% xyf=[100,100;110,100;120,100;
%       100,110;110,110;120,110;
%       100,120;110,120;120,120]; % N=9

% xyf=[100,100;110,100;120,100;
%      100,110;110,110;120,110;
%      100,120;110,120;120,120;
%      100,130;110,130;120,130]; % N=12

% xyf=[100,100;110,100;120,100;130,100;140,100;
%      100,110;110,110;120,110;130,110;140,110;
%      100,120;110,120;120,120;130,120;140,120;
%      100,130;110,130;120,130;130,130;140,130]; % N=20
%% Triangular Compact Array with N nodes (T)
% N=39; %max 100
% for ii=0:N-1
%         xyf(ii+1,:)=[100+10*mod(ii,10)+5*mod(round(abs(ii-5)/10)
                    ,2),100+10*round(mod(abs(ii-5)/10,10))];
% end
% xyf(1,:)=[100,100];
```

```
55
56 %xyf=[100,100;110,100;120,100;105,110;
57 %    115,110;125,110;100,120;110,120;120,120]; % N=9
58
59 % xyf=[100,100;110,100;120,100;
60 %     105,110;115,110;125,110;
61 %     100,120;110,120;120,120;
62 %     105,130;115,130;125,130]; % N=12
63
64 % xyf=[100,100;110,100;120,100;130,100;140,100;
65 %     105,110;115,110;125,110;135,110;145,110;
66 %     100,120;110,120;120,120;130,120;140,120;
67 %     105,130;115,130;125,130;135,130;145,130]; % N=20
68
69
70 %% Traps shaping
71 x=[xyf(:,1)];
72 y=[xyf(:,2)];
73 N=length(x);
74
75 pi=3.1415;
76 xyres=ones(N,2); %reserve trap
77
78 for ii=1:N
79 nn=0;
80 nc=1;
81 while nc==1
82 nc=0;
83 res=[xyf(ii,1)+(5+0.05*nn)*cos(nn*pi/8),xyf(ii,2)+(5+0.05*nn)*sin(
                    nn*pi/8)];
84 for jj=1:N %check on final nodes
85 if  sqrt(sum((res - xyf(jj,:)) .^ 2))<10
86 nc=1;
87 end
88 end %check on reserve nodes
89 for jj=1:length(xyres(:,1))
90 if  sqrt(sum((res - xyres(jj,:) ).^ 2))<10
91 nc=1;
92 end
93 end
94 nn=nn+1;
95 end
96 if 0>res(1)||res(1)>350 || 0>res(2)||res(2)>350
97 nc=1;
98 end
99 if nc==1
100 break;
101 end
102 xyres(ii,:)=res;
103 end
104 if nc==1
105 error(message('ERROR:Graph unuseful'))
106 end
107
108 % SurplusTraps
109 for ii=1:round(2*sqrt(3*N))
110 nn=0;
111 nc=1;
```

```
while nc==1
nc=0;
res=[mean(xyf(:,1))+(5+0.05*nn)*cos(nn*pi/8),mean(xyf(:,2))
                    +(5+0.05*nn)*sin(nn*pi/8)];
for jj=1:N %check on final nodes
if  sqrt(sum((res - xyf(jj,:)) .^ 2))<10
nc=1;
end
end %check on reserve nodes
for jj=1:length(xyres(:,1))
if  sqrt(sum((res - xyres(jj,:) ).^ 2))<10
nc=1;
end
end
nn=nn+1;
end
if 0>res(1)||res(1)>350 || 0>res(2)||res(2)>350
nc=1;
end
if nc==1
break;
end
xyres(N+ii,:)=res;
end


x=[xyf(:,1);xyres(:,1)];
y=[xyf(:,2);xyres(:,2)];
xy=[x,y];

%% Triangulation
DT = delaunay(x,y);% triplot(DT,x,y);
TR = triangulation(DT,x,y);
E=edges(TR);
s=E(:,1);
t=E(:,2);
G = graph(s,t);
n = numnodes(G);
%% FullConnected
A=ones(n,n);
G=graph(A,'omitselfloop');
%% Too Close Egdes Removing
G=edgesremoving(G,n,xy);

%%
save('xy', 'G','xy','n','N');
```

D.8 Atomic Graph Analysis

```
%Andrea Fantini 18/11/2021

clf
clear all
close all

load('xy') %traps array loading

%% Closeness and Betweeness
s=G.Edges.EndNodes(:,1);
t=G.Edges.EndNodes(:,2);
G.Edges.Weight = hypot(xy(s,1)-xy(t,1), xy(s,2)-xy(t,2));

figure(1)
p = plot(G,'XData',xy(:,1),'YData',xy(:,2),'MarkerSize',5);
ucc = centrality(G,'closeness');
p.NodeCData = ucc;
colormap jet
colorbar
title('Closeness Centrality Scores - Unweighted')

wcc = centrality(G,'closeness','Cost',G.Edges.Weight);
wcc = normalize(wcc, 'range',[0,1]);

p.NodeCData = wcc;
title('Closeness Centrality Scores - Weighted')

figure(2)
p = plot(G,'XData',xy(:,1),'YData',xy(:,2),'MarkerSize',5);
wbc = centrality(G,'betweenness','Cost',G.Edges.Weight);

wbc=2*wbc./((n-2)*(n-1));
wBc=normalize(wbc, 'range',[0,1]);


p.NodeCData = wBc;
colormap jet%(flip(autumn,1));
colorbar
title('Betweenness Centrality Scores - Weighted')

%% Priority Selection
wgc=wcc;
[~,b]=sort(wcc);
wgc(b(n))=wgc(b(n))/2; %experimental evidence

figure(3)
p = plot(G,'XData',xy(:,1),'YData',xy(:,2),'MarkerSize',5);
p.NodeCData = wgc;
colormap jet
colorbar
title('Piority Weight')

%% Path Searching
dista=ones(n,n/2)*Inf;
spath=zeros(n,n/2,n); %shortestpath
Lenght=ones(n,n/2)*Inf;
```

```
magazine=zeros(n/2,n);
for ii=1:n/2
for jj=1:n
[P, d]=shortestpath(G,jj,ii);
L=length(P);
spath(jj,ii,1:L)=P;
dista(jj,ii)=d;
Length(jj,ii)=L;
end
[~,magazine(ii,:)]=sort(dista(:,ii));
end
%% Atom Loading
At=zeros(n,1); %Enough Atoms
while sum(At)<N
At=round(rand(n,1))';
end
numberofatom=sum(At)

figure(4)
p = plot(G,'XData',xy(:,1),'YData',xy(:,2),'MarkerSize',5);
p.NodeCData = At;
title('Loaded Atoms Network')
%%
save('AtomLoaded','G','xy','n','N','At','spath','dista','Length'
                    ,...
'magazine','wgc')
```

D.9 Atomic Graph Reconfiguration

```
1
2  %Andrea Fantini 5/01/2022
3  clf
4  clear all
5  close all
6
7  hc=3.0; %HybridationControl
8
9  nm=0;% Number of Moved Atoms
10 sc=0; %steps count
11
12 load('AtomLoaded') %traps array loading (IMAGING)
13 x=xy(:,1);
14 y=xy(:,2);
15
16 %% Atom Loading
17
18 At=zeros(n,1); %Enough Atoms
19 while sum(At)<n/2
20 At=round(rand(n,1))';
21 end
22 numberofatom=sum(At);
23 Atiniziale=At;
24
25 %% Priority Hybrid
26
27 for ii=1:n/2
28 if At(ii)==1
29 wgc(ii)= wgc(ii)*hc ;
30 end
31 end
32 wgc(n/2+1:n)=zeros(1,n/2); %no priority for reserve traps
33 [~,priority]=sort(wgc(1:n/2));
34
35 %% Reconfiguration
36
37 DIST=ones(n/2,1)*Inf;
38
39 for kk=1:n/2 %target
40 ii=priority(n/2-kk+1);
41 if At(ii)==0
42 for hh=2:n %the first is house node
43 jj=magazine(ii,hh); %source
44
45 if At(jj)==1 %on nodes loaded with atoms
46 if wgc(ii)>=wgc(jj)%not move from more to less important traps
47 L=Length(jj,ii);
48 Path(1:L)=spath(jj,ii,1:L);
49 DIST(ii)=dista(jj,ii);
50 break
51 end
52 end
53 end
54
55 sc=sc+L-1;
56 tt=L;%target point
```

```
plotting(G,At,Path,x,y)

fw=0;
while fw==0 %freeway control
fw=1;
for oo=1:tt-1
ob=tt-oo;
if At(Path(ob))==1
fw=0;
break
end
end
if fw==0
PATH=Path(ob:tt);
plotting(G,At,PATH,x,y)
At=pmove(PATH,At,G,x,y);
tt=ob;
nm=nm+1;
end
end
end
clear Path
wgc(ii)=wgc(ii)+sum(wgc); %updating trap weight trap
%(if it's done, don't take from it!)
end

%% Atoms Dropping
sc=sc+sum(At(n/2+1:n));

for ii=1:n/2
if DIST(ii)==Inf
DIST(ii)=0;
end
end

if At(1:n/2)==1
'SUCCESS'
L1=sum(DIST);
TotSteps=sc;
At(n/2+1:n)=zeros(1,n/2);
else
'MISSION ABORTED'
end

%% Results
% mean(L1)
TotalSteps=mean(TotSteps)
TotalMoves=mean(nm)

%% Plotting
p = plot(G,'XData',x,'YData',y);
title('After Dropping')
p.NodeCData = At;
highlight(p,linspace(1,n/2,n/2), 'MarkerSize', 15);
```